Technische Universität München
Fakultät für Mathematik

Reconstructions in limited angle x-ray tomography: Characterization of classical reconstructions and adapted curvelet sparse regularization

Jürgen Frikel

Vollständiger Abdruck der von der Fakultät für Mathematik der Technischen Universität München zur Erlangung des akademischen Grades eines

Doktors der Naturwissenschaften (Dr. rer. nat.)

genehmigten Dissertation.

Vorsitzender:		Univ.-Prof. Dr. Peter Gritzmann
Prüfer der Dissertation:	1.	Univ.-Prof. Dr. Brigitte Forster-Heinlein, Universität Passau
	2.	Univ.-Prof. Dr. Rupert Lasser
	3.	Prof. Samuli Siltanen, Ph.D. University of Helsinki / Finland

Die Dissertation wurde am 01.10.2012 bei der Technischen Universität München eingereicht und durch die Fakultät für Mathematik am 12.03.2013 angenommen.

Abstract

In this thesis we investigate the reconstruction problem of limited angle tomography. Such problems arise naturally in practical applications like digital breast tomosynthesis, dental tomography or electron microscopy. Many of these modalities still employ the filtered backprojection (FBP) algorithm for practical reconstructions. However, as the FBP algorithm implements an inversion formula for the Radon transform, an essential requirement for its application is the completeness of tomographic data. Consequently, the use of the FBP algorithm is theoretically not justified in limited angle tomography. Another issue that arises in limited angle tomography is that only specific features of the original object can be reconstructed reliably and additional artifacts might be created in the reconstruction.

The first part of this work is devoted to a detailed analysis of classical reconstructions at a limited angular range. For this purpose, we derive an exact formula of filtered backprojection reconstructions at a limited angular range and interpret these results in the context of microlocal analysis. In particular, we show that a meaningful a-priori information can be extracted from the limited angle data. Moreover, we prove a characterization of limited angle artifacts that are generated by the filtered backprojection algorithm and develop an artifact reduction strategy. We also illustrate the performance of the proposed method in some numerical experiments. Finally, we study the ill-posedness of the limited angle reconstruction problem. We show that the existence of invisible singularities at a limited angular range entails severe ill-posedness of limited angle tomography. Owing to this observation, we derive a stabilization strategy and justify the application of the filtered backprojection algorithm to limited angle data under certain assumptions on the target functions.

In the second part of this work, we develop curvelet sparse regularization (CSR) as a novel reconstruction method for limited angle tomography and argue that this method is stable and edge-preserving. We also formulate an adapted version of curvelet sparse regularization (A-CSR) by applying the stabilization strategy of the first part, and provide a thorough mathematical analysis of this method. To this end, we prove a characterization of the kernel of the limited angle Radon transform in terms of curvelets and derive a characterization of CSR reconstructions at a limited angular range. Finally, we show in a series of numerical experiments that the theoretical results directly translate into practice and that the proposed method outperforms classical reconstructions.

Acknowledgements

At this place my gratitude goes to all who contributed to the completion of this work.

First and foremost, I wish to thank my PhD advisor Prof. Dr. Brigitte Forster-Heinlein for her help, her advice and the freedom she gave me during the time I spent on this thesis. I have also enjoyed her supported throughout the time of my student project and my diploma thesis at TUM, where I already had the opportunity to work in the field of tomographic image reconstruction. Furthermore, I also thank Prof. Dr. Rupert Lasser and Prof. Dr. Samuli Siltanen for their interest in my work and for having agreed to write a report for this thesis.

The first two and a half years of my research to the topic of this thesis were carried out at GE Healthcare, Image Diagnost International, Munich, whose financial support I gratefully acknowledge. In particular, I am much obliged to Dr. Peter Heinlein, my advisor at GE Healthcare, Image Diagnost International, for giving me the chance to do research in a practical environment. I appreciate very much his help and his patience during this time.

I sincerely thank Dr. Frank Filbir for giving me the opportunity to work on my dissertation while I was employed in his research group at the Institute of Biomathematics and Biometry, Helmholtz Zentrum München. I have profited much from his advice and his support during this time. In particular, I want to thank him for giving me the chance to travel and to get in touch with distinguished scientists. During that time I received financial support from DFG (grant no. FI 883/3/3-1) which I herewith gratefully acknowledge.

It is my pleasure to express my gratitude to Prof. Dr. Eric Todd Quinto (Tufts University, Medford, USA), for many fruitful and inspiring discussions on the topic of limited angle tomography and for his hospitality during my visits, where some ideas of Section 3.4 were developed. Furthermore, I wish to thank PD Dr. Peter Massopust, Prof. Dr. Wolodymyr R. Madych (University of Connecticut, Storrs, USA) and Prof. Dr. Hrushikesh Mhaskar (Caltech, USA) for discussing mathematics with me and for proofreading parts of my work.

Especially, I would like to thank my colleague and friend Martin Storath, with whom I have shared an office over the past years, for many inspiring and valuable discussions as well as for proofreading all versions of this work. Moreover, I am very grateful to Prof. Dr. Stefan Kunis for carefully proofreading this work and many valuable remarks. I have also benefited a lot from brainstorming ideas and mathematical discussions with Dr. Laurent Demaret and Dr. Thomas Amler.

Finally, and most importantly, I would like to express my deep gratitude to my wife Elena and to my parents for their constant support, encouragement, patience and love.

Contents

Chapter 1

Introduction

Computed tomography (CT) has revolutionized diagnostic radiology and is by now one of the standard modalities in medical imaging. Its goal consists in imaging cross sections of the human body by measuring and processing the attenuation of x-rays along a large number of lines through the section. In this process, a fundamental feature of CT is the mathematical reconstruction of an image through the application of a suitable algorithm. The corresponding mathematical problem consists in the reconstruction of a function $f : \mathbb{R}^2 \to \mathbb{R}$ from the knowledge of its line integrals

$$\mathcal{R}f(\theta, s) = \int_{L(\theta,s)} f(x)\, \mathrm{d}S(x),$$

where $L(\theta, s) = \{x \in \mathbb{R}^2 : \ x_1 \cos\theta + x_2 \sin\theta = s\}$. The purely mathematical problem of reconstructing a function from its line integrals was first studied and solved by the Austrian mathematician Johann Radon in 1917 in his pioneering paper "Über die Bestimmung von Funktionen durch ihre Integralwerte längs gewisser Mannigfaltigkeiten", cf. [Rad17]. In that work, he derived an explicit inversion formula for the integral transform $\mathcal{R} : f \mapsto \mathcal{R}f(\theta, s)$ under the assumption that the data $\mathcal{R}f(\theta, s)$ is complete, i.e., available for all possible values $(\theta, s) \in [-\pi/2, \pi/2) \times \mathbb{R}$. More than 50 years later, when Allan M. Cormack, [Cor63, Cor64], and Godfrey N. Hounsfield, [Hou73], invented computer assisted tomography[1], this mathematical problem has finally become relevant for practical applications. This breakthrough has attracted very much attention in engineering sciences as well as in the mathematical community. Especially, the tomographic reconstruction problem has been studied extensively, and many different reconstruction algorithms were developed for the case of complete tomographic data, cf. [Nat86, NW01], [KS88], [RK96], [Eps08], [Her09].

The success of computed tomography has also initiated the development of new imaging techniques. In some of these applications the tomographic data can be acquired only at a limited angular range, i.e., the integral values $\mathcal{R}f(\theta, s)$ are merely available for $(\theta, s) \in [-\Phi, \Phi] \times \mathbb{R}$, where $\Phi < \pi/2$. According to that, the reconstruction problem of limited angle tomography is equivalent to the inversion of the limited angle Radon transform $\mathcal{R}_\Phi : f \mapsto \mathcal{R}f|_{[-\Phi,\Phi]\times\mathbb{R}}$, rather than the full Radon transform $\mathcal{R}$. Typical examples of modalities where such problems arise are digital breast tomosynthesis (DBT) [N$^+$97], [III09], dental tomography [HKL$^+$10], [MS12], or

[1] Allan M. Cormack and Godfrey N. Hounsfield were jointly awarded with the Nobel prize in Physiology and Medicine in 1979 for the development of computer assisted tomography.

electron microscopy [DRK68]. In these cases, the available angular range $[-\Phi, \Phi]$ might be very small. In DBT, for example, the angular range parameter usually varies between $\Phi = 10^\circ$ and $\Phi = 25^\circ$, [ZCS+06], [III09]. In such situations, the reconstruction methods for the full angular problem are no longer applicable. In [Lou79], [Per79], [Grü80], [Ino79], [Ram91, Ram92], dedicated inversion methods for the limited angle tomography problem were developed under the assumption that the target functions have compact support. Essentially, all of these methods utilize analytic continuation in the Fourier domain or employ the completion of the limited angle data. In particular, these methods show that a perfect reconstruction is theoretically possible even from a very small angular range. Nevertheless, there are still substantial problems that arise in practice:

Severe ill-posedness. Since the limited angle reconstruction problem is severely ill-posed [Nat86], [Dav83], all reconstruction procedures are extremely unstable, i.e., small measurement errors can cause huge reconstruction errors. This is a serious drawback since, in practice, the acquired data is (to some extent) always corrupted by noise. As a consequence, only specific features of the original object can be reconstructed stably, [Qui93].

Filtered backprojection in limited angle tomography. In practice, the filtered backprojection (FBP) algorithm is usually preferred over those inversion techniques mentioned above, cf. [PSV09], [LMKH08], [SMB03], [IG03], [SFS06], [III09]. However, as the FBP algorithm implements an inversion formula for the Radon transform, cf. Section 2.4, an essential requirement for its application is the completeness of tomographic data. Consequently, there is no theoretical justification for the application of the FBP algorithm in limited angle tomography.

Limited angle artifacts. Besides the fact that only specific features of the original object can be reconstructed reliably, the application of the FBP algorithm to limited angle data can also create additional artifacts in reconstructions, cf. Figure 3.1. Thus, even the reliable information can be distorted by these artifacts.

Edge-preserving reconstruction. The filtered backprojection algorithm does not perform well in the presence of noise, [NW01], [Her09], [MS12]. Depending on the choice of the regularization parameter, the reconstructions may appear either noisy or tend to oversmooth the edges, cf. Figure 4.1. However, edge-preserving reconstructions are of particular importance for medical imaging purposes.

In this thesis, we solve the problems listed above. To this end, we prove different characterizations of classical reconstructions at a limited angular range, justify the application of filtered backprojection to the limited angle data, and provide an artifact reduction strategy for the FBP algorithm. Furthermore, we address the severe ill-posedness by developing a novel edge-preserving reconstruction method that is adapted to the limited angle geometry, and show its practical relevance.

The thesis is organized as follows. Chapter 2 has an introductory character. It is devoted to the presentation of basic concepts of computed tomography at a full angular range. We begin with a brief overview of the imaging principle in x-ray tomography and introduce the Radon transform as a mathematical model of the measurement process in x-ray CT. Moreover, we note some fundamental properties of the Radon transform. The main part of this chapter is devoted

to the presentation of inversion formulas for the Radon transform and the study of ill-posedness of the tomographic reconstruction problem. The last section of this chapter reviews classical reconstruction methods. In particular, we present the classical filtered backprojection algorithm (FBP). Most of the material presented in this chapter is well known and can be found in the textbooks [Nat86, NW01], [KS88], [RK96], [Eps08], [Her09].

Chapter 3 contains the first part of our main results. Its main objective is the characterization of reconstructions at a limited angular range. In Section 3.2, we begin our investigations by studying the backprojection of limited angle data. To that end, we characterize the action of the Gram operator $\mathcal{R}_\Phi^* \mathcal{R}_\Phi$ in the Fourier domain, cf. Theorem 3.6, and prove a characterization of the kernel of the limited angle Radon transform in the Schwartz space $\mathcal{S}(\mathbb{R}^2)$, cf. Corollary 3.7. We also observe that the kernel functions of $\mathcal{R}_\Phi$ are directional and illustrate this fact in a numerical example. Subsequently, we derive an exact formula for filtered backprojection reconstructions at a limited angular range in Theorem 3.9, and justify the application of the FBP algorithm to limited angle data under suitable assumptions on the sought functions. An interpretation of these results in terms of visible and invisible singularities is given in Section 3.3. In particular, we show that a meaningful a-priori information can be extracted from the limited angle data. In Section 3.4, we turn our attention to the characterization of limited angle artifacts that are generated by the filtered backprojection algorithm. Using techniques of microlocal analysis we state a characterization of these artifacts in Theorem 3.24. Based on this result, we derive an artifact reduction strategy for the FBP algorithm in Theorem 3.26, and conclude the section with numerical experiments. In Section 3.5, we discuss three aspects of the severe ill-posedness of limited angle tomography in the context of microlocal analysis. In particular, we show that the main reason for the severe ill-posedness is the existence of invisible singularities at limited angular range. Based on this observation, we finally derive a stabilization strategy for limited angle tomography.

The second part of our results is presented in Chapters 4 and 5. In Chapter 4, we develop a novel reconstruction technique that is stable, edge-preserving and adapted to the limited angle geometry. To achieve that, we combine the technique of sparse regularization, [DDDM04], with the curvelet dictionary, [CD05b], [MP10]. We show that this gives a stable and edge-preserving reconstruction method which we call *curvelet sparse regularization* (CSR). In Section 4.2, we formulate an adapted version of curvelet sparse regularization (A-CSR) by integrating the inherent a-priori information of limited angle tomography (which we derived in Chapter 3) into the CSR method. In contrast to the non-adapted CSR, the problem dimension of A-CSR is directly linked to the available angular range. In particular, a significant dimensionality reduction can be achieved for small angular ranges. The relation between the adapted and the non-adapted approach is investigated in Section 4.3. To this end, we first derive an explicit formula for the Radon transform of curvelets, cf. Theorem 4.7, and prove a characterization of the kernel of the limited angle Radon transform in terms of curvelets, cf. Theorem 4.8. Finally, we characterize the CSR reconstructions at a limited angular range in Theorem 4.10. These results show that the reconstructions obtained by the adapted curvelet sparse regularization (A-CSR) coincide with those obtained via CSR. In Section 4.4, we discuss the relation between the CSR method and the "curvelet thresholding" approach of [CD02]. In particular, we derive an explicit formula for CSR reconstructions at a full angular range and interpret the CSR method as a natural generalization of the "curvelet thresholding" approach to a limited angular range. We conclude with some further remarks on the CSR approach and discuss the related literature.

Chapter 5 is concerned with the numerical implementation and with the performance analysis of CSR and A-CSR in a practical setting. We begin by giving the details of our implementation in Section 5.1 and proceed with the presentation of numerical experiments in Sections 5.2 and 5.3. These experiments are basically divided into two parts. The first part, presented in Section 5.2, is devoted to the illustration of the visibility of curvelets under the limited angle Radon transform. In the second part of our experiments, we analyze the execution times and the reconstruction quality of CSR and A-CSR reconstructions, cf. Section 5.3. We show that a significant speedup can be achieved by using the adapted approach (A-CSR), while preserving the reconstruction quality of the CSR method. In both cases, the reconstructions are found to be superior to those obtained via filtered backprojection (FBP). In Section 5.4, we adopt the artifact reduction strategy of Section 3.4 to the adapted curvelet sparse regularization and illustrate its performance in numerical experiments.

The appendix contains supplementary material. In Appendix A, we review the basic concepts of the Fourier transform on various spaces of functions and distributions, and present the definition of Sobolev spaces H^s. The singular value decomposition of compact operators is presented in Appendix B, whereas Appendix C summarizes the fundamentals of the theory of inverse problems and regularization.

Remarks. The contents of Chapter 4 and Chapter 5 were partly published in the Journal of Applied and Computational Harmonic Analysis, [Fri12]. Moreover, the results of Section 4.3 have been announced in the Proceedings in Applied Mathematics and Mechanics, [Fri11]. We also note that an alternative approach to adapted curvelet sparse regularization was published in the Proceedings of IEEE International Symposium on Biomedical Imaging, [Fri10].

CHAPTER 2

An overview of computed tomography

In this chapter, we present the basic concepts of computed tomography (CT). We begin with an overview of the imaging principle in x-ray tomography. Subsequently, the Radon transform is introduced as a mathematical model for the measurement process in CT and some fundamental properties are noted. The main part is devoted to the presentation of inversion formulas for the Radon transform and the study of ill-posedness of the tomographic reconstruction problem. In the last section of this chapter we give a brief overview of some classical reconstruction methods. Most of the material presented in this chapter is well known and can be found in the following textbooks [Nat86, NW01], [KS88], [RK96], [Eps08], [Her09].

2.1 The principle of x-ray tomography

The aim of *x-ray tomography* (greek $\tau o \mu o \varsigma$ = slice) consists in reconstructing the interior of an unknown two dimensional object from a number of one dimensional x-ray projections. In order to explore the two-dimensional structure of the object, the x-ray projections are taken at different views. To this end, a source-detector pair is rotated around the object, cf. Figure 2.1.

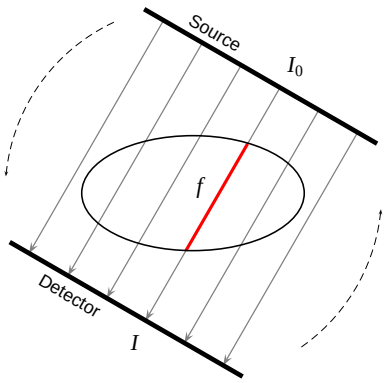

Figure 2.1: Imaging principle of x-ray tomography. In order to explore the inner structure of an object f, the x-ray projections are taken at different views. To this end, a source-detector pair is rotated around the object.

The underlying imaging principle is based on the fact that the x-rays are attenuated when passing the object. The attenuation of the x-ray depends on the interior structure and, hence, carries information about the interior of the unknown object. Assuming that the x-rays are monochromatic and that they travel along straight lines, the intensity I of an x-ray beam is given according to Beer's law by, [KS88, Sec. 4.1], [Nat86, Sec. I.1], [Eps08, Sec. 3.1.1],

$$I = I_0 \cdot \exp\left\{-\int_L f(x)\,\mathrm{d}x\right\},$$

where I_0 denotes the initial intensity of the x-ray, f is the absorption coefficient and $\mathrm{d}x$ is the arc length along the straight line path L. Assuming the initial intensity I_0 to be known, we can restate the Beer's law as

$$y_L := \ln\left(\frac{I_0}{I}\right) = \int_L f(x)\,\mathrm{d}x. \tag{2.1}$$

Recovering the absorption coefficient f or, equivalently, reconstructing an object from x-ray projections, therefore reduces to solving the mathematical equation (2.1). The theory for solving this integral equation (in the case that the data y_L is available for all possible lines L) is well developed and will be presented in the course of this chapter.

2.2 Notations

We begin by introducing some standard notation. The inner product of $x, y \in \mathbb{R}^n$, $n \in \mathbb{N}$, will be denoted as $x \cdot y$ or simply xy. When not otherwise stated, the inner product in a function space X will be denoted by $\langle f, g\rangle_X$. The Euclidean norm of a vector $x \in \mathbb{R}^n$ will be denoted by $\|x\|_2$ or $|x|$, respectively, whereas the norm in a function space X will be denoted by $\|f\|_X$. We will be using some classical function spaces, such as the space of Schwartz functions $\mathcal{S}(\mathbb{R}^n)$ and the spaces of measurable functions $L^p(\Omega)$, without reference since they can be found in every book on functional analysis. The same holds for the classical sequence spaces ℓ^p. Probably the most important notation for this work is that of the Fourier transform $\hat{f}$ of a function $f \in \mathcal{S}(\mathbb{R}^n)$ which is defined as

$$\hat{f}(\xi) := (2\pi)^{-n/2} \int_{\mathbb{R}^n} f(x) e^{-ix\xi}\,\mathrm{d}x.$$

The inverse Fourier transform is given by $\check{f}(x) = \hat{f}(-x)$. We will also use the notation $\mathcal{F}(f)$ and $\mathcal{F}^{-1}(f)$ for the Fourier and its inverse, respectively. More facts about the Fourier transform are summarized in Appendix A.

Furthermore, we will make use of the following sets

$$\begin{aligned}
&\Omega^n := \{x \in \mathbb{R}^n : \|x\|_2 \le 1\} && \text{(unit ball in } \mathbb{R}^n\text{)}\\
&S^{n-1} := \{x \in \mathbb{R}^n : \|x\|_2 = 1\} && \text{(sphere in } \mathbb{R}^n\text{)}\\
&Z^{n-1} := S^{n-2} \times \mathbb{R} && \text{(cylinder in } \mathbb{R}^n\text{)}\\
&H(\theta, s) := \{x \in \mathbb{R}^n : x \cdot \theta = s\} && (\theta \in S^{n-1},\ s \in \mathbb{R})\\
&T^{n-1} := \{(\theta, x) : \theta \in S^{n-1},\ x \in H(\theta, 0)\} && \text{(tangent bundle of } S^{n-1}\text{)}
\end{aligned}$$

For $n = 2$, we will sometimes drop the superscripts of the above sets and simply write Ω, Z and T instead of Ω^2, Z^1 and T^1, respectively. Both, the volume (Lebesgue measure) of subsets $A \subseteq \mathbb{R}^n$ as well as the surface measure of submanifolds $M \subseteq \mathbb{R}^n$ will be denoted by $|A|$ or $|M|$, respectively. The hyperplanes $H(\theta, 0)$ will be denoted by $\theta^\perp := H(\theta, 0)$, whereas the affine hyperplanes $H(\theta, s)$ in $\mathbb{R}^2$ will be denoted by $L(\theta, s)$. Sometimes we will abuse the notation and write $\theta^\perp = (-\sin\varphi, \cos\varphi)^\intercal$ for the orthogonal unit vector $\theta = (\cos\varphi, \sin\varphi)^\intercal \in S^1$.

The spaces $L^2(Z^n)$ as well as $L^2(T^{n-1})$ are defined by the inner products

$$\langle g, h\rangle_{L^2(Z^n)} := \int_{S^{n-1}} \int_{\mathbb{R}} g(\theta, s)\overline{h(\theta, s)}\,\mathrm{d}s\,\mathrm{d}\theta,$$
$$\langle g, h\rangle_{L^2(T^{n-1})} := \int_{S^{n-1}} \int_{\theta^\perp} g(\theta, x)\overline{h(\theta, x)}\,\mathrm{d}x\,\mathrm{d}\theta,$$

where $\mathrm{d}\theta$ denotes the surface measure on S^{n-1}. The space of Schwartz functions on Z^n is defined as

$$\mathcal{S}(Z^n) := \left\{ g \in C(Z^n) : \; g(\theta, \cdot) \in \mathcal{S}(\mathbb{R}) \text{ uniformly in } \theta \in S^{n-1} \right\}.$$

In what follows, the Fourier transforms and convolutions of functions on Z^n or T^n are taken with respect to the second variable, i.e.,

$$h * g(\theta, s) = \int_{\mathbb{R}} h(\theta, s - t)g(t)\,\mathrm{d}t,$$
$$\hat{h}(\theta, \sigma) = (2\pi)^{-1/2} \int_{\mathbb{R}} h(\theta, s)e^{-is\sigma}\,\mathrm{d}s,$$

for $h, g \in \mathcal{S}(Z^n)$, and

$$h * g(\theta, x) = \int_{\theta^\perp} h(\theta, x - y)g(y)\,\mathrm{d}y, \quad x \in \theta^\perp,$$
$$\hat{h}(\theta, \omega) = (2\pi)^{-1/2} \int_{\theta^\perp} h(\theta, x)e^{-ix\omega}\,\mathrm{d}x, \quad \omega \in \theta^\perp$$

for $h, g \in \mathcal{S}(T^n)$. Further notation that is of importance for this work will be introduced at the place of its first occurrence.

2.3 Mathematics of computed tomography

In this section we will give a brief overview of some basic facts about computed tomography. Though this thesis is concerned with the two dimensional setting, the basic principles will be stated for arbitrary dimensions.

2.3.1 Radon transforms

According to Beer's law (2.1), the mathematical model for the measurement process of x-ray tomography is an integral transform which maps a function f to the set of all of its line integrals.

In the two dimensional case, this is the well known Radon transform, cf. [Rad17]. We now define the Radon transform in a multivariate setting.

Definition 2.1 (Radon transform). *The* Radon transform $\mathcal{R}f : Z^n \to \mathbb{R}$ *of a function* $f \in \mathcal{S}(\mathbb{R}^n)$ *is defined by*

$$\mathcal{R}f(\theta, s) = \int_{H(\theta,s)} f(x)\,\mathrm{d}x = \int_{\theta^\perp} f(x + s\theta)\,\mathrm{d}x. \tag{2.2}$$

⌟

In the multivariate case, there are several possibilities to define a transform that resembles (2.1). Another prominent example is the so-called x-ray transform.

Definition 2.2 (X-Ray Transform). *The* x-ray transform $\mathcal{X}f : T^{n-1} \to \mathbb{R}$ *of a function* $f \in \mathcal{S}(\mathbb{R}^n)$ *is defined by*

$$\mathcal{X}f(\theta, x) = \int_{\mathbb{R}} f(x + t\theta)\,\mathrm{d}t. \tag{2.3}$$

⌟

The x-ray transform integrates f over straight lines in $\mathbb{R}^n$. This is in contrast to the Radon transform which integrates the functions over affine hyperplanes $H(\theta, s)$. Clearly, both transforms coincide (apart from the parametrization) for $n = 2$. For $n > 2$, the following relation is valid (cf. [Nat86, Sec. II.1])

$$\mathcal{R}f(\theta, s) = \int_{H(\theta,s)\cap\eta^\perp} \mathcal{X}f(\eta, x)\,\mathrm{d}x.$$

In what follows, we use the notation $\mathcal{R}_\theta f(s) = \mathcal{R}f(\theta, s)$ and $\mathcal{X}_\theta f(x) = \mathcal{X}f(\theta, x)$ for the Radon and the x-ray transform of f, respectively. Note that $\mathcal{R}_\theta f$ and $\mathcal{X}_\theta f$ are considered as functions of the second variable. We call these functions projections of f at $\theta \in S^{n-1}$.

Remark. The x-ray and Radon transforms are special cases of the general k-plane transform, which maps a function to its integrals over k-dimensional affine subspaces, see [Kei89]. ⌟

We shall now present some basic properties of the Radon and the x-ray transform. We start by noting the obvious facts that $\mathcal{R}$ as well as $\mathcal{X}$ are linear operators and that $\mathcal{R}f$ is an even function on Z^n, i.e., $\mathcal{R}f(-\theta, -s) = \mathcal{R}f(\theta, s)$. However, the most important property of the above Radon transforms is given in the next theorem.

Theorem 2.3 (Fourier slice theorem, [Nat86, Theorem II.1.1]). *For* $f \in \mathcal{S}(\mathbb{R}^n)$ *we have*

$$\widehat{\mathcal{X}_\theta f}(\eta) = (2\pi)^{1/2}\hat{f}(\eta), \quad \eta \in \theta^\perp, \tag{2.4}$$

$$\widehat{\mathcal{R}_\theta f}(\sigma) = (2\pi)^{(n-1)/2}\hat{f}(\sigma\theta), \quad \sigma \in \mathbb{R}. \tag{2.5}$$

⌟

The importance of the Fourier slice theorem lies in the fact that it links together the Radon transforms and the Fourier transform, which is very well studied. This connection can be used to derive properties of the Radon transform from those properties which are known for the Fourier transform.

Moreover, Theorem 2.3 immediately provides a scheme for reconstructing a function from the knowledge of its Radon transform. More specifically, assume that $\mathcal{R}f_\theta(s)$ is known for all $\theta \in S^{n-1}$ and all $s \in \mathbb{R}$. Then, we can gain knowledge about the (n-dimensional) Fourier transform of f by computing the (1-dimensional) Fourier transform of the projections $\mathcal{R}_\theta f$ for all values of θ. Subsequent application of the inverse Fourier transform would yield the sought function f. Such reconstruction procedures are known as *Fourier reconstructions*, cf. [Nat86, NW01].

We proceed by noting further properties of the Radon and the x-ray transform.

Theorem 2.4 ([Nat86, Theorem II.1.2]). *For $f, g \in \mathcal{S}(\mathbb{R}^n)$ we have*

$$\mathcal{X}(f * g) = \mathcal{X}f * \mathcal{X}g, \tag{2.6}$$
$$\mathcal{R}(f * g) = \mathcal{R}f * \mathcal{R}g, \tag{2.7}$$

where the convolution on the right hand side is in Z^n or T^{n-1} (cf. Section 2.2), respectively, whereas the convolution on the left hand side denotes the usual convolution of functions in $\mathbb{R}^n$, cf. Proposition A.5. ⌟

Dual operators of $\mathcal{R}$ and $\mathcal{X}$ play also an important role in computed tomography.

Theorem 2.5 (Dual Operators, [Nat86, p. 13]). *For $g \in \mathcal{S}(Z^n)$ or $g \in \mathcal{S}(T^{n-1})$, respectively, we define the dual operators $\mathcal{R}_\theta^*, \mathcal{R}^*, \mathcal{X}_\theta^*, \mathcal{X}^*$ by*

$$\begin{aligned}
\mathcal{R}_\theta^* g(x) &= g(\theta, x \cdot \theta), \\
\mathcal{R}^* g(x) &= \int_{S^{n-1}} g(\theta, x \cdot \theta)\, \mathrm{d}\theta, \\
\mathcal{X}_\theta^* g(x) &= g(\theta, E_\theta x), \\
\mathcal{X}^* g(x) &= \int_{S^{n-1}} g(\theta, E_\theta x)\, \mathrm{d}\theta,
\end{aligned}$$

where E_θ denotes the orthogonal projection onto $\theta^\perp$. Then, for any $f \in \mathcal{S}(\mathbb{R}^n)$,

$$\begin{aligned}
\int_{\theta^\perp} \mathcal{R}_\theta f(s) g(\theta, s)\, \mathrm{d}\theta\, \mathrm{d}s &= \int_{\mathbb{R}^n} f(x) \mathcal{R}_\theta^* g(x)\, \mathrm{d}x, \\
\int_{S^{n-1}} \int_{\mathbb{R}} \mathcal{R} f(\theta, s) g(\theta, s)\, \mathrm{d}\theta\, \mathrm{d}s &= \int_{\mathbb{R}^n} f(x) \mathcal{R}^* g(x)\, \mathrm{d}x, \\
\int_{\theta^\perp} \mathcal{X}_\theta f(x) g(\theta, x)\, \mathrm{d}\theta\, \mathrm{d}x &= \int_{\mathbb{R}^n} f(x) \mathcal{X}_\theta^* g(x)\, \mathrm{d}x, \\
\int_{S^{n-1}} \int_{\theta^\perp} \mathcal{X} f(\theta, x) g(\theta, x)\, \mathrm{d}\theta\, \mathrm{d}x &= \int_{\mathbb{R}^n} f(x) \mathcal{X}^* g(x)\, \mathrm{d}x.
\end{aligned}$$

⌟

The notion of dual operators stems from integral geometry. In computed tomography the operators $\mathcal{X}^*$ and $\mathcal{R}^*$ are also called *backprojection operators*. This is because the value $\mathcal{R}^* f(x)$ is an average of all measurement values $\mathcal{R}f(\theta, x)$ which correspond to hyperplanes passing through the point $x \in \mathbb{R}^n$. A similar interpretation holds for $\mathcal{X}^* f(\theta, y)$. We have the following useful properties of backprojection operators.

Theorem 2.6 ([Nat86, Theorem II.1.3]). *For $f \in \mathcal{S}(\mathbb{R}^n)$ and $g \in \mathcal{S}(Z^n)$, $\mathcal{S}(T^{n-1})$, respectively, we have*

$$(\mathcal{X}^* g) * f = \mathcal{X}^*(g * \mathcal{X} f), \tag{2.8}$$
$$(\mathcal{R}^* g) * f = \mathcal{R}^*(g * \mathcal{R} f). \tag{2.9}$$

⌟

The following characterization of the Gram operators show that simple backprojection of the measured data does not recover the unknown object but a smoothed version of it.

Theorem 2.7 ([Nat86, Theorem II.1.5]). *For $f \in \mathcal{S}(\mathbb{R}^n)$ we have*

$$\mathcal{X}^* \mathcal{X} f = 2 \|\cdot\|_2^{1-n} * f, \tag{2.10}$$
$$\mathcal{R}^* \mathcal{R} f = \left|S^{n-2}\right| \|\cdot\|_2^{-1} * f. \tag{2.11}$$

⌟

Since the Radon transforms are used as mathematical model for the measurement process in computed tomography, it is important to know about the continuity of these transforms. In this case, the measurement process is stable, i.e., small differences of the imaged object result in small variations of the data.

Theorem 2.8 ([Nat86, Theorem II.1.6]). *All of the following linear operators are continuous:*

$$\begin{aligned}
&\mathcal{R}_\theta : L^2(\Omega^n) \to L^2([-1,1], (1-s^2)^{(1-n)/2}),\\
&\mathcal{X}_\theta : L^2(\Omega^n) \to L^2(\theta^\perp, (1-\|x\|_2^2)^{-1/2}),\\
&\mathcal{R} : L^2(\Omega^n) \to L^2(Z^n, (1-s^2)^{(1-n)/2}),\\
&\mathcal{X} : L^2(\Omega^n) \to L^2(T^{n-1}, (1-\|x\|_2^2)^{-1/2})
\end{aligned}$$

⌟

In particular, $\mathcal{R} : L^2(\Omega^n) \to L^2(Z^n)$ and $\mathcal{X} : L^2(\Omega^n) \to L^2(T^{n-1})$ are continuous operators and, in this case, their dual operators (cf. Theorem 2.5) correspond to their Hilbert space adjoints.

To prove Theorem 2.8, it is essential to assume that the functions have compact support which is contained in a bounded set $\Omega \subseteq \mathbb{R}^n$. However, there are some situations where it would be convenient to deal with functions that are supported on the whole $\mathbb{R}^n$. Unfortunately, the Radon transform is an unbounded operator on $L^2(\mathbb{R}^n)$. Though $\mathcal{R}$ is defined on a dense subset of $L^2(\mathbb{R}^n)$ (e.g. $\mathcal{S}(\mathbb{R}^n)$), there are functions $f \in L^2(\mathbb{R}^n)$, for which $\mathcal{R}f(\theta, s)$ does not exist for any $\theta \in S^{n-1}$ and any $s \in \mathbb{R}$. An example of such a function is given by (cf. [GS08])

$$f(x) = (2 + \|x\|)_2^{-\frac{n}{2}} \left(\log(2 + \|x\|)\right)^{-1}.$$

To restore continuity, we have to consider weighted L^2-spaces.

Theorem 2.9. *The Radon transform*

$$\mathcal{R} : L^2(\mathbb{R}^2, (1+\|x\|_2^2)^\alpha) \to L^2(S^1 \times \mathbb{R}, (1+s^2)^{\alpha - 1/2}). \tag{2.12}$$

is bounded for $\alpha > 1/2$. ⌟

Proof. This proof was communicated by W.R. Madych. Denote $w_\alpha(x) = (1 + \|x\|_2^2)^{\alpha/2}$. We start by estimating the modulus of $\mathcal{R}f(\theta, s)$:

$$\begin{aligned}
|\mathcal{R}f(\theta,s)| &= \left| \int_{-\infty}^{\infty} \frac{w_\alpha(s\theta + t\theta^\perp)}{w_\alpha(s\theta + t\theta^\perp)} f(s\theta + t\theta^\perp)\,\mathrm{d}t \right| \\
&\leq \int_{-\infty}^{\infty} \frac{w_\alpha(s\theta + t\theta^\perp)}{w_\alpha(s\theta + t\theta^\perp)} \left| f(s\theta + t\theta^\perp) \right| \,\mathrm{d}t \\
&\leq \left(\int_{-\infty}^{\infty} \frac{\mathrm{d}t}{w_\alpha^2(s\theta + t\theta^\perp)} \right)^{\frac{1}{2}} \left(\int_{-\infty}^{\infty} w_\alpha^2(s\theta + t\theta^\perp) \left| f(s\theta + t\theta^\perp) \right|^2 \,\mathrm{d}t \right)^{\frac{1}{2}}. \qquad (2.13)
\end{aligned}$$

We compute the first integral:

$$\begin{aligned}
\int_{-\infty}^{\infty} \frac{\mathrm{d}t}{w_\alpha^2(s\theta + t\theta^\perp)} &= \int_{-\infty}^{\infty} \frac{\mathrm{d}t}{(1 + s^2 + t^2)^\alpha} \\
&= \frac{1}{(1+s^2)^\alpha} \int_{-\infty}^{\infty} \frac{1}{\left(1 + \left(t/\sqrt{1+s^2}\right)^2\right)^\alpha} \,\mathrm{d}t \\
&= \frac{1}{(1+s^2)^{\alpha - 1/2}} \int_{-\infty}^{\infty} \frac{1}{(1+p^2)^\alpha} \,\mathrm{d}p.
\end{aligned}$$

For $\alpha > 1/2$ it holds that

$$c_\alpha := \int_{-\infty}^{\infty} \frac{1}{(1+p^2)^\alpha} \,\mathrm{d}p < \infty.$$

Hence, we further deduce from (2.13) that

$$|\mathcal{R}f(\theta,s)|^2 \,(1+s^2)^{\alpha - 1/2} \leq c_\alpha \int_{-\infty}^{\infty} w_\alpha^2(s\theta + t\theta^\perp) \left| f(s\theta + t\theta^\perp) \right|^2 \,\mathrm{d}t.$$

Therefore we get the following estimate

$$\begin{aligned}
\|\mathcal{R}f\|^2_{L^2(S^1 \times \mathbb{R}, (1+s^2)^{\alpha-1/2})} &= \int_{S^1} \int_{-\infty}^{\infty} |\mathcal{R}f(\theta,s)|^2 \,(1+s^2)^{\alpha-1/2} \,\mathrm{d}s\,\mathrm{d}\theta \\
&\leq c_\alpha \int_{S^1} \int_{-\infty}^{\infty} \int_{-\infty}^{\infty} w_\alpha^2(s\theta + t\theta^\perp) \left| f(s\theta + t\theta^\perp) \right|^2 \,\mathrm{d}t\,\mathrm{d}s\,\mathrm{d}\theta \\
&= c_\alpha \int_{S^1} \int_{\mathbb{R}^2} w_\alpha^2(x) \,|f(x)|^2 \,\mathrm{d}x\,\mathrm{d}\theta \\
&= c_\alpha |S^1| \,\|f\|^2_{L^2(\mathbb{R}^2, (1+|x|^2)^\alpha)}. \qquad \blacksquare
\end{aligned}$$

Another possibility to get rid of the assumption about the compact support is to consider L^1-spaces. In this case, we have for $f \in \mathcal{S}(\mathbb{R}^n)$,

$$\begin{aligned}
&\|\mathcal{R}f\|_{L^1(Z^n)} \leq C \,\|f\|_{L^1(\mathbb{R}^n)}, \\
&\|\mathcal{R}_\theta f\|_{L^1(\mathbb{R})} \leq C \,\|f\|_{L^1(\mathbb{R}^n)}, \\
&\|\mathcal{X}f\|_{L^1(T^{n-1})} \leq C \,\|f\|_{L^1(\mathbb{R}^n)}, \\
&\|\mathcal{X}_\theta f\|_{L^1(\theta^\perp)} \leq C \,\|f\|_{L^1(\mathbb{R}^n)},
\end{aligned}$$

where $C > 0$ may denote different constants in the above estimates. Hence, $\mathcal{R}$, $\mathcal{R}_\theta$, $\mathcal{X}$ and $\mathcal{X}_\theta$ are easily continuously extended to $L^1(\mathbb{R}^n)$.

2.3.2 Inversion formulas

In order to note the inversion formulas for the Radon transform and the x-ray transform, we first recall the definition of Riesz potentials. Let $\alpha \in \mathbb{R}$ such that $\alpha < n$. Then, the Riesz potential $\mathcal{I}^\alpha f$ of a function $f \in \mathcal{S}(\mathbb{R}^n)$ is defined as a fractional power of the Laplacian via

$$\mathcal{I}^\alpha f = (-\Delta)^{-\alpha/2} f = \mathcal{F}^{-1}(\|\cdot\|^{-\alpha} \hat{f}\,). \tag{2.14}$$

Note that, for $\alpha < n$, the function $\|\xi\|^{-\alpha}$ is locally integrable, and hence $\mathcal{F}(\mathcal{I}^\alpha f) \in L^1(\mathbb{R}^n)$. Therefore, the Riesz potential is well-defined and we have $\mathcal{I}^{-\alpha}\mathcal{I}^\alpha f = f$ for all $f \in \mathcal{S}(\mathbb{R}^n)$. For more details we refer to [Ste70]. Furthermore, if $\mathcal{I}^\alpha$ is applied to functions $g \in S(Z^n)$ or $g \in \mathcal{S}(T^{n-1})$, respectively, it is defined to act on the second variable, i.e.,

$$\mathcal{F}(\mathcal{I}^\alpha g(\theta, \cdot)) = \|\cdot\|^{-\alpha} \mathcal{F}(g(\theta, \cdot)). \tag{2.15}$$

We have the following general inversion formulas.

Theorem 2.10 ([Nat86, Theorem II.2.1]). *Let $f \in \mathcal{S}(\mathbb{R}^n)$. Then, for any $\alpha < n$, we have*

$$f = \frac{1}{2}(2\pi)^{1-n} \mathcal{I}^{-\alpha} \mathcal{R}^* \mathcal{I}^{\alpha-n+1} g, \;\; g = \mathcal{R}f, \tag{2.16}$$

$$f = \frac{1}{\left|S^{n-2}\right|}(2\pi)^{-1} \mathcal{I}^{-\alpha} \mathcal{X}^* \mathcal{I}^{\alpha-1} g, \;\; g = \mathcal{X}f. \tag{2.17}$$

⌟

For $\alpha = 0$ the inversion formulas reduce to

$$f = \frac{1}{2}(2\pi)^{1-n} \mathcal{R}^* \mathcal{I}^{1-n} g, \;\; g = \mathcal{R}f, \tag{2.18}$$

$$f = \frac{1}{\left|S^{n-2}\right|}(2\pi)^{-1} \mathcal{X}^* \mathcal{I}^{-1} g, \;\; g = \mathcal{X}f. \tag{2.19}$$

As remarked above, backprojecting the data $g = \mathcal{R}f$ is not sufficient for the recovery of f. The inversion formulas (2.18) and (2.19) reveal that the Riesz potential need to be applied to the data g before backprojecting it. This operation is usually considered as filtering of the data. For this reason, an algorithm that implements one of these inversion formulas is called *filtered backprojection (FBP)* (cf. remark at the end of Section 2.4).

Moreover, we would like to mention that for even dimensions n, the reconstruction formula (2.18) may be expressed as follows, cf. [Nat86],

$$f(x) = 2c(n) \int_0^\infty \frac{1}{q} F_x^{(n-1)}(q)\, \mathrm{d}q, \tag{2.20}$$

where $c(n) = (-1)^{n/2}(2\pi)^{-n} \left|S^{n-1}\right|$ and $F_x^{(n-1)}$ is $(n-1)$-st derivative of the function

$$F_x(q) = \frac{1}{\left|S^{n-1}\right|} \int_{S^{n-1}} \mathcal{R}f(\theta, x \cdot \theta + q)\, \mathrm{d}\theta.$$

In two dimensional setting, (2.20) is the famous inversion formula that was published by Johann Radon in 1917, [Rad17]. An English translation of the original article can be found in [Rad86].

The validity of Radon's inversion formula was studied by W.R. Madych in [Mad04]. This author shows in this work that, for functions $f \in L^p(\mathbb{R}^2)$ with $4/3 < p < 2$, the Radon transform exists almost everywhere and the Radon inversion formula holds almost everywhere in this case.

Although we are not going to consider three dimensional reconstructions in this thesis, we would like to mention that the use of the reconstruction formula (2.19) is limited in 3D because it requires the knowledge of all line integrals. However, in practice, the sources are usually restricted to a curve surrounding the object (restricted source problem). For this reason, many line integrals are not available. In this situation, Tuy's inversion formula is more appropriate.

Theorem 2.11 (Tuy's inversion formula, [Nat86, Theorem VI.5.1]). *Let Ω^3 be the unit ball in $\mathbb{R}^3$ and let $\gamma : [a, b] \to \mathbb{R}^3$ be a C^1 curve which satisfies the* Tuy's condition*, i.e., for each $x \in \Omega^3$ and each $\theta \in S^2$ there is $t = t(x, \theta)$ such that*

$$(\gamma(t) - x) \cdot \theta = 0, \quad \gamma'(t) \cdot \theta \neq 0. \tag{2.21}$$

Then, for $f \in C_c^\infty(\Omega^3)$, we have

$$f(x) = (2\pi)^{-3/2} i^{-1} \int_{S^2} (\gamma'(t) \cdot \theta)^{-1} \frac{d}{dt} \mathcal{F}\left(\mathcal{D}_{\gamma(t)} f\right)(\theta)\, \mathrm{d}\theta, \tag{2.22}$$

where $\mathcal{D}_a f$ is a function on $\mathbb{R}^3$ defined by

$$\mathcal{D}_a f(x) = \int_0^\infty f(a + tx)\, \mathrm{d}t. \qquad \lrcorner$$

The above theorem gives sufficient conditions on the acquisition process of tomographic data which guarantee a perfect reconstruction of the unknown object. Condition (2.21), known as Tuy's condition, is a very standard condition for three dimensional reconstruction. The first requirement in (2.21) ensures that for each $x \in \Omega^3$ and each plane containing x, this plane contains also some point of the curve γ, whereas the second requirement of (2.21) states that the curve γ intersects the plane transversally in that point. Interestingly, this condition can be understood in the framework of microlocal analysis and singularity detection (cf. Section 3.3).

2.3.3 Ill-posedness

In the previous subsection we have presented some inversion formulas for the Radon transform. However, for the application of these reconstruction formulas to real data, we have to assume that we are given perfect measurement data, which is not a realistic scenario because in practice the data is always corrupted by noise. Hence, it is of proper importance to know how small measurement errors are propagated through the reconstruction process. In particular, it is important to know whether inversion is stable or not, i.e., whether small measurements errors lead to small reconstruction errors. In what follows, we shall make use of standard notations and concepts of the theory of inverse problems and regularization. These are summarized for reader's convenience in Appendix C.

One possibility to study stability issues is to consider the singular value decomposition of the Radon transform. More precisely, the decay rate of the singular values gives an insight into the nature of ill-posedness of an inverse problem, cf. Theorem C.4 and subsequent remarks.

Theorem 2.12 (Singular values of the full angular Radon transform, [Nat86, Sec. IV.3]). *The singular values $\sigma_{m,l}$ of the two-dimensional Radon transform $\mathcal{R} : L^2(\Omega) \to L^2(Z, (1-s^2)^{1/2})$ are given by*

$$\sigma_{m,l} = \begin{cases} \sqrt{\frac{4\pi}{m+1}}, & |l| \le m,\ m+l \text{ even},\ m \in \mathbb{N}_0, \\ 0, & \text{otherwise}. \end{cases}$$

In particular, it holds that $\sigma_{m,l} = O(m^{-1/2})$ for $m \to \infty$. ⌟

Remarks.

1. Let $(\sigma_{m,l}; f_{m,l,k}, g_{m,l,k})$ denote the singular system for the Radon transform $\mathcal{R}$, cf. Appendix B. Then, the system $\{g_{m,l,k}\}$ of eigenfunctions of $\mathcal{R}\mathcal{R}^*$ is an orthonormal basis of $L^2(Z, (1-s^2)^{1/2})$, [Lou84]. Therefore, the operator $\mathcal{R}\mathcal{R}^*$ is compact. In turn, this implies the compactness of $\mathcal{R}$ and $\mathcal{R}^*$.
2. Theorem 2.12 is formulated with respect to the weighted L^2-space $L^2(Z, (1-s^2)^{1/2})$. However, a singular value decomposition is not known for L^2-spaces without weight. ⌟

As a consequence Theorem 2.12, we see that the problem of reconstructing a two-dimensional function from the Radon transform data is *ill-posed of order* $\frac{1}{2}$ in the sense of Definition C.5. In the context of inverse problems, this is considered to be mildly ill-posed. The same conclusion holds with respect to Definition C.6 which is based on Sobolev space estimates. To state the result, we first need to define appropriate Sobolev spaces. The Sobolev spaces $H^\alpha(\Omega)$ and $H_0^\alpha(\Omega)$, $\Omega \subseteq \mathbb{R}^n$, are defined in Appendix A.2. The spaces $H^\alpha(Z^n)$ and $H_0^\alpha(T^{n-1})$ are defined by the norms

$$\|g\|_{H^\alpha(Z^n)} = \left(\int_{S^{n-1}} \int_{\mathbb{R}} |\hat{g}(\theta,\sigma)|^2 \, (1+\sigma^2)^\alpha \, \mathrm{d}\sigma \, \mathrm{d}\theta \right)^{\frac{1}{2}},$$

$$\|g\|_{H^\alpha(T^{n-1})} = \left(\int_{S^{n-1}} \int_{\theta^\perp} |\hat{g}(\theta,\eta)|^2 \, (1+\|\eta\|_2^2)^\alpha \, \mathrm{d}\eta \, \mathrm{d}\theta \right)^{\frac{1}{2}}.$$

We can now formulate the announced result.

Theorem 2.13 ([Nat86, Theorem II.5.1]). *Let $f \in C_c^\infty(\Omega^n)$. Then, for each $\alpha \in \mathbb{R}$ there exist positive constants $c(\alpha, n)$, $C(\alpha, n)$ such that*

$$c(\alpha,n)\,\|f\|_{H_0^\alpha(\Omega^n)} \le \|\mathcal{R}f\|_{H^{\alpha+(n-1)/2}(Z^n)} \le C(\alpha,n)\,\|f\|_{H_0^\alpha(\Omega^n)}, \tag{2.23}$$

$$c(\alpha,n)\,\|f\|_{H_0^\alpha(\Omega^n)} \le \|\mathcal{X}f\|_{H^{\alpha+1/2}(T^{n-1})} \le C(\alpha,n)\,\|f\|_{H_0^\alpha(\Omega^n)}. \tag{2.24}$$

⌟

Theorem 2.13 shows that the inverse operators $\mathcal{X}^{-1}$ and $\mathcal{R}^{-1}$ are continuous as operators between $H_0^\alpha(\Omega^n)$ and $H^{\alpha+1/2}(T)$ or $H^{\alpha+(n-1)/2}(Z)$, respectively. However, there is an inherent instability in the reconstruction of f: Theorem 2.13 implies that the x-ray transform $\mathcal{X}$ smoothes by an order of $\frac{1}{2}$ measured in a Sobolev scale. Since, inversion has to reverse the smoothing, the reconstruction process is unstable. To stabilize the inversion, regularization strategies have to be applied, cf. Appendix C and references therein.

2.4 Reconstruction methods

There are basically two classes of reconstruction methods, namely direct (or analytical) and algebraic methods. In this subsection, we present the basic idea of each class of reconstruction methods. As an example for the analytic reconstruction method, we will present the classical filtered backprojection (FBP) reconstruction. Moreover, we will formulate the fully discrete reconstruction problem as a basis for the class of algebraic methods. Based on this formulation, the broad class of variational methods will be discussed.

Let us fix the notation before we start. In what follows we will deal with a practical situation where the data $y = \mathcal{R}f$ is not known precisely, but only up to an error bound $\delta > 0$. That is, we assume to be given y^δ such that

$$\left\| y - y^\delta \right\|_{L^2(Z)} \leq \delta.$$

Our goal is to recover an approximation f^δ to f from the noisy data y^δ. Thus, the practical reconstruction problem may be written in the following form

$$\mathcal{R}f^\delta = y^\delta. \tag{2.25}$$

2.4.1 Analytic reconstruction methods

The characteristic of the class of *analytic* (or direct) reconstruction methods is the fact that these methods are based on analytic reconstruction formulas and, hence, deal with continuous data.

Filtered backprojection (FBP) is clearly the most important analytic reconstruction method in computed tomography. We have already mentioned in Subsection 2.3.2 that this reconstruction method may be regarded as an implementation of the reconstruction formula (2.18), which (for $n = 2$) may be written in the following form

$$f(x) = \frac{1}{4\pi} \int_{S^1} (\mathcal{R}_\theta f * \psi)(x \cdot \theta) \, \mathrm{d}\sigma(\theta), \tag{2.26}$$

where $\psi = \mathcal{F}^{-1}(\|\cdot\|)$ (in the distributional sense). However, implementing the formula (2.26) would lead to an instable reconstruction procedure, which is due to the ill-posedness of the tomographic reconstruction problem, cf. Subsection 2.3.3. Intuitively, the source for instability is the filtering step because it amplifies high frequencies. To stabilize the inversion, a regularization strategy needs to be applied (cf. Appendix C). A standard approach is to choose a sequence of band limited functions $\{\psi_\varepsilon : \mathbb{R} \to \mathbb{R}\}_{\varepsilon>0}$ such that $\hat{\psi}_\varepsilon(\xi) \to \hat{\psi}(\xi)$ as $\varepsilon \to 0$ for all $\xi \in \mathbb{R}$. Usually, the regularization parameter ε is chosen as a function of the noise level δ such that $\varepsilon(\delta) \to 0$ as $\delta \to 0$, cf. Chapter C. Then, a regularized solution is given by

$$f^\delta(x) = \frac{1}{4\pi} \int_{S^1} (y_\theta^\delta * \psi_\varepsilon)(x \cdot \theta) \, \mathrm{d}\sigma(\theta),$$

where $y_\theta^\delta = y^\delta(\theta, \cdot)$. Since noise is a high frequency phenomenon, the idea behind this regularization strategy consists in suppressing high frequency components. A standard choice for ψ_ε is given by $\hat{\psi}_\varepsilon(\xi) = \chi_{[-1/\varepsilon, 1/\varepsilon]}(\xi) \cdot |\xi|$, which is the so-called *Ram-Lak filter*. There are many other

filters that can be used in this context. For example, the *Shepp-Logan filter*, *cosine filter*, and many more, cf. [NW01]. We note that the choice of the filter and the regularization parameter ε is essential for the reconstruction quality. The right choice should balance the amplification of noise and the measurement error. We refer to [Nat86, NW01] for more details on the filtered backprojection algorithm.

Finally, we list some more analytic reconstruction methods without explanation. *Kernel based reconstruction (summability method)* is an approximation theoretic approach that was introduced in [Mad90]. A related technique is the method of *approximate inverse* that may also be applied to tomographic reconstruction [LM90], [Sch07]. Moreover, we mention the *Fourier reconstruction techniques* that are direct applications of the Fourier slice theorem (cf. Theorem 2.3 and subsequent remarks), cf. [NW01].

2.4.2 Algebraic reconstruction methods

Another large class of reconstruction methods is the class algebraic reconstruction methods. This class again splits into many different subclasses of algorithms. Describing all of them would go beyond the scope of this thesis. We present only the basic idea of these methods.

In contrast to analytic methods, algebraic approaches are based on a fully discrete formulation of the reconstruction problem. In this setting, the sought function f^δ is discretized right from the beginning by using some basis functions $\{\varphi_n\}$. That is, f^δ is assumed to be given as a finite linear combination of these basis functions,

$$f^\delta(x) = \sum_{n=1}^{N} c_n \varphi_n(x), \tag{2.27}$$

where $c \in \mathbb{R}^N$, $N \in \mathbb{N}$, is the coefficient vector with respect to $\{\varphi_n\}$. In the next discretization step we assume to be given a finite number of measurements $y_m^\delta = \mathcal{R}f^\delta(\theta_m, s_m)$, $1 \leq m \leq M \in \mathbb{N}$. Then, each measurement is given by

$$y_m^\delta = \sum_{n=1}^{N} c_n \mathcal{R}\varphi_n(\theta_m, s_m).$$

Thus, the fully discrete version of the reconstruction problem (2.25) is given by the linear system of equations

$$R \cdot c = y^\delta, \tag{2.28}$$

where $R = (r_{m,n}) \in \mathbb{R}^{M \times N}$ is the so-called *system matrix* whose entries are given by

$$r_{m,n} = \mathcal{R}\varphi_n(\theta_m, s_m).$$

Note that the discrete reconstruction problem (2.28) is formulated with respect to the coefficient vector $c \in \mathbb{R}^N$. That is, in this case we aim at reconstructing the vector c rather than f^δ.

Of course there are many algorithms for solving linear equations like (2.28). In practice, one of the most popular methods is the so-called algebraic reconstruction technique (ART), which is an implementation of the Kaczmarz method, and its variants SART (simultaneous algebraic reconstruction) and SIRT (simultaneous iterative reconstruction) [Her80], [KS88], [NW01].

Remark. The nomenclature "algebraic reconstruction" is not consistently used in the literature. In this thesis, we will use this term to refer to methods which are designed for solving the algebraic equation (2.28). At this point, we have to point out that the term algebraic reconstruction is often used to refer to the methods ART, SART, and SIRT. ⌟

In designing reconstruction algorithms based on (2.28), one still has to consider the ill-posedness of the reconstruction problem and use regularization strategies. In its standard formulation, the methods ART, SART and SIRT do not incorporate any regularization strategy.

Usually, stabilization of the inversion is achieved by incorporating prior knowledge into the reconstruction procedure. A very flexible way for doing this is offered by the *statistical reconstruction*. In this setting, the unknown coefficient vector c as well as the measurement vector y^δ are considered to be realizations of some random variables. In order to formulate the statistical reconstruction problem one has to model the likelihood density $\pi(y|c)$ and the prior-density $\pi(c)$. The likelihood-density $\pi(y|c)$ is a statistical model for the measurement process, whereas the prior-density $\pi(c)$ encodes the a priori information. The solution of the statistical reconstruction results in determining the posterior-density $\pi(c|y)$. To compute an explicit solution of the problem (2.28) a statistical estimator is used. For more details, we refer to [KSJ+03], [SKJ+03], [BLZ08] and [KS05], [CS11].

Another very general setting for regularized reconstruction can be formulated in the framework of variational regularization. In this case, the solution of the equation (2.28) is computed by minimizing a Tikhonov type functional

$$c_\alpha = \underset{c\in\mathbb{R}^N}{\arg\min} \left\| R\cdot c - y^\delta \right\|_2^2 + \alpha\cdot\Lambda(c), \tag{2.29}$$

where $\alpha > 0$ is a regularization parameter and $\Lambda : \mathbb{R}^N \to [0,\infty]$ is a *prior (or penalty) function*. The first term in (2.29) (data fidelity term) controls the data error, whereas the second term encodes the prior information about the unknown object. It can be shown that the variational approach is a regularization strategy, cf. Appendix C. For more details on variational regularization, we refer to [SGG+09].

We would like to note that the choice among the various prior terms and, thus, regularization techniques, depends on the specific object (which is imaged) and, to some extent, on the desire to preserve or emphasize particular features of the unknown object. A possible choice for Ψ may be any kind of a smoothness (semi-) norm [SGG+09]. For instance, the Besov norm allows to adjust the smoothness of the solution at a very fine scale [KSJ+03], [LT08], [RVJ+06]. Another prominent example in image reconstruction is the total variation (TV) seminorm. This seminorm is a smoothness norm that is particularly used for edge-preserving reconstructions [FP11], [HSP11], [HHK+12].

Algebraic approaches and, in particular, variational reconstruction methods enjoy great popularity in image reconstruction. This is based on fact that the algebraic formulation of the reconstruction problem offers high flexibility. More precisely, the solution of the equation (2.28) allows the integration of a priori information and does not depend on the specific acquisition geometry which is in contrast to the FBP method.

CHAPTER 3

Characterization of limited angle reconstructions and artifact reduction

In this chapter, we turn our attention to the study of the limited angle reconstruction problem. In this case, the tomographic data $\mathcal{R}f(\theta, s)$ is no longer available for all $\theta \in S^1$, but is known only on a restricted subset of S^1. Problems of this type arise naturally in practical applications, such as digital breast tomosynthesis [N$^+$97], electron microscopy [DRK68], or dental tomography [HKL$^+$10], [MS12]. Many of these modalities still employ the filtered backprojection (FBP) algorithm for practical reconstructions, cf. [PSV09], [LMKH08], [SMB03], [IG03], [SFS06], [III09]. However, since the FBP algorithm implements an inversion formula for the Radon transform, cf. Section 2.4, an essential requirement for its application is the completeness of tomographic data. Consequently, the application of the FBP algorithm is theoretically not justified in limited angle tomography. Moreover, only specific features of the original object can be reconstructed reliably from limited angle data, [Qui93], and additional artifacts can be created in FBP reconstructions, cf. Figure 3.1.

In the present chapter, we solve the above issues and provide a detailed analysis of reconstructions at a limited angular range. Specifically, we focus on the following topics:

- Characterization of classical reconstructions at a limited angular range,
- Characterization of the information content of limited angle data and in particular of those features that can be reconstructed from a limited angular range,
- Characterization and reduction of artifacts in filtered backprojection reconstructions from a limited angular range,
- Stabilization strategy for limited angle tomography.

In Section 4.3, we begin our investigations by studying the backprojection of limited angle data and prove a characterization of the kernel of the limited angle Radon transform in the Schwartz space $\mathcal{S}(\mathbb{R}^2)$, cf. Theorem 3.6 and Corollary 3.7. Subsequently, we derive an exact formula for filtered backprojection reconstructions at a limited angular range in Theorem 3.9 and justify the application of the FBP algorithm to limited angle data under suitable assumptions on the target functions. An interpretation of these results in terms of visible and invisible singularities is given in Section 3.3. In particular, we show that a meaningful a-priori information can be extracted from

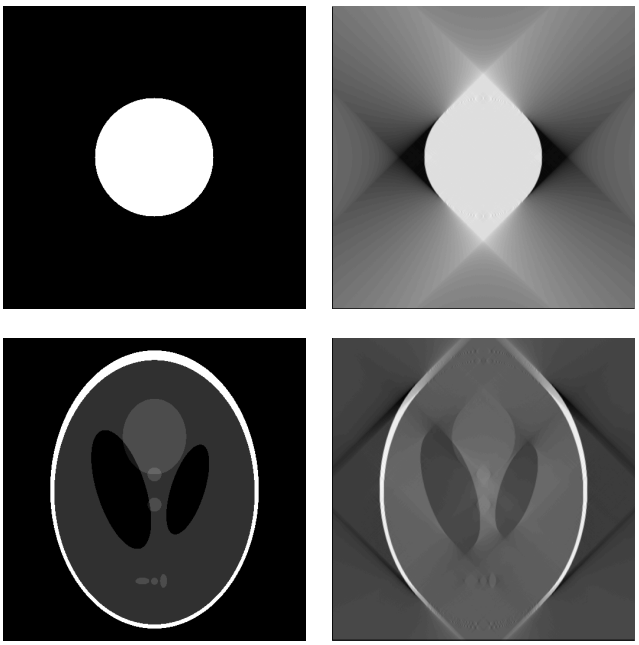

Figure 3.1: Original images (left) and FBP reconstructions at limited angular range $[-\Phi, \Phi]$, $\Phi = 45°$ (right). As a consequence of the limited angular range, only specific features of the original object can be reconstructed, and some streak artifacts are generated.

limited angle data. In Section 3.4, we prove a microlocal characterization of limited angle artifacts that are generated by the filtered backprojection algorithm, Theorem 3.24, and develop an artifact reduction strategy for the FBP algorithm, Theorem 3.26. We also illustrate the proposed method in some numerical experiments. Finally, we show that the existence of invisible singularities at limited angular range entails severe ill-posedness of limited angle tomography, and derive a stabilization strategy in Section 3.5.

3.1 Notations and basic definitions

In what follows, we assume that the data $\mathcal{R}f(\theta, s)$ is known only for $(\theta, s) \in S^1_\Phi \times \mathbb{R}$, where the *angular range parameter* Φ satisfies $0 < \Phi < \pi/2$, and $S^1_\Phi \subsetneq S^1$ is given by (cf. Figure 3.2)

$$S^1_\Phi := S^{1,+}_\Phi \cup S^{1,-}_\Phi, \quad S^{1,\pm}_\Phi := \left\{\theta \in S^1 : \theta = \pm(\cos\varphi, \sin\varphi)^T, |\varphi| \leq \Phi\right\}. \tag{3.1}$$

In order to compute a reconstruction, we consequently have to invert the restricted or the *limited angle Radon transform*

$$\mathcal{R}_\Phi : f \mapsto \mathcal{R}f|_{S^1_\Phi \times \mathbb{R}}. \tag{3.2}$$

Hence, the practical *limited angle reconstruction problem* reads

$$\text{given } y^\delta = \mathcal{R}_\Phi f + \eta, \qquad \text{find an approximation to } f, \tag{3.3}$$

where η denotes the noise component with $\|\eta\|_{L^2(Z)} < \delta$ and $\delta > 0$.

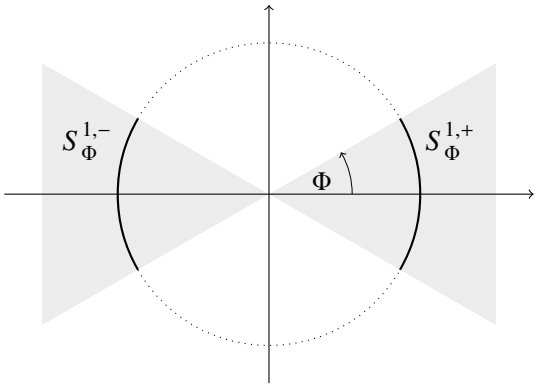

Figure 3.2: The figure shows $S_\Phi^1 = S_\Phi^{1,+} \cup S_\Phi^{1,-}$ (solid line) as a subset of S^1 (dotted line). The wedge $W_\Phi = \mathbb{R} \cdot S_\Phi^1$ is indicated by the gray shaded area.

In the context of tomographic reconstruction at a limited angular, the backprojection operator (or dual operator) $\mathcal{R}_\Phi^*$ plays an important role. Analogously to Theorem 2.5, we have the following representation.

Theorem 3.1. *Let $0 \le \Phi \le \pi/2$. For $g \in Z_\Phi = S_\Phi^1 \times \mathbb{R}$ we define the backprojection operator of the limited angle Radon transform $\mathcal{R}_\Phi$ by*

$$\mathcal{R}_\Phi^* g(x) = \int_{S_\Phi^1} g(\theta, x \cdot \theta)\, \mathrm{d}\theta. \tag{3.4}$$

Then, for $f \in \mathcal{S}(\mathbb{R}^2)$,

$$\int_{S_\Phi^1} \int_{\mathbb{R}} \mathcal{R}_\Phi f(\theta, s) g(\theta, s)\, \mathrm{d}\theta\, \mathrm{d}s = \int_{\mathbb{R}^2} f(x) \mathcal{R}_\Phi^* g(x)\, \mathrm{d}x$$ ⌟

Note that many properties, such as continuity, evenness, etc., carry over from the full angular Radon transform the case of the limited angle Radon transform.

3.2 Characterizations of limited angle reconstructions

The objective of this section is to understand the nature of limited angle tomography. Of proper interest are the following questions: How much information about the unknown function is contained in the limited angle data? Which features of the sought function can be reconstructed reliably using a limited angle data set? In this section we are going to partly answer these questions by characterizing reconstructions that are obtained via FBP and algebraic reconstructions.

We start by examining the information content of the limited angle data. To this end, we use the Fourier slice theorem (Theorem 2.3) in order to relate the data $y = \mathcal{R}_\Phi f$ to the Fourier transform of f. For this purpose, we first note that the limited angle Radon transform $\mathcal{R}_\Phi f$ can be extended to the cylinder $Z = S^1 \times \mathbb{R}$ by setting $\mathcal{R}_\Phi f(\theta, s) = \chi_{S_\Phi^1}(\theta) \cdot \mathcal{R} f(\theta, s)$. In this context, we have

$\hat{f}(s\theta) = \mathcal{F}(\mathcal{R}_\Phi f(\theta,\cdot))(s)$ if $\theta \in S^1_\Phi$, and $\hat{f}(s\theta) = \mathcal{F}(\mathcal{R}_\Phi f(\theta,\cdot))(s) = 0$ if $\theta \notin S^1_\Phi$. Therefore, the limited angle Radon transform acts as a truncation operator in the Fourier domain, and we have

$$\mathcal{R}_\Phi f = \mathcal{R}_\Phi(P_\Theta f), \text{ for all } \Phi \le \Theta \le \frac{\pi}{2},$$

where $P_\Theta f = \mathcal{F}^{-1}(\chi_{W_\Theta}\hat{f}\,)$ and χ_{W_Θ} is the characteristic function of the wedge $W_\Theta = \mathbb{R}\cdot S^1_\Theta$.

In view of the above discussion, the limited angle data $g = \mathcal{R}_\Phi f$ contains only the information about the two dimensional Fourier transform $\hat{f}$ on the polar wedge W_Φ, which is defined by, cf. Figure 3.2,

$$W_\Phi := \mathbb{R}\cdot S^1_\Phi = \left\{ r\cdot\theta :\ \theta \in S^1_\Phi, r\in\mathbb{R}\right\}. \tag{3.5}$$

Consequently, a minimum requirement on a reconstruction algorithm for limited angle tomography should be the ability to provide reconstructions f_{rec} whose Fourier transform coincides with the Fourier transform of the sought function f on the wedge W_Φ. That is, the reconstructions should satisfy $\hat{f}_{\text{rec}}|_{W_\Phi} = \hat{f}|_{W_\Phi}$. Since many practical applications still employ the filtered backprojection (FBP) algorithm for reconstruction at a limited angular range, it is important to understand whether the FBP meets this requirement.

In what follows, we turn our attention to the characterization of FBP reconstructions at a limited angular range. To this end, let us recall that the FBP algorithm implements the inversion formula $f = 1/(4\pi)\mathcal{R}^*\mathcal{I}^{-1}\mathcal{R}f$, which by Theorem 2.10 is equal to $f = 1/(4\pi)\mathcal{I}^{-1}\mathcal{R}^*\mathcal{R}f$. According to that, we see that the (limited angle) Gram operator $\mathcal{R}^*_\Phi\mathcal{R}_\Phi$ plays an important role in this context. For the problem of image reconstruction at a limited angular range, it is therefore important to have a characterization of $\mathcal{R}^*_\Phi\mathcal{R}_\Phi$.

The content of the next theorem is a generalization of Theorem 2.7 to the setting of limited angle tomography.

Theorem 3.2. *Let $0 \le \Phi \le \pi/2$ and $f \in \mathcal{S}(\mathbb{R}^2)$. Then,*

$$\mathcal{R}^*_\Phi\mathcal{R}_\Phi f = 2\cdot\frac{\chi_{W^\perp_\Phi}}{\|\cdot\|_2} * f, \tag{3.6}$$

where $\chi_{W^\perp_\Phi}$ is the characteristic function of the polar wedge

$$W^\perp_\Phi = \left\{\xi\in\mathbb{R}^2 :\ \theta\cdot\xi = 0 \text{ for some } \theta\in W_\Phi\right\}.$$

Proof. We use (3.4) to compute

$$\begin{aligned}
\mathcal{R}^*_\Phi\mathcal{R}_\Phi f(x) &= \int_{S^1_\Phi} \mathcal{R}_\Phi f(\theta, x\cdot\theta)\,\mathrm{d}\theta,\\
&= \int_{S^1_\Phi}\int_{\mathbb{R}} f((x\cdot\theta)\theta + t\theta^\perp)\,\mathrm{d}t\,\mathrm{d}\theta,\\
&= \int_{S^1_\Phi}\int_{\mathbb{R}} f(x + t\theta^\perp)\,\mathrm{d}t\,\mathrm{d}\theta.
\end{aligned}$$

The last equations holds true because $(-x + (x \cdot \theta)\theta) \perp \theta$, whence $(x \cdot \theta)\theta = x + t_0 \cdot \theta^\perp$ for some $t_0 \in \mathbb{R}$, where $\theta^\perp = (-\theta_2, \theta_1)$ denotes an orthogonal vector to $\theta = (\theta_1, \theta_2)$. Using the symmetry of the above integral we further get with $y = t\theta$,

$$\begin{aligned}\mathcal{R}_\Phi^* \mathcal{R}_\Phi f(x) &= \int_{(S^1_\Phi)^\perp} \int_{-\infty}^{\infty} f(x + t\theta)\, \mathrm{d}t\, \mathrm{d}\theta \\ &= 2 \cdot \int_{\mathbb{R}^2} f(x + y) \frac{\chi_{W_\Phi^\perp}(y)}{\|y\|_2}\, \mathrm{d}y \\ &= 2 \cdot \left(\frac{\chi_{W_\Phi^\perp}}{\|\cdot\|_2} * f \right)(x). \end{aligned}$$

∎

In the following, we shall use Theorem 3.2 in order to derive a representation of the Gram operator $\mathcal{R}_\Phi^* \mathcal{R}_\Phi$ in the Fourier domain. For this purpose, we first note some auxiliary results.

Proposition 3.3. *Let $b > 0$ and $\delta_\pm^b$ be the function defined by*

$$\delta_\pm^b(x) = \frac{1}{2\pi} \int_{-b}^{b} e^{\pm i x \cdot \xi}\, \mathrm{d}\xi. \tag{3.7}$$

For $c, d \in \mathbb{R} \cup \{-\infty, \infty\}$, $c < d$, let $\varphi \in L^1((c,d))$ such that $\varphi \in C^1(B_\varepsilon(0))$, where $B_\varepsilon(0) = [-\varepsilon, \varepsilon] \cap [c,d]$ for some $\varepsilon > 0$. Then, we have

$$\lim_{b\to\infty} \int_c^d \delta_\pm^b(x)\varphi(x)\, \mathrm{d}x = \chi_{[c,d]}(0) \cdot \begin{cases} \frac{1}{2} \cdot \varphi(0+), & c = 0, \\ \frac{1}{2} \cdot \varphi(0-), & d = 0, \\ \varphi(0), & \textit{else}. \end{cases} \tag{3.8}$$

⌟

Proof. A simple calculation yields

$$\delta_\pm^b(x) = \frac{1}{\pi} \frac{\sin(bx)}{x}.$$

To show the assertion we first assume that either $c > 0$ or $d < 0$. In both cases, the function $g(x) := \chi_{(c,d)}(x) \cdot \varphi(x)/x$ is in $L^1(\mathbb{R})$ and it follows from the Riemann-Lebesgue Lemma, cf. Appendix A, that

$$\lim_{b\to\infty} \int_c^d \delta_\pm^b(x)\varphi(x)\, \mathrm{d}x = \frac{1}{\pi} \lim_{b\to\infty} \int_{\mathbb{R}} \sin(bx) g(x)\, \mathrm{d}x = \sqrt{\frac{2}{\pi}} \lim_{b\to\infty} \mathrm{Im}(\hat{g}(b)) = 0. \tag{3.9}$$

Next, we consider the cases $c = 0$ and $d = 0$. Because

$$\int_c^0 \delta_\pm^b(x)\varphi(x)\, \mathrm{d}x = \int_0^{-c} \delta_\pm^b(x)\varphi(-x)\, \mathrm{d}x,$$

we may assume without loss of generality that $c = 0$ and $d > 0$. Then, it follows from (3.9) that

$$\lim_{b\to\infty} \int_0^d \delta_\pm^b(x)\varphi(x)\, \mathrm{d}x = \lim_{b\to\infty} \left(\int_0^\varepsilon + \int_\varepsilon^d \right) \delta_\pm^b(x)\varphi(x)\, \mathrm{d}x = \lim_{b\to\infty} \int_0^\varepsilon \delta_\pm^b(x)\varphi(x)\, \mathrm{d}x$$

for some $\varepsilon > 0$. By assumption, φ can be extended to a continuously differentiable function $\widetilde{\varphi}$ on the closed interval $[0, \varepsilon]$ such that we can use the Taylor expansion, $\widetilde{\varphi}(x) = \widetilde{\varphi}(0) + \widetilde{\varphi}'(\xi_x)x$ with $x \in [0, \varepsilon)$ and $\xi_x \in [0, x]$. By assumption, the derivative $\widetilde{\varphi}'$ is bounded and, hence, it follows that $\widetilde{\varphi}'(\xi_x)$ is integrable. Using the Riemann-Lebesgue Lemma we get

$$\begin{aligned}\lim_{b\to\infty} \int_0^\varepsilon \delta_\pm^b(x)\varphi(x)\,\mathrm{d}x &= \lim_{b\to\infty} \int_0^\varepsilon \delta_\pm^b(x)\widetilde{\varphi}(x)\,\mathrm{d}x \\ &= \frac{\widetilde{\varphi}(0)}{\pi} \lim_{b\to\infty} \int_0^\varepsilon \frac{\sin(bx)}{x}\,\mathrm{d}x + \frac{1}{\pi} \lim_{b\to\infty} \int_0^\varepsilon \sin(bx)\widetilde{\varphi}'(\xi_x)\,\mathrm{d}x \\ &= \frac{\widetilde{\varphi}(0)}{\pi} \lim_{b\to\infty} \int_0^{b\varepsilon} \frac{\sin(x)}{x}\,\mathrm{d}x.\end{aligned}$$

The asymptotics for the sine integral, $\lim_{x\to\infty} \int_0^x \sin t/t\,\mathrm{d}t = \pi/2$, yield

$$\lim_{b\to\infty} \int_0^\varepsilon \delta_\pm^b(x)\varphi(x)\,\mathrm{d}x = \frac{1}{2} \cdot \widetilde{\varphi}(0) = \frac{1}{2} \cdot \varphi(0+). \tag{3.10}$$

Finally, if $0 \in (c, d)$ we consider $(c, d) = (c, -\varepsilon] \cup (-\varepsilon, \varepsilon) \cup [\varepsilon, d)$ and use (3.9) to get

$$\begin{aligned}\frac{1}{\pi} \lim_{b\to\infty} \int_c^d \frac{\sin(bx)}{x}\varphi(x)\,\mathrm{d}x &= \frac{1}{\pi} \lim_{b\to\infty} \left(\int_c^{-\varepsilon} + \int_{-\varepsilon}^{\varepsilon} + \int_\varepsilon^d \right) \frac{\sin(bx)}{x}\varphi(x)\,\mathrm{d}x \\ &= \frac{1}{\pi} \lim_{b\to\infty} \int_{-\varepsilon}^{\varepsilon} \frac{\sin(bx)}{x}\varphi(x)\,\mathrm{d}x \\ &= \frac{1}{\pi} \lim_{b\to\infty} \int_0^{\varepsilon} \frac{\sin(bx)}{x}(\varphi(x) + \varphi(-x))\,\mathrm{d}x.\end{aligned}$$

Now, we can apply (3.10) to the function $(\varphi(x) + \varphi(-x))$ to get

$$\frac{1}{\pi} \lim_{b\to\infty} \int_c^d \frac{\sin(bx)}{x}\varphi(x)\,\mathrm{d}x = \varphi(0). \qquad \blacksquare$$

As a consequence of Proposition 3.3 we get the following result, which is well known in the classical Fourier analysis.

Corollary 3.4. *Let $b > 0$ and $\delta_\pm^b$ as in Proposition 3.3. Then, $\delta_\pm^b \to \delta$ in $\mathcal{S}'(\mathbb{R})$ as $b \to \infty$, i.e., for each $\varphi \in \mathcal{S}(\mathbb{R})$ we have*

$$\lim_{b\to\infty} \int_{\mathbb{R}} \delta_\pm^b(x)\varphi(x)\,\mathrm{d}x = \varphi(0). \tag{3.11}$$

⌟

Remark. The classical proof of Corollary 3.4 is more succinct than the proof of Proposition 3.3. It is based on the L^2-Theory of the Fourier transform. In this case, the crucial observation is that $\delta_\pm^b \in L^2(\mathbb{R})$ and $\hat{\delta}_\pm^b(\xi) = \frac{1}{\sqrt{2\pi}}\chi_{[-b,b]}$ in $L^2(\mathbb{R})$. Then, the assertion follows by applying Parseval's identity (cf. Proposition A.4),

$$\lim_{b\to\infty} \int_{\mathbb{R}} \delta_\pm^b(x)f(x)\,\mathrm{d}x = \lim_{b\to\infty} \int_{\mathbb{R}} \hat{\delta}_\pm^b(\xi)\hat{f}(\xi)\,\mathrm{d}\xi = \frac{1}{\sqrt{2\pi}} \int_{\mathbb{R}} \hat{f}(\xi)\,\mathrm{d}\xi = f(0).$$

Another essential ingredient in the classical proof is the continuity of test functions around the origin. In our setting, however, we neither suppose the test functions to be continuous around the origin nor we assume the test functions to belong to an L^2-space. Therefore, the classical proof (as stated above) cannot be applied directly in our situation. The setting of Proposition 3.3 will be used to prove Theorem 3.6. ⌟

Lemma 3.5. *Let $f : [-1, 1] \to \mathbb{R}$ be bounded and integrable. Then, for any $\eta \in S^1$,*

$$\int_{S^1} f(\eta \cdot \xi)\, \mathrm{d}\xi = 2 \int_{-1}^{1} \frac{f(t)}{\sqrt{1-t^2}}\, \mathrm{d}t. \tag{3.12}$$

⌟

Proof. The assertion is a special case of the well known Funk-Hecke theorem, cf. [Gro96, Theorem 3.4.1]. ∎

We are now able to characterize the action of the operator $\mathcal{R}_\Phi^* \mathcal{R}_\Phi$ in the Fourier domain.

Theorem 3.6. *Let $0 \le \Phi \le \pi/2$ and $f \in \mathcal{S}(\mathbb{R}^2)$. Then,*

$$\mathcal{F}(\mathcal{R}_\Phi^* \mathcal{R}_\Phi f)(\xi) = 4\pi \frac{\chi_{W_\Phi}(\xi)}{\|\xi\|_2} \hat{f}(\xi), \tag{3.13}$$

for almost all $\xi \in \mathbb{R}^2$. ⌟

Proof. We use the representation (3.6) to compute the Fourier transform of $\mathcal{R}_\Phi^* \mathcal{R}_\Phi f$. Using the convolution theorem for the Fourier transform, Proposition A.15, we first note that

$$\mathcal{F}\left(\mathcal{R}_\Phi^* \mathcal{R}_\Phi f\right) = 4\pi \cdot \mathcal{F}(\chi_{W_\Phi^\perp} \|\cdot\|_2^{-1}) \cdot \hat{f}. \tag{3.14}$$

It is therefore sufficient to compute the (distributional) Fourier transform of $T := (\chi_{W_\Phi^\perp} \|\cdot\|_2^{-1})$. To this end, we further note that T can be written as $T = T_b + R_b$ with $T_b = \chi_{\{|x| \le b\}} T \in L^1(\mathbb{R}^2)$ and $R_b = \chi_{\{|x|>b\}} T \in L^2(\mathbb{R}^2)$, $b > 0$. This means that T an element of $L^1(\mathbb{R}^2) + L^2(\mathbb{R}^2)$ and, therefore, the distributional Fourier transform of T belongs to $C_0(\mathbb{R}^2) + L^2(\mathbb{R}^2)$. In particular, $\widehat{T} \in L^1_{\mathrm{loc}}(\mathbb{R}^2)$.

On the other hand, the pointwise convergence $T_b \to T$, $b \to \infty$, implies the distributional convergence $T_b \to T$ in $\mathcal{S}'(\mathbb{R}^2)$ as $b \to \infty$. In turn, the continuity of the Fourier transform in $\mathcal{S}'$ entails the convergence $\widehat{T_b} \to \widehat{T}$ in $\mathcal{S}'(\mathbb{R}^2)$.

In summary, the above considerations show that in order to compute the distributional Fourier transform of T, it is sufficient to compute the pointwise limit $\lim_{b\to\infty} \widehat{T_b}(\xi)$, where $\widehat{T_b}$ denotes the ordinary Fourier transform.

To do so, we evaluate the Fourier transform $\widehat{T} \in L^1_{\mathrm{loc}}(\mathbb{R}^2)$ using polar coordinates $\xi = r\theta$, $r > 0$, and $\theta \in S^1$,

$$\mathcal{F}\left(\frac{\chi_{W_\Phi^\perp}}{\|\cdot\|_2}\right)(r\theta) = \frac{1}{2\pi} \lim_{b\to\infty} \int_{\{\|x\|_2 \le b\}} \frac{\chi_{W_\Phi^\perp}(x)}{\|x\|_2} e^{-irx\cdot\theta}\, \mathrm{d}x. \tag{3.15}$$

In addition, we also use polar coordinates $x = s\zeta$, $s \in \mathbb{R}$, and $\zeta \in S^{1,+}_{\Phi}$, cf. (3.1), to evaluate the integral on the right-hand side. To this end, note that $W^{\perp}_{\Phi} = \mathbb{R} \cdot A_{\Phi}$, where

$$A_{\Phi} = \left\{\theta \in S^1 : \theta = (\cos\varphi, \sin\varphi)^T, |\varphi - \pi/2| \leq \Phi\right\}$$

is the rotation of $S^{1,+}_{\Phi}$ by $\pi/2$ (cf. (3.1)). Then,

$$\begin{aligned}\mathcal{F}\left(\frac{\chi_{W^{\perp}_{\Phi}}}{\|\cdot\|_2}\right)(r\theta) &= \frac{1}{2\pi}\lim_{b\to\infty}\int_{A_{\Phi}}\int_{-b}^{b}\frac{1}{\|s\zeta\|_2}e^{-irs\zeta\cdot\theta}\,|s|\;\mathrm{d}s\,\mathrm{d}\zeta \\ &= \lim_{b\to\infty}\int_{S^1}\chi_{A_{\Phi}}(\zeta)\,\delta^b(r\zeta\cdot\theta)\;\mathrm{d}\zeta.\end{aligned}$$

Now let

$$m(\theta) = \inf_{\zeta\in A_{\Phi}}(\zeta\cdot\theta) \text{ and } M(\theta) = \sup_{\zeta\in A_{\Phi}}(\zeta\cdot\theta).$$

Then,

$$\mathcal{F}\left(\frac{\chi_{W^{\perp}_{\Phi}}}{\|\cdot\|_2}\right)(r\theta) = \frac{1}{2}\lim_{b\to\infty}\int_{S^1}\chi_{[m(\theta),M(\theta)]}(\zeta\cdot\theta)\,\delta^b(r\zeta\cdot\theta)\;\mathrm{d}\zeta.$$

Applying Lemma 3.5 to the function $f(t) = \chi_{[m(\theta),M(\theta)]}(t)\,\delta^b(rt)$ and substituting $x = rt$, we get

$$\mathcal{F}\left(\frac{\chi_{W^{\perp}_{\Phi}}}{\|\cdot\|_2}\right)(r\theta) = \lim_{b\to\infty}\int_{rm(\theta)}^{rM(\theta)}\delta^b(x)\frac{1}{\sqrt{r^2-x^2}}\,\mathrm{d}x \tag{3.16}$$

and by Proposition 3.3 we eventually deduce

$$\mathcal{F}\left(\frac{\chi_{W^{\perp}_{\Phi}}}{\|\cdot\|_2}\right)(r\theta) = C(\theta)\cdot\chi_{[m(\theta),M(\theta)]}(0)\cdot\frac{1}{r},$$

where $C(\theta) \in \{1/2, 1\}$, according to (3.8). Now it is easy to see that,

$$C(\theta)\cdot\chi_{[m(\theta),M(\theta)]}(0) = \chi_{S^1_{\Phi}}(\theta)\cdot\begin{cases}1/2, & \theta\in\partial W_{\Phi}\cap S^1\\ 1, & \text{otherwise}\end{cases}, \tag{3.17}$$

where S^1_{Φ} is defined in (3.1). Now note that the right hand side in (3.17) is equal to $\chi_{S^1_{\Phi}}$ almost everywhere, and $W_{\Phi} = \mathbb{R}\cdot S^1_{\Phi}$. Hence, the assertion follows from (3.14) together with

$$\mathcal{F}\left(\frac{\chi_{W^{\perp}_{\Phi}}}{\|\cdot\|_2}\right)(\xi) = \frac{\chi_{W_{\Phi}}(\xi)}{\|\xi\|_2}.$$

∎

Remark. It was communicated by E. T. Quinto that a similar version of the Theorem 3.6 was published in [Tuy81]. However, Theorem 3.6 and its proof that we presented here were developed without knowledge of this work.

An inspection of [Tuy81] shows that both proofs follows a similar idea, whereas our realization seems to be more elementary and complete in its argumentation. More precisely, the author of [Tuy81] arrives at an expression which is similar to (3.16) (by using a different technique) and concludes the proof by simply noting that $\delta^b \to \delta$ in $\mathcal{S}'(\mathbb{R}^2)$ as $b \to 0$, cf. [Tuy81, p. 610]. This

argumentation is however incomplete, since on the one hand the function $(r^2 - x^2)^{-1/2}$ does not belong to $\mathcal{S}(\mathbb{R}^2)$ and, on the other hand, the evaluation of the limit

$$\lim_{b\to\infty} \int_c^d \delta^b(x) \frac{1}{\sqrt{r^2 - x^2}} \, \mathrm{d}x$$

depends on the interval of integration $[c, d]$. Moreover, the convergence $\delta^b \to \delta$ in $\mathcal{S}'(\mathbb{R}^2)$ does not imply the Proposition 3.3 (cf. remark after Corollary 3.4). In contrast to the proof of H. Tuy, we have treated both of these issues in Proposition 3.3, which was an essential ingredient for the proof of Theorem 3.6. ⌟

As an immediate consequence of Theorem 3.6 we note the following null space characterization of the Gram operator $\mathcal{R}_\Phi^* \mathcal{R}_\Phi$ and the limited angle Radon transform.

Corollary 3.7. *Let $f \in \mathcal{S}$ such that* $\operatorname{supp} \hat{f} \subseteq \mathbb{R}^2 \setminus W_\Phi$*, then $\mathcal{R}_\Phi^* \mathcal{R}_\Phi f \equiv 0$ and $\mathcal{R}_\Phi f \equiv 0$.* ⌟

If we consider the limited angle Radon transform as an operator between Schwartz spaces, i.e., $\mathcal{R}_\Phi : \mathcal{S}(\mathbb{R}^2) \to \mathcal{S}(S^1_\Phi \times \mathbb{R})$, then Corollary 3.7 implies that

$$\ker(\mathcal{R}_\Phi) = \ker\left(\mathcal{R}_\Phi^* \mathcal{R}_\Phi\right) = \left\{ f \in \mathcal{S}(\mathbb{R}^2) : \operatorname{supp} \hat{f} \subseteq W_\Phi \right\}.$$

In view of the limited angle reconstruction problem, this result also characterizes functions that can be perfectly reconstructed from a limited angle data set. These are those functions $f \in \mathcal{S}(\mathbb{R}^2)$ whose Fourier transform satisfies $\operatorname{supp} \hat{f} \subseteq W_\Phi$.

Example. To illustrate the functions in the kernel of the limited angle Radon transform let us assume that we are given a function $f_1 \in \mathcal{S}(\mathbb{R}^2)$ such that $\operatorname{supp} \hat{f}_1 \subseteq \mathbb{R}^2 \setminus W_\Phi$. By Corollary 3.7, this function lies in the kernel of $\mathcal{R}_\Phi$, i.e., $\mathcal{R}_\Phi f_1 \equiv 0$. Now consider a rotated version of f_1, namely $f_2(x) = f_1(\varrho_\varphi x)$, where ϱ_φ denotes the rotation matrix in $\mathbb{R}^2$ with respect to the angle $\varphi \in [0, 2\pi)$. Assume that φ is chosen in such a way that $\operatorname{supp} \hat{f}_2 \cap W_\Phi \neq \emptyset$, Then, $f_2 \notin \ker(\mathcal{R}_\Phi)$. As a consequence, we see that kernel functions of $\mathcal{R}_\Phi$ are directional and that the orientation determines whether the function belongs to the kernel of the limited angle Radon transform $\mathcal{R}_\Phi$ or not. These considerations also show up in the corresponding practical experiment that is presented in Figure 3.3. ⌟

In order to understand the appearance of practical reconstructions in Figure 3.1, let us now consider the reconstruction problem which is given by the equation $\mathcal{R}_\Phi f = y$. In practice, the reconstruction is often obtained by computing a least squares solution $\widetilde{f} \in \arg\min \|\mathcal{R}_\Phi f - y\|^2_{L^2(Z)}$ or by computing a best approximate solution $f^\dagger = \mathcal{R}_\Phi^\dagger y$, cf. Appendix C. In both cases the reconstruction satisfies the normal equation

$$\mathcal{R}_\Phi^* \mathcal{R}_\Phi f = \mathcal{R}_\Phi^* y.$$

To characterize the solutions of this normal equation, we reformulate the result of Theorem 3.6 in the following way

$$\mathcal{R}_\Phi^* \mathcal{R}_\Phi f = 4\pi \mathcal{I}^1 P_\Phi f, \tag{3.18}$$

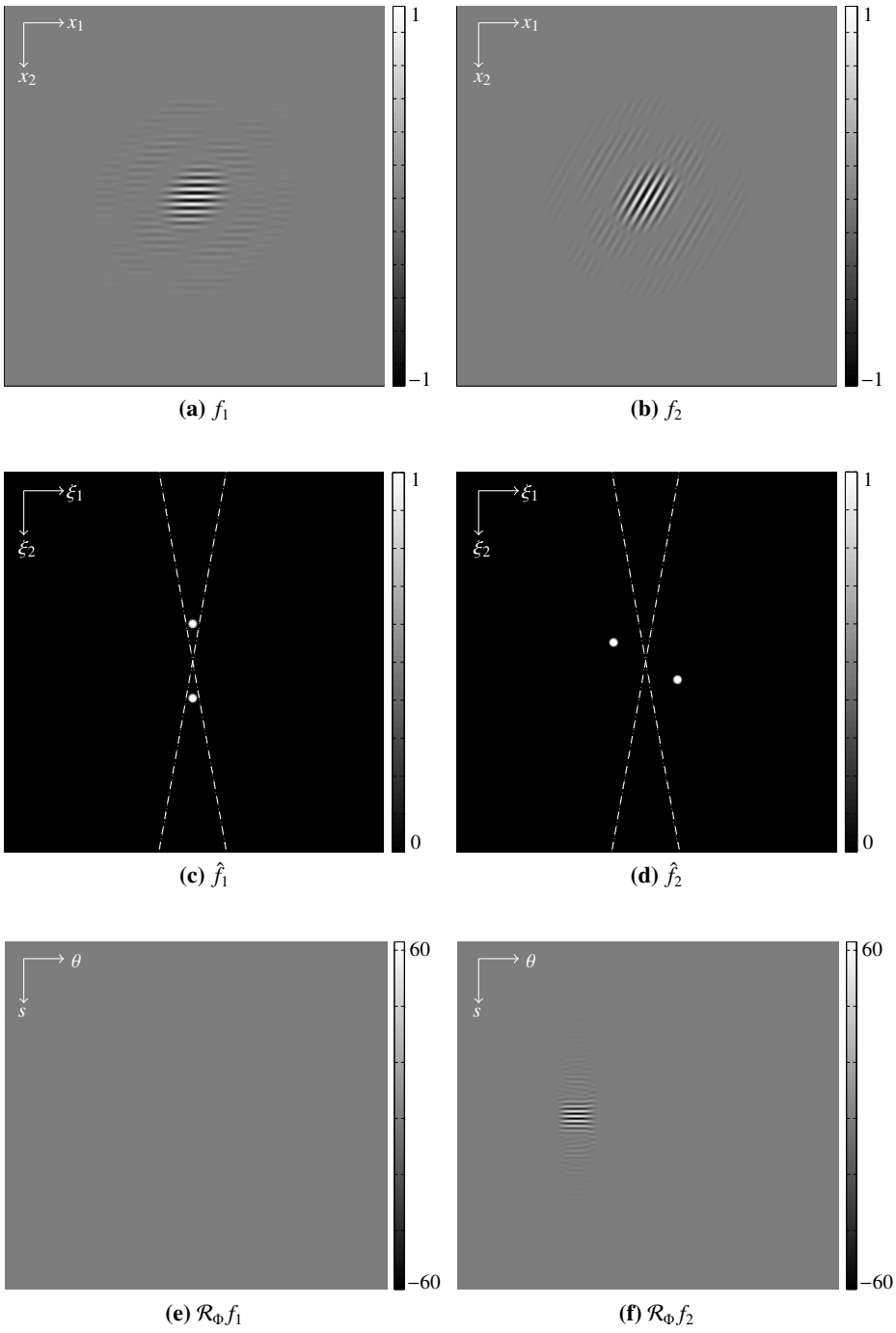

(a) f_1 **(b)** f_2

(c) $\hat{f}_1$ **(d)** $\hat{f}_2$

(e) $\mathcal{R}_\Phi f_1$ **(f)** $\mathcal{R}_\Phi f_2$

Figure 3.3: Illustration of the null space $\ker(\mathcal{R}_\Phi)$ for $\Phi = 80°$. The top row shows two functions $f_1(x_1, x_2)$ and $f_2(x_1, x_2)$ in the spatial domain, whose Fourier and Radon transforms are depicted in the middle and the bottom row, respectively. The dashed lines in the middle row indicate the boundary of the wedge W_Φ and, hence, do not belong to $\hat{f}_1(\xi_1, \xi_2)$, $\hat{f}_2(\xi_1, \xi_2)$. One can see that the function f_1 satisfies $\operatorname{supp} \hat{f}_1 \subseteq \mathbb{R}^2 \setminus W_\Phi$, whereas f_2 is a rotation of f_1 such that $\operatorname{supp} \hat{f}_2 \subseteq W_\Phi$. According to Corollary 3.7, it holds that $f_1 \in \ker(\mathcal{R}_\Phi)$ but $f_2 \notin \ker(\mathcal{R}_\Phi)$ which is also reflected by the images of the corresponding limited angle Radon transforms, $\mathcal{R}_\Phi f_1(\theta, s)$ and $\mathcal{R}_\Phi f_2(\theta, s)$, that are shown in the bottom row. As can be observed from the top row, both functions f_1 and f_2 are directional and their orientation determines whether they belong to the kernel of $\mathcal{R}_\Phi$ or not.

where I^1 denotes the Riesz potential (cf. (2.14)) and P_Φ is the projection operator defined by $P_\Phi f = \mathcal{F}^{-1}(\chi_{W_\Phi}\hat{f})$. Inserting this into the normal equation and applying $\mathcal{I}^{-1}$ to both sides yields

$$P_\Phi f = \frac{1}{4\pi}\mathcal{I}^{-1}\mathcal{R}_\Phi^* y.$$

Assuming that we are given perfect data, i.e., $y = \mathcal{R}_\Phi f$, we get

$$P_\Phi f = \frac{1}{4\pi}\mathcal{I}^{-1}\mathcal{R}_\Phi^*\mathcal{R}_\Phi f = \frac{1}{4\pi}\mathcal{I}^{-1}\mathcal{R}_\Phi^*\mathcal{R}_\Phi(P_\Phi f).$$

Thus, the set of all least squares solutions is given by

$$\mathbb{L}_\Phi = \left\{P_\Theta f : \ f \in \mathcal{S}(\mathbb{R}^2),\ \Phi \le \Theta \le \pi/2\right\}. \tag{3.19}$$

Since the best approximate solution $f^\dagger$ is a least squares solution of minimal L^2-norm, it is not hard to see that $f^\dagger = P_\Phi f = \frac{1}{4\pi}\mathcal{I}^{-1}\mathcal{R}_\Phi^*\mathcal{R}_\Phi f$. We summarize the above discussion in the following theorem.

Theorem 3.8. *Let $0 \le \Phi \le \pi/2$, $f_0 \in \mathcal{S}(\mathbb{R}^2)$ and $y = \mathcal{R}_\Phi f_0$. Then, the set of all least squares solutions of the equation $\mathcal{R}_\Phi f = y$ is given by* (3.19)*. In particular, the approximate inverse is given by*

$$f^\dagger = P_\Phi f = \frac{1}{4\pi}\mathcal{I}^{-1}\mathcal{R}_\Phi^*\mathcal{R}_\Phi f. \tag{3.20}$$

⌟

Note that the approximate inverse $f^\dagger$ in (3.20) is obtained by applying the inversion formula for the full angular (2.16) (with $\alpha = 1$) to the limited angle data $y = \mathcal{R}_\Phi f$. More generally, we get that the approximate inverse $f^\dagger$ may be computed by applying each of the inversion formulae in (2.16) to the limited angle Radon transform.

Theorem 3.9. *Let $f \in \mathcal{S}(\mathbb{R}^2)$ and $\alpha < 2$. Then,*

$$P_\Phi f = \frac{1}{4\pi}\mathcal{I}^{-\alpha}\mathcal{R}_\Phi^*\mathcal{I}^{\alpha-1}\mathcal{R}_\Phi f, \tag{3.21}$$

where $P_\Phi f = \mathcal{F}^{-1}(\chi_{W_\Phi}\hat{f})$. ⌟

Proof. The proof follows from the Fourier slice theorem (Theorem 2.3) by a simple computation:

$$\begin{aligned}
\frac{1}{4\pi}\mathcal{R}_\Phi^*\mathcal{I}^{\alpha-1}\mathcal{R}_\Phi f(x) &= \frac{1}{4\pi}\int_{S^1}\chi_{S^1_\Phi}(\theta)\mathcal{I}^{\alpha-1}\mathcal{R}_\Phi f(\theta, x\cdot\theta)\,\mathrm{d}\theta \\
&= \frac{1}{4\pi}\int_{S^1}\chi_{S^1_\Phi}(\theta)\int_{-\infty}^{\infty}|r\theta|^{-\alpha+1}\,\widehat{\mathcal{R}_\theta f}(r)e^{irx\cdot\theta}\,\mathrm{d}r\,\mathrm{d}\theta \\
&= \frac{1}{2\pi}\int_{S^1}\int_0^{\infty}\chi_{W_\Phi}(r\theta)\,|r|^{-\alpha}\,\hat{f}(r\theta)e^{irx\cdot\theta}r\,\mathrm{d}r\,\mathrm{d}\theta \\
&= \frac{1}{2\pi}\int_{\mathbb{R}^2}|\xi|^{-\alpha}\,(\chi_{W_\Phi}(\xi)\hat{f}(\xi))e^{ix\cdot\xi}\,\mathrm{d}\xi \\
&= (\mathcal{I}^\alpha P_\Phi f)(x).
\end{aligned}$$

The application of the Riesz potential $\mathcal{I}^{-\alpha}$ (cf. (2.14)) to both sides yields the assertion. ∎

Theorem 3.9 also shows that the naive application of the inversion formulas (2.16) to $y = \mathcal{R}_\Phi f$ reconstructs $P_\Phi f$ rather than the unknown function f. Since $f = P_\Phi f + (\mathrm{id} - P_\Phi) f$, that part of f that cannot be recovered from limited angle data is given by $(\mathrm{id} - P_\Phi) f$. In particular, only those functions can be perfectly recovered from limited angle data, whose Fourier transform is supported inside the wedge W_Φ.

In Section 2.4 we have outlined that the filtered backprojection algorithm may be regarded as an implementation of the inversion formula (2.18). Theorem 3.9 justifies the application of the filtered backprojection (FBP) algorithm in limited angle tomography only if the Fourier transform of the unknown function is supported inside the wedge W_Φ. In this case, the unknown function can be perfectly recovered from the limited angle data. However, if $\operatorname{supp} \hat{f} \not\subset W_\Phi$, then Theorem 3.9 implies that the FBP reconstruction is equal to $P_\Phi f$ which is equal to the approximate inverse at a limited angular range. This explains why the objects cannot be perfectly reconstructed from a limited angular range, cf. Figure 3.1.

Remark. Throughout this section we have assumed that the available angular range is given by $[-\Phi, \Phi]$. In this case, the corresponding polar wedge W_Φ is oriented along the the x-axis, cf. Figure 3.2. However, the results of this section can be easily adapted for arbitrary orientations of W_Φ and thus for arbitrary angular ranges. ⌟

3.3 Microlocal characterization of limited angle reconstructions

In the previous section we have shown that, at a limited angular range $[-\Phi, \Phi]$, the approximate inverse as well as the filtered backprojection reconstruction are given by $P_\Phi f = \mathcal{F}^{-1}(\chi_{W_\Phi} \hat{f})$. This implies that, in general, the unknown function cannot be recovered perfectly and also explains to some extent the discrepancy between the original and the reconstructed image in Figure 3.1.

The goal of this section is to give a more detailed characterization of features that can be reconstructed from limited angle Radon transform data. To this end, we shall use the concept of singularities as a mathematical tool for describing those features. The characterization will be presented within the mathematical framework of microlocal analysis that enables us to describe locations and directions of singularities (features) simultaneously.

3.3.1 Basic facts from microlocal analysis

In this subsection, we summarize some of the basic principles of microlocal analysis, where we mainly follow the expositions [Hör03], [Fri98]. To fix the notation, we recall that $\mathcal{D}(\mathbb{R}^2) = \{\varphi \in C^\infty(\mathbb{R}^2) : \operatorname{supp} \varphi \text{ is compact}\}$ and $\mathcal{E}(\mathbb{R}) = C^\infty(\mathbb{R}^2)$. The corresponding sets of distributions will be denoted by $\mathcal{D}'(\mathbb{R}^2)$ and $\mathcal{E}'(\mathbb{R}^2)$ (distributions with compact support), respectively. Throughout this chapter we will denote the action of distributions f on test functions φ by $\langle f, \varphi \rangle$, and use the notation $\mathbb{R}^n_* = \mathbb{R} \setminus \{0\}$ for $n = 1, 2$.

We start by giving the basic definitions.

Definition 3.10 (conic neighborhood). *A* conic neighborhood *of a set $A \subseteq \mathbb{R}^2_*$ is an open subset $\mathcal{N} \subseteq \mathbb{R}^2_*$ with $A \subseteq \mathcal{N}$ and the property that $t\xi \in \mathcal{N}$ for all $t > 0$ whenever $\xi \in \mathcal{N}$.* ⌟

Definition 3.11. *A function f is said to* decay rapidly in *a conic neighborhood $\mathcal{N}$ if for all $\xi \in \mathcal{N}$ and all $N \in \mathbb{N}$ it holds that $f(\xi) = O(|\xi|^{-N})$, $|\xi| \to \infty$, i.e.,*

$$\forall N \in \mathbb{N}\ \exists C_N > 0 :\ |f(\xi)| \leq C_N(1 + |\xi|)^{-N} \ \ as \ \ |\xi| \to \infty,\ \xi \in \mathcal{N}. \qquad \lrcorner$$

We now define the singular support of a distribution as the set of all singular locations.

Definition 3.12 (singular support). *The* singular support *of a distribution $f \in \mathcal{D}'(\mathbb{R}^2)$ is defined as the set*

$$\operatorname{sing\,supp}(f) = \left\{x \in \mathbb{R}^2 :\ \forall \varphi \in \mathcal{D}(\mathbb{R}^2), \varphi(x) \neq 0, \varphi f \notin \mathcal{D}(\mathbb{R}^2)\right\} \qquad \lrcorner$$

It follows directly form the definition that $\operatorname{sing\,supp}(f) \subseteq \operatorname{supp}(f)$, and $\operatorname{sing\,supp}(f) = \emptyset$ if and only if $f \in C^\infty(\mathbb{R}^2)$.

Definition 3.13 (frequency set). *Let $f \in \mathcal{E}'(\mathbb{R}^2)$. We define the* frequency set $\Sigma(f)$ of *f as the set of all directions $\xi \in \mathbb{R}^2_*$ in which $\hat{f}$ does not decay rapidly in any conic neighborhood of ξ. More precisely,*

$$\xi \notin \Sigma(f) \quad \Leftrightarrow \quad \exists \text{ conic neighborhood } \mathcal{N} \text{ of } \xi :\ \forall N \in \mathbb{N} :\ \hat{f}(\eta) = O(|\eta|^{-N}) \text{ in } \mathcal{N}. \tag{3.22}$$

$\lrcorner$

Remark. Since the frequency set $\Sigma(f)$ is conic, we will sometimes identify it with the quotient frequency set $\Sigma(f)/\!\sim$, where the equivalence relation $\sim$ is defined via

$$\xi \sim \eta \ :\Leftrightarrow\ \exists t \neq 0 :\ \eta = t\xi. \tag{3.23}$$

This identification is justified since for each real valued distribution $f \in \mathcal{E}'(\mathbb{R}^2)$ (that is $\langle f, \varphi\rangle \in \mathbb{R}$ for each real valued $\varphi \in C^\infty(\mathbb{R}^2)$), $\hat{f}$ does not decay rapidly in a conic neighborhood of ξ if and only if $\hat{f}$ does not decay rapidly a conic neighborhood of $-\xi$.

This identification justifies the nomenclature *directions* for the elements $\xi \in \Sigma(f)$. In this context, we will call the directions $\xi, \zeta \in \Sigma(f)$ different if the corresponding equivalence classes $[\xi]$ and $[\zeta]$ are disjoint. $\lrcorner$

We note a fundamental property of the frequency set.

Lemma 3.14 ([Hör03, Lemma 8.1.1]). *Let $f \in \mathcal{E}'(\mathbb{R}^2)$ and $\varphi \in \mathcal{D}(\mathbb{R}^2)$. Then,*

$$\Sigma(\varphi f) \subseteq \Sigma(f). \qquad \lrcorner$$

The singular support $\operatorname{sing\,supp}(f)$ of a distribution gives the location of the singularities, whereas, the frequency set $\Sigma(f)$ describes all directions in which f is singular. However, both concepts are not yet correlated. That is, if $\Sigma(f) \neq \emptyset$, then $f \notin C^\infty(\mathbb{R}^2)$, but we do not know the singular location corresponding to $\xi \in \Sigma(f)$.

The notion of the wavefront set combines both of these concepts and simultaneously describes the location and the direction of a singularity. In order to define the wavefront set, we first need the following notion of a localized frequency set.

Definition 3.15 (localized frequency set). *Let $f \in \mathcal{D}'(\mathbb{R}^2)$. The* localized frequency set *of f at $x \in \mathbb{R}^2$ is defined as*

$$\Sigma_x(f) = \bigcap \left\{ \Sigma(\varphi f) : \ \varphi \in \mathcal{D}(\mathbb{R}^2), \varphi(x) \neq 0 \right\}. \tag{3.24}$$

⌟

We first note that by Lemma 3.14 it holds $\Sigma_x(f) \subseteq \Sigma(f)$. Therefore, the localized frequency set $\Sigma_x(f)$ of f at x can be interpreted as the set of directions in which f is singular at x. This gives us a precise correspondence of singularities and its directions. We are now able to define the wavefront set.

Definition 3.16 (wavefront set). *Let $f \in \mathcal{D}'(\mathbb{R}^2)$. The* wavefront set *of f is given by*

$$\mathrm{WF}(f) = \left\{ (x, \xi) \in \mathbb{R}^2 \times \mathbb{R}^2_* : \ \xi \in \Sigma_x(f) \right\}. \tag{3.25}$$

If $(x, \xi) \notin \mathrm{WF}(f)$ one also says that f is microlocally near (x, ξ). ⌟

As a consequence of (3.25), the wavefront set $\mathrm{WF}(f)$ can be expressed as a union of sets of the form $\{x\} \times \Sigma_x(f)$. Since $\Sigma_x(f) = \emptyset$ if $x \notin \operatorname{sing\,supp}(f)$, we get the following expression

$$\mathrm{WF}(f) = \bigcup_{x \in \operatorname{sing\,supp}(f)} \{x\} \times \Sigma_x(f). \tag{3.26}$$

Remark. From Definition 3.16 it follows that $(x, \xi) \in \mathrm{WF}(f)$ if and only if for each cut off function $\varphi \in \mathcal{D}(\mathbb{R}^2)$ with $\varphi(x) \neq 0$ the Fourier transform $\widehat{\varphi f}$ does not decay rapidly in any open conic neighborhood of the ray $\{t\xi : \ t > 0\}$. In this context, one first localizes the distribution f near x by multiplying with φ and then microlocalizes $\widehat{\varphi f}$ near the direction ξ. ⌟

The following proposition shows that the wavefront set indeed contains the information of both, $\operatorname{sing\,supp}(f)$ and $\Sigma(f)$. An element $(x, \xi) \in \mathrm{WF}(f)$ gives the information about the location x of a singularity and its direction ξ.

Proposition 3.17 ([Hör03, Prop. 8.1.3]). *Let π_1 be the projection onto the first variable, $\pi_1(x, \xi) = x$, and π_2 be the projection onto the second variable, $\pi_2(x, \xi) = \xi$, respectively. Then, the following relations hold*

$$\pi_1\left(\mathrm{WF}(f)\right) = \operatorname{sing\,supp}(f), \tag{3.27}$$

$$\pi_2\left(\mathrm{WF}(f)\right) = \Sigma(f). \tag{3.28}$$

⌟

The next proposition gives an upper bound for the wavefront set.

Proposition 3.18. *For each $f \in \mathcal{E}'(\mathbb{R}^2)$ we have*

$$\mathrm{WF}(f) \subseteq \operatorname{sing\,supp} f \times \Sigma(f). \tag{3.29}$$

⌟

Proof. This is an immediate consequence of Lemma 3.14 and (3.26). ∎

Figure 3.4: The Shepp-Logan head phantom (left) with its singular support, indicated by the black solid line (right). The direction ξ of the singularity at x is given by the normal to the boundary, cf. (3.30).

We note a very important example that illustrates the concept of the wavefront set and which will be of importance for us later.

Example. Let $\Omega \subseteq \mathbb{R}^2$ be such that the boundary $\partial\Omega$ is a smooth manifold. Then, the wavefront set of χ_Ω is characterized by

$$(x, \xi) \in WF(\chi_\Omega) \quad \Leftrightarrow \quad x \in \partial\Omega,\ \xi \in N_x\ (\xi \text{ is a normal vector to } \partial\Omega \text{ at } x), \tag{3.30}$$

where χ_Ω denotes the characteristic function of Ω and N_x is the normal space to $\partial\Omega$ at $x \in \partial\Omega$. The proof of this fact is non-trivial and we refer the reader to [Hör03, p. 265]. ⌟

The relationship (3.30) provides an intuitive understanding of the wavefront set of a function. It motivates to think of a singularity $(x, \xi) \in \mathrm{WF}(f)$ in terms of an oriented infinitesimally small line segment which is located at x and has the normal direction ξ. This way of thinking gives us an idea how to visualize the wavefront set of a given function and, on the other hand, to visualize the singularities of an unknown function if only the wavefront set $\mathrm{WF}(f)$ is known.

We conclude visualizing the wavefront set of the well-known Shepp-Logan head phantom in Figure 3.4. By (3.30) and discussion above, it is easy to see that the singularities are located along the boundaries of the elliptic regions, whereas the singular directions are given by the normal directions (except at intersections), cf. the Figure 3.4.

3.3.2 Microlocal characterizations of limited angle reconstructions

Recall that the approximate inverse solution as well as the filtered backprojection reconstruction at the limited angular range $[-\Phi, \Phi]$ is given by $P_\Phi f = \mathcal{F}^{-1}(\chi_{W_\Phi} \cdot \hat{f})$, cf. Section 3.2. In the following theorem we note a simple observation about the wavefront set of $P_\Phi f$.

Theorem 3.19. *For $f \in L^2(\mathbb{R}^2)$ we have*

$$\mathrm{WF}(P_\Phi f) \subseteq \operatorname{sing\,supp}(P_\Phi f) \times W_\Phi. \tag{3.31}$$

⌟

Proof. Since $\Sigma(P_\Phi f) \subseteq W_\Phi$, the assertion follows from Proposition 3.18. ∎

As a consequence of Theorem 3.19, we conclude that $P_\Phi f$ has no singularities in directions $\xi \in W_\Phi^C := \mathbb{R}^2 \setminus W_\Phi$. Therefore, the reconstruction $P_\Phi f$ is smooth in directions $\xi \in W_\Phi^C$ at every point $x \in \mathbb{R}^2$. This observation explains the appearance of limited angle FBP reconstructions in Figure 3.1, where we can clearly observe the directional smoothing.

In order to get a characterization which is independent of the reconstruction method, we need to relate the singularities of the Radon transform $\mathcal{R}_\Phi f$ to the singularities of f. A correspondence between the wavefront set $\mathrm{WF}(\mathcal{R}f)$ and $\mathrm{WF}(f)$ was established by E.T. Quinto. We cite this in the following theorem.

Theorem 3.20 ([Qui93]). *Let $f \in \mathcal{E}'(\mathbb{R}^2)$, $a \neq 0$, and $x \in L(\theta, s) = \{x \in \mathbb{R}^2 : x \cdot \theta = s\}$ with $(\theta, s) \in Z = S^1 \times \mathbb{R}$. Moreover, we denote $\zeta = (-x \cdot \theta^\perp, 1)^\top$. Then,*

$$((\theta, s), a\zeta) \in \mathrm{WF}(\mathcal{R}f) \quad \Leftrightarrow \quad (x, a\theta) \in \mathrm{WF}(f). \tag{3.32}$$

⌟

We use Theorem 3.20 to investigate the relationship between the wavefront set of the limited angle Radon transform, $\mathrm{WF}(\mathcal{R}_\Phi f)$, and the sought function f. Apparently, we have the same correspondence as in (3.32) if (θ, s) lies in the interior of $Z_\Phi = S^1_\Phi \times \mathbb{R}$, which in turn is the case when θ belongs to the interior of S^1_Φ. On the other hand, since there is no data point for $(\theta, s) \notin Z_\Phi$, the wavefront set $\mathrm{WF}(\mathcal{R}_\Phi f)$ contains no element $((\theta, s), a\zeta)$ for $\theta \notin S^1_\Phi$. Consequently, the limited angle data $y = \mathcal{R}_\Phi f$ does not carry enough information about the singularities $(x, \xi) \in \mathrm{WF}(f)$, where $\xi \notin W_\Phi$. As a result, we cannot stably recover these singularities. This is in accordance with Theorem 3.19 and the subsequent discussion.

Example. Let $f(x) = \chi_\Omega$ be the characteristic function of the unit ball $\Omega \subseteq \mathbb{R}^2$. Then,

$$\mathcal{R}f(\theta, s) = \begin{cases} 2(1 - s^2)^{1/2} & \text{for } |s| \leq 1, \\ 0 & \text{otherwise.} \end{cases}$$

The Radon transform $\mathcal{R}f(\theta, s)$ is therefore smooth on $S^1 \times (-1, 1)$, whereas $\mathcal{R}f(\theta, s)$ is singular at each point $(\theta, \pm 1)$, $\theta \in S^1$, cf. Figure 3.5. That is, singularities appear exactly for those $(\theta, s) \in Z$, for which the line $L(\theta, s)$ is tangent to the boundary of the unit ball Ω. ⌟

The above discussion motivates the following definition, which was originally given in [Qui06].

Definition 3.21 (visible singularity). *A singularity $(x, \theta) \in \mathrm{WF}(f)$, $\theta \in S^1$, is called* visible *from a limited data set if the value $\mathcal{R}_\Phi f(\theta, x \cdot \theta)$ is in the data set. Other singularities are called* invisible. ⌟

The characterization of visible singularities at a given angular range is of great importance for practical applications since it describes precisely the information content of an incomplete tomographic data set. Thus, visible singularities provide information about features that can be

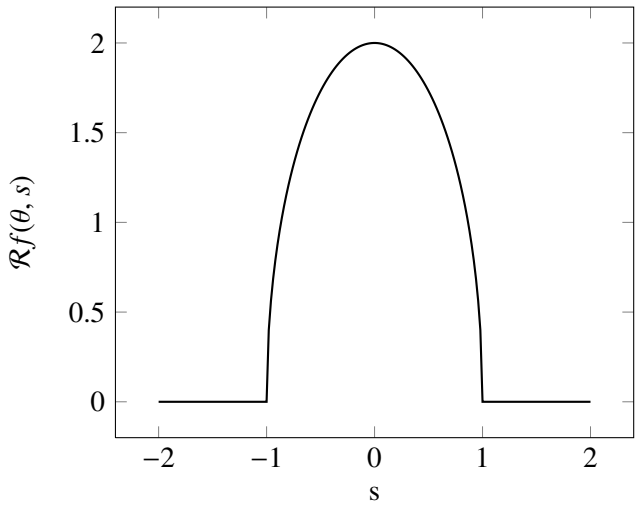

Figure 3.5: Radon transform of the characteristic function of the unit disc. For $s \neq 1$, $\mathcal{R}f(\theta, s)$ is smooth. Exactly at lines tangent to the boundary of f, $L(\theta, \pm 1)$, $\mathcal{R}f(\theta, s)$ is not smooth (the first derivative is infinite).

reconstructed at a limited angular range and, in particular, about those features which cannot be reconstructed from the given data (cf. discussion at the end of Subsection 3.3.1).

Let us draw some conclusions for the case of the limited angular range $[-\Phi, \Phi]$. In this case, the visible singularities (x, ξ) of an unknown function f are exactly those with $\xi \in W_\Phi$, cf. Theorem 3.20. We therefore know a-priori that any reconstruction f_{rec} from the limited angle data $y = \mathcal{R}_\Phi f$ will satisfy

$$\text{WF}(f_{\text{rec}}) \subseteq \mathbb{R}^2 \times W_\Phi. \tag{3.33}$$

This observation is also reflected by practical reconstructions which are shown in Figure 3.6. Since the above relation (3.33) does not depend on a particular reconstruction algorithm, the inclusion (3.33) may be interpreted as an *inherent a-priori information of limited angle tomography*.

Remark. A result similar to Theorem 3.20 is also available for the three-dimensional case, which is formulated with respect to the divergent x-ray transform $\mathcal{D}$ (cf. Theorem 2.11) in $\mathbb{R}^3$ with sources on a smooth curve γ in $\mathbb{R}^3$, cf. [Qui93]: Let f be a distribution with compact support, $x \in \text{supp}(f)$. Then any singularity $(x, \xi) \in \text{WF}(f)$ is stably detected from data $\mathcal{D}f$ if and only if

$$\text{the plane } \mathcal{P}(x, \xi) \text{ through } x \text{ with normal direction } \xi, \text{ intersects } \gamma \text{ transversally}^1. \tag{3.34}$$

If data are taken over an open set of rays with sources on γ, then a ray in $\mathcal{P}(x, \xi)$ from γ to x must be in the data set for (3.34) to apply.

Note that condition (3.34) is necessary for every tomographic reconstruction method in three dimensions which deals with x-ray data $\mathcal{D}f$. Indeed, the requirement that "each plane which

[1] Two submanifolds of a given finite dimensional smooth manifold are said to intersect transversally if at every point of intersection, their separate tangent spaces at that point together generate the tangent space of the ambient manifold at that point.

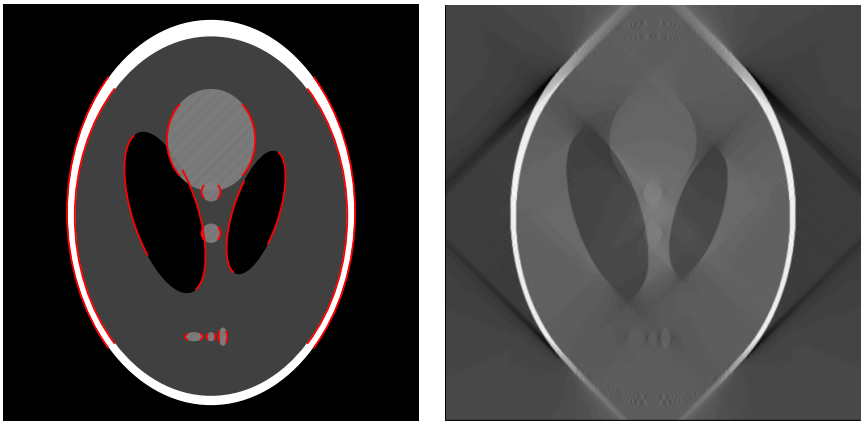

Figure 3.6: The Shepp-Logan head phantom (left) and its reconstruction at the angular range $[-45°, 45°]$ (right). The red lines in the left image indicate visible singularities at the given angular range. In the reconstructed image on the right, the visible singularities are clearly visible, however, the invisible singularities are smoothed out. In addition to the visible singularities, the reconstruction (right) shows the appearance of some streak artifacts.

meets supp f intersects the curve transversally" is part of the Tuy's condition (2.21) in Theorem 2.11, which is the standard inversion formula for the x-ray transform in $\mathbb{R}^3$. In turn, Tuy's condition ensures that all singularities of the imaged object f are visible. ⌟

3.4 Characterization and reduction of limited angle artifacts

In the previous section we have shown that only visible singularities of a function can be reconstructed from a limited angular range, whereas the invisible singularities are smoothed or distorted. However, the practical reconstructions in Figure 3.6 reveal another phenomenon. Besides the visible singularities, the reconstruction shows the appearance of some additional singularities that seem to be located on straight lines. Motivated by this observation, the goal of this section is to present an exact characterization of these additional singularities. To this end, we will derive another microlocal characterization of $P_\Phi f$ (which is considered as limited angle reconstruction, cf. Section 3.2). Based on this characterization, we will present a novel strategy for artifact reduction. In addition, we will show that this strategy can be easily integrated into the filtered backprojection algorithm.

3.4.1 Characterization of limited angle artifacts

To gain knowledge about the limited angle artifacts we again consider $P_\Phi f = \mathcal{F}^{-1}(\chi_{W_\Phi} \hat{f})$, cf. Theorem 3.9. Our goal is derive a more precise characterization of the wavefront set $\mathrm{WF}(P_\Phi f)$. To this end, we need some more facts about the wavefront sets.

Theorem 3.22 ([Hör03, p. 270]). *Let $f \in \mathcal{D}'(\mathbb{R}^2)$ and $g \in \mathcal{E}'(\mathbb{R}^2)$. Then,*

$$\mathrm{WF}(f * g) \subseteq \left\{(x+y,\xi) \in \mathbb{R}^2 \times \mathbb{R}^2_* : (x,\xi) \in \mathrm{WF}(f),\ (y,\xi) \in \mathrm{WF}(g)\right\}. \qquad \lrcorner$$

In what follows, we call a distribution $f \in \mathcal{S}'(\mathbb{R}^2)$ *homogeneous* if f is homogeneous of some degree $\alpha \in \mathbb{R}$, cf. Proposition A.17. The next lemma shows that the wavefront set $\mathrm{WF}(f)$ of a homogeneous distributions $f \in \mathcal{S}'(\mathbb{R}^2)$ is determined by the wavefront set of its Fourier transform.

Lemma 3.23 ([Hör03, Theorem 8.1.8]). *Let $f \in \mathcal{S}'(\mathbb{R}^2)$ be homogeneous in $\mathbb{R}^2_*$, then*

$$(x,\xi) \in \mathrm{WF}(f) \ \Leftrightarrow\ (\xi,-x) \in \mathrm{WF}(\hat{f}\,),$$

whenever $\xi \neq 0$ and $x \neq 0$. $\lrcorner$

We are now able to prove our main result of this section.

Theorem 3.24. *Let $0 \leq \Phi \leq \pi/2$ and let $f \in L^2(\mathbb{R}^2)$ have compact support. Denote $\mathrm{int}(W_\Phi)$ the interior of the polar wedge W_Φ and let $\xi_\varphi = (\cos(\varphi),\sin(\varphi))^\intercal$, $\xi_\varphi^\perp = (-\sin(\varphi),\cos(\varphi))^\intercal$ for $\varphi \in [-\pi,\pi)$. Then*

$$\mathrm{WF}(P_\Phi f) \subseteq \mathrm{WF}_\Phi(f) \cup \mathcal{A}_\Phi, \tag{3.35}$$

where

$$\mathrm{WF}_\Phi(f) = \left\{(x,\xi) \in \mathbb{R}^2 \times \mathbb{R}^2_* :\ (x,\xi) \in \mathrm{WF}(f),\ \xi \in \mathrm{int}(W_\Phi)\right\} \tag{3.36}$$

is the set of visible singularities of f and

$$\mathcal{A}_\Phi = \left\{(x + r\xi_\varphi^\perp, \alpha\xi_\varphi) :\ (x,\xi_\varphi) \in \mathrm{WF}(f),\ r,\alpha \in \mathbb{R}_*,\ \varphi = \pm\Phi\right\} \tag{3.37}$$

is the set of additional singularities. $\lrcorner$

Proof. In what follows we let $u_\Phi(x) = \chi_{W_\Phi}(x)$ and $\check{u}_\Phi = \mathcal{F}^{-1}(u_\Phi)$. Then $u_\Phi, \check{u}_\Phi \in \mathcal{S}'(\mathbb{R}^2)$ and

$$P_\Phi f = \frac{1}{2\pi} f * \check{u}_\Phi.$$

Moreover, by Theorem 3.22, we have

$$\mathrm{WF}(P_\Phi f) \subseteq \left\{(x+y,\xi) \in \mathbb{R}^2 \times \mathbb{R}^2_* : (x,\xi) \in \mathrm{WF}(f),\ (y,\xi) \in \mathrm{WF}(\check{u}_\Phi)\right\}. \tag{3.38}$$

Thus, we need to compute $\mathrm{WF}(\check{u}_\Phi)$. Now observe that $\check{u}_\Phi$ is homogeneous (since u_Φ is homogeneous), cf. Proposition A.17. Therefore, by Lemma 3.23, it suffices to compute the wavefront set $\mathrm{WF}(u_\Phi)$. To this end, we first note that

$$\mathrm{sing\,supp}\,(u_\Phi) = \partial W_\Phi = (\mathbb{R}\cdot\xi_\Phi) \cup (\mathbb{R}\cdot\xi_{-\Phi}).$$

In order to compute the localized frequency sets $\Sigma_x(u_\Phi)$ for each $x \in \mathrm{sing\,supp}(u_\Phi)$, we note that the singular directions at each $x_\pm \in \mathbb{R}\cdot\xi_{\pm\Phi}\setminus\{0\}$ are given by the normals to $\xi_{\pm\Phi}$, cf. correspondence (3.30). Hence, we have

$$\Sigma_{x_\pm}(u_\Phi) = \mathbb{R}_* \cdot \xi_{\pm\Phi}^\perp,$$

and thus

$$\mathrm{WF}(u_\Phi) = \left\{(r\xi_\varphi, \alpha\xi_\varphi^\perp)^\intercal : \ r, \alpha \in \mathbb{R}_*, \ \varphi = \pm\Phi\right\} \cup \{0\} \times \Sigma_0(u_\Phi).$$

By Lemma 3.23, we therefore have

$$\begin{aligned}\mathrm{WF}(\check{u}_\Phi) &= \left\{(r\xi_\varphi^\perp, \alpha\xi_\varphi) : \ r, \alpha \in \mathbb{R}_*, \ \varphi = \pm\Phi\right\} \cup \{0\} \times \Sigma_0(\check{u}_\Phi) \\ &\subseteq \left\{(r\xi_\varphi^\perp, \alpha\xi_\varphi) : \ r, \alpha \in \mathbb{R}_*, \ \varphi = \pm\Phi\right\} \cup \{0\} \times W_\Phi, \end{aligned} \tag{3.39}$$

where the last inclusion is due to $\Sigma_0(\check{u}_\Phi) \subseteq W_\Phi$, which in turn follows from $\operatorname{supp} \mathcal{F}(\check{u}_\Phi) \subseteq W_\Phi$ by Proposition 3.18. The assertion follows now by inserting (3.39) into (3.38). ∎

Theorem 3.24 is of particular interest for limited angle tomography since it provides a precise characterization of the wavefront set of the filtered backprojection reconstruction at the angular range $[-\Phi, \Phi]$. In particular, it explains all effects that can be observed in practical reconstructions in Figure 3.1: On the one hand, there is the effect of cancellation or smoothing of singularities of f that is expressed by the fact that $\mathrm{WF}(P_\Phi f) \subseteq \mathrm{WF}_\Phi(f) \cup \mathcal{A}_\Phi \subseteq \mathbb{R}^2 \times W_\Phi$. Therefore, only the visible singularities are reconstructed, other singularities are smoothed. On the other hand, Theorem 3.24 characterizes the limited angle artifacts that can be observed in every filtered backprojection reconstruction, cf. Figures 3.1. These artifacts, are described by those singularities $(x, \xi) \in \mathrm{WF}(P_\Phi f)$ that belong to the set $\mathcal{A}_\Phi$, cf. (3.37). We call these singularities *additional* since $(x, \xi) \in \mathcal{A}_\Phi$, in general, does not imply that $(x, \xi) \in \mathrm{WF}(f)$.

Let us take a closer look at the additional singularities $(x, \xi) \in \mathcal{A}_\Phi$. First of all, note that by (3.37) we have $\mathcal{A}_\Phi \neq \emptyset$ if and only if $\xi_{\pm\Phi} \in \Sigma(f)$. In this case, $(x_f, \alpha\xi_{\pm\Phi}) \in \mathrm{WF}(f)$ for some $x_f \in \operatorname{sing\,supp}(f)$. Now let $(x_f, \alpha_0\xi_{\pm\Phi}) \in \mathrm{WF}(f)$ for some $\alpha_0 \neq 0$. Then, by (3.37),

$$(x_f + r\xi_{\pm\Phi}^\perp, \alpha\xi_{\pm\Phi}) \in \mathcal{A}_\Phi$$

for each $r, \alpha \in \mathbb{R}_*$. That is, only the existence of a singularity $(x_f, \alpha_0\xi_{\pm\Phi}) \in \mathrm{WF}(f)$ induces new singularities that have the same direction and are located on the line $l(r) = x_f + r\xi_{\pm\Phi}^\perp$. This fact describes exactly the streak artifacts that are visible in reconstructions in Figures 3.1. An illustration of the above discussion is shown in Figure 3.7.

We conclude this section by noting that a good reconstruction algorithm should be, on the one hand, able to reliably reconstruct visible singularities and, on the other hand, should avoid the production of the added singularities.

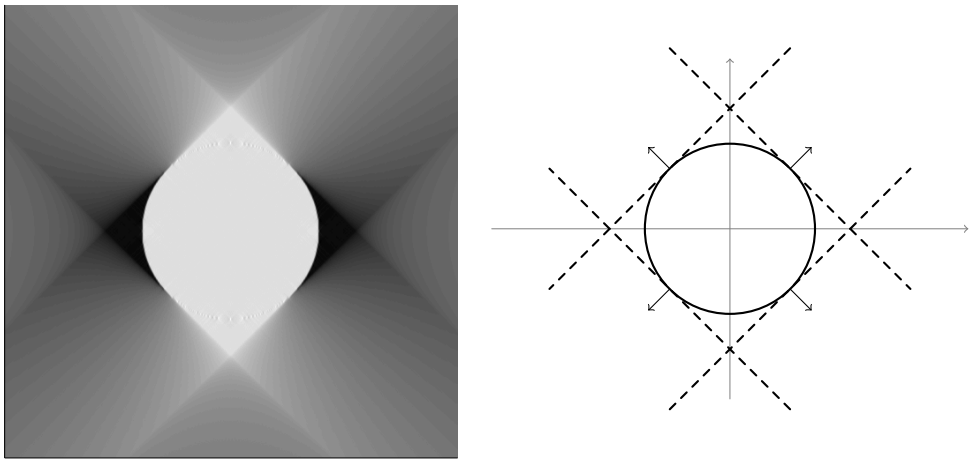

Figure 3.7: Filtered backprojection reconstruction (left) of χ_Ω at an angular range $[-\Phi, \Phi]$, $\Phi = 45°$ and an illustration of additional singularities (right). According to Theorem 3.24, the additional singularities (streak artifacts) are located on lines $l(r) = x_f + r\xi_{\pm\Phi}$, where x_f is such that $(x_f, \alpha\xi_{\pm\Phi}) \in \mathrm{WF}(f)$ for $\alpha \neq 0$. The correspondence of the theoretical description (right) and practical reconstruction (left) is remarkable.

3.4.2 Reduction of limited angle artifacts

Our aim in this subsection is to derive an artifact reduction strategy for the filtered backprojection (FBP) algorithm in limited angle tomography. To this end, let us recall that the basis of the limited angle FBP is the inversion formula (3.21)

$$P_\Phi f = \frac{1}{4\pi}\mathcal{R}_\Phi^* \mathcal{I}^{-1}\mathcal{R}_\Phi f. \tag{3.40}$$

In order to reduce artifacts, our idea consists in modifying the above inversion formula in such a way that it outputs a function $T_\Phi f$ which

(i) does not include additional singularities, i.e., $\mathrm{WF}(T_\Phi f) \subseteq \mathrm{WF}_\Phi(f)$,

(ii) is a good approximation to $P_\Phi f$.

Let us first point out the reason why $P_\Phi f = \mathcal{F}^{-1}(\chi_{W_\Phi} \cdot \hat{f})$ may contain singularities (x, ξ) which do not belong to the wavefront set of f. To this end, we write

$$P_\Phi f = \frac{1}{2\pi} f * \check{u}_\Phi,$$

where $\check{u}_\Phi = \mathcal{F}^{-1}(\chi_{W_\Phi})$. Then, by examining the proof of Theorem 3.24 it is easy to see that the set of additional singularities $\mathcal{A}_\Phi$ may be written as

$$\mathcal{A}_\Phi = \left\{(x + y, \xi) \in \mathbb{R}^2 \times \mathbb{R}^2_* : (x, \xi) \in \mathrm{WF}(f),\ (y, \xi) \in \mathrm{WF}(\check{u}_\Phi),\ y \neq 0\right\}.$$

Consequently, the additional singularities appear only if there are singularities $y \in \mathrm{sing\,supp}(\check{u}_\Phi)$ with $y \neq 0$. In order to avoid the production of additional singularities it is therefore canonical to aim at reconstructing

$$T_\Phi f = \frac{1}{2\pi} f * \check{\kappa}_\Phi \tag{3.41}$$

instead of $P_\Phi f$, where $\check{\kappa}_\Phi \in \mathcal{S}'(\mathbb{R}^2)$ is assumed to be homogeneous sucht that sing supp$(\check{\kappa}_\Phi) = \{0\}$. This ensures the requirement (i) to hold. To summarize the above discussion we record the following lemma.

Lemma 3.25. *Let $\kappa_\Phi \in C^\infty(\mathbb{R}^2)$ be bounded and homogeneous of degree 0 such that*

$$\kappa_\Phi|_{W_{(\Phi-\varepsilon)}} \equiv 1, \quad \kappa_\Phi|_{\mathbb{R}^2\setminus W_\Phi} \equiv 0 \tag{3.42}$$

for some $0 < \varepsilon \leq \Phi$. Moreover, let

$$\check{\kappa}_\Phi := \mathcal{F}^{-1}(\kappa_\Phi).$$

Then, for $T_\Phi f$ defined in (3.41)*, we have*

$$\mathrm{WF}(T_\Phi f) \subseteq \mathrm{WF}_\Phi(f).$$

In particular, this relation ensures that no additional singularities are produced. ⌟

Proof. Note that $\check{\kappa}_\Phi = \mathcal{F}^{-1}(\kappa_\Phi)$ is homogeneous because κ_Φ is homogeneous, cf. Proposition A.17. Moreover, by Lemma 3.23, we have that sing supp $\check{\kappa}_\Phi \subseteq \{0\}$. The assertion follows now from Theorem 3.22 since $\Sigma(\check{\kappa}_\Phi) \subseteq W_\Phi$ (cf. Proposition 3.18). ∎

The next theorem shows that a simple modification of the inversion formula (3.40) leads to an artifact-free reconstruction $T_\Phi f$.

Theorem 3.26. *Let κ_Φ fulfill the assumptions of Lemma 3.25. In addition, assume that κ_Φ symmetric, i.e, $\kappa_\Phi(\theta) = \kappa_\Phi(-\theta)$ for all $\theta \in S^1$. Then,*

$$T_\Phi f = \frac{1}{4\pi}\mathcal{R}_\Phi^* \mathcal{I}^{-1}\mathcal{K}_\Phi \mathcal{R} f, \tag{3.43}$$

where $T_\Phi f$ is defined in (3.41)*, and*

$$\mathcal{K}_\Phi \mathcal{R} f(\theta, s) = \kappa_\Phi(\theta) \cdot \mathcal{R} f(\theta, s).$$

In particular, the inversion formula (3.43) *does not produce additional artifacts, i.e.,*

$$\mathrm{WF}(T_\Phi f) \subseteq \mathrm{WF}(f).$$ ⌟

Proof. First note that $\mathcal{I}^{-1}$ and $\mathcal{K}_\Phi$ commute since $\mathcal{I}^{-1}$ acts on the second variable of $\mathcal{R}_\Phi f$, whereas $\mathcal{K}_\Phi$ acts on the first variable of $\mathcal{R}_\Phi f$. Moreover, because κ_Φ is homogeneous of degree 0, we have $\kappa_\Phi(r\theta) = \kappa_\Phi(\theta)$ for all $\theta \in S^1$, $r \neq 0$. Following the proof of Theorem 3.9 for

$\alpha = 0$, we therefore get

$$\begin{aligned}
\frac{1}{4\pi}\mathcal{R}_\Phi^* \mathcal{I}^{-1}\mathcal{K}_\Phi \mathcal{R}_\Phi f(x) &= \frac{1}{4\pi}\int_{S^1} \chi_{S^1_\Phi}(\theta)\mathcal{K}_\Phi \mathcal{I}^{-1}\mathcal{R}_\Phi f(\theta, x\cdot\theta)\,\mathrm{d}\theta \\
&= \frac{1}{4\pi}\int_{S^1} \chi_{S^1_\Phi}(\theta)\int_{-\infty}^{\infty} \kappa_\Phi(\theta)\,|r|\,\widehat{\mathcal{R}_\theta f}(r) e^{irx\cdot\theta}\,\mathrm{d}r\,\mathrm{d}\theta \\
&= \frac{1}{2\pi}\int_{S^1}\int_0^{\infty} \kappa_\Phi(r\theta)\hat{f}(r\theta)e^{irx\cdot\theta} r\,\mathrm{d}r\,\mathrm{d}\theta \\
&= \frac{1}{2\pi}\int_{\mathbb{R}^2} \kappa_\Phi(\xi)\hat{f}(\xi)e^{ix\cdot\xi}\,\mathrm{d}\xi \\
&= \mathcal{F}^{-1}(\kappa_\Phi \cdot \hat{f})(x) \\
&= \frac{1}{2\pi}(f * \check{\kappa}_\Phi)(x) = T_\Phi f(x).
\end{aligned}$$

The last statement follows from Lemma 3.25. ∎

The above Theorem 3.26 shows that a simple preprocessing of the data $y_\Phi = \mathcal{R}_\Phi f$, namely the multiplication of the data y_Φ by the function κ_Φ, i.e.,

$$\overline{y}_\Phi(\theta, s) = \kappa_\Phi(\theta)\cdot y_\Phi(\theta, s), \tag{3.44}$$

and the subsequent application of the limited angle FBP leads to a reconstruction that does not contain additional singularities. We note that the authors of [KLQ12] applied a similar smooth data truncation in the case of the elliptical Radon transform in order to reduce limited angle artifacts.

Remark. Let us give a different view on the artifact reduction strategy. To this end, we interpret the limited angle Radon transform data $y_\Phi = \mathcal{R}_\Phi f$ as a truncated version of $y = \mathcal{R}f$ via

$$y_\Phi(\theta, s) = \chi_{S^1_\Phi}(\theta)\cdot y(\theta, s),$$

where $(\theta, s) \in S^1 \times \mathbb{R}$. Assuming that $y(\pm\Phi, s) \neq 0$ for some $s \in \mathbb{R}$, this hard truncation in the Radon domain introduces additional singularities in the data y_Φ which are located at $(\pm\Phi, s)$ for each $s \in \mathbb{R}$. These additional singularities in the Radon domain entail added singularities in the reconstruction. In order to avoid the additional singularities in the Radon domain, it is therefore reasonable to use a smoothly truncated data $\overline{y}_\Phi(\theta, s) = \kappa_\Phi(\theta)y(\theta, s)$. In that regard, only those singularities are reconstructed which belong to the original object f. In particular, no added singularities are generated.

Though it is not a formal proof, the above discussion gives an intuitive understanding of the artifact reduction strategy that we presented in Theorem 3.26. ⌟

Example. Let $\varphi_\varepsilon : [-\pi, \pi] \to [0, 1]$ be defined by $\varphi_\varepsilon(x) = \exp(\frac{x^2}{x^2-\varepsilon^2})$ for $|x| \leq \varepsilon$ and $\varphi_\varepsilon(x) = 0$

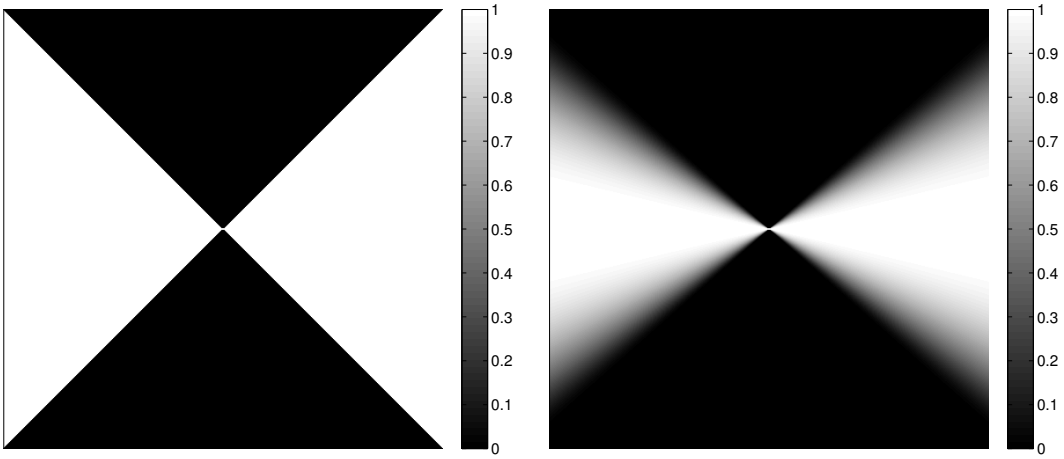

Figure 3.8: The characteristic function χ_{W_Φ} (left) and the smooth truncation function κ_Φ (right) as defined in (3.45) for $\Phi = 45°$ and $\varepsilon = 35°$.

for $|x| > \varepsilon$. Denote $\xi_\theta = (\cos\theta, \sin\theta)$ for $\theta \in [-\pi, \pi]$. Then, the function

$$\kappa_\Phi(r\xi_\theta) = \begin{cases} \varphi_\varepsilon(\theta + (\Phi - \varepsilon)), & \theta \in [-\Phi, -(\Phi - \varepsilon)], \\ 1, & \theta \in [-(\Phi - \varepsilon), \Phi - \varepsilon], \\ \varphi_\varepsilon(\theta - (\Phi - \varepsilon)), & \theta \in [(\Phi - \varepsilon), \Phi], \\ 0, & \text{otherwise.} \end{cases} \tag{3.45}$$

satisfies the assumptions of Lemma 3.25 and Theorem 3.26, and therefore can be used for artifact reduction according to (3.43). A plot of such κ_Φ is given in Figure 3.8. ⌟

We have implemented this artifact reduction strategy in Matlab using the function κ_Φ as defined in (3.45). The resulting reconstructions for $\Phi = 45°$ and $\varepsilon = 35°$ are shown in Figure 3.9. Here, one can clearly observe the effect of artifact reduction: While the limited angle artifacts are visible in the FBP reconstructions (middle column), the implementation of the artifact reduction strategy (3.41) avoids the production of the additional singularities (right column).

Finally, let us comment on the choice of the parameter $\varepsilon \in (0, \Phi]$ in (3.42) (cf. also (3.45)). First note that, according to Lemma 3.25 and Theorem 3.26, every choice of the parameter $\varepsilon \in (0, \Phi]$ leads to a reconstruction $T_\Phi f$ which does not contain additional artifacts as opposed to $P_\Phi f$. Secondly, the function $\kappa_{\Phi,\varepsilon} = \kappa_\Phi$ converges pointwise to χ_{W_Φ} as $\varepsilon \to 0$ (according to (3.42)). Therefore, a small value of the parameter ε ensures that $T_\Phi f$ is close to $P_\Phi f$ (cf. requirement (ii)). That is, a small parameter ε leads to a reconstruction $T_\Phi f$ which is a good approximation to $P_\Phi f$ and which does not contain additional artifacts. However, in practice, small values of ε lead to artifacts in the reconstruction as can be observed in Figure 3.10. This is because κ_Φ decays very fast near the boundary ∂W_Φ for small values of ε. Therefore, the parameter ε has to be chosen appropriately. For the experiment in Figure 3.9, the choice of this parameter was based on a visual inspection of reconstructions for different values of ε.

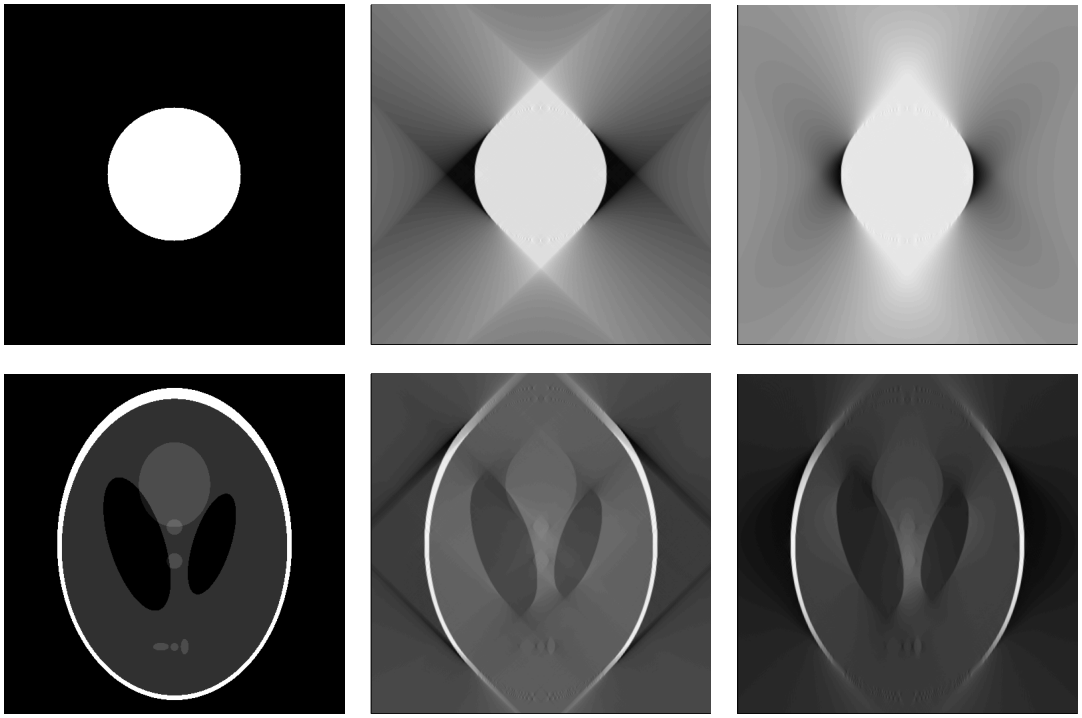

Figure 3.9: Limited angle reconstructions at the angular range $[-\Phi, \Phi]$, $\Phi = 45°$. Original images (left column), FBP reconstructions (middle column) and FBP reconstruction with artifact reduction (right column).

3.5 A microlocal approach to stabilization of limited angle tomography

In the last section of this chapter we draw our attention to the ill-posedness of the limited angle tomography. We will discuss that, in this case, the reconstruction problem is severely ill-posed. In particular, we will relate the severe ill-posedness of limited tomography to the existence of invisible singularities. Moreover, we will show that by integrating the inherent a-priori information about visible singularities (3.33) into the reconstruction, the inversion procedure can be stabilized. As a result, the degree of ill-posedness is reduced to $1/2$ (in the sense of Definition C.6) which equals to the degree of ill-posedness of the reconstruction problem at a full angular range, cf. Theorem 2.13.

3.5.1 A microlocal principle behind the severe ill-posedness

Our goal of this section is to understand the severe ill-posedness of limited angle tomography within the framework of microlocal analysis. Though most of the results about the severely ill-posed nature of limited angle tomography are well-known, we present them here for the sake of completeness. For more details we refer to the classical literature [Dav83], [Lou84, Lou86], [Nat86, NW01].

In order to study well-posedness of a problem it is the first task to check whether a unique

(a) $\varepsilon = 10°$ **(b)** $\varepsilon = 25°$ **(c)** $\varepsilon = 35°$

Figure 3.10: FBP reconstructions with artifact reduction. The effect of the parameter ε in the definition of κ_Φ on artifact reduction, cf. (3.42) and (3.45). Small values of ε lead to artifacts in the reconstruction.

reconstruction exists, cf. Definition C.1. We begin by noting that the reconstruction cannot be unique if the sought function has a non-compact support. This is due to the non-injectivity of the limited angle Radon transform $\mathcal{R}_\Phi$ which was shown in Corollary 3.7. Therefore, the severe ill-posedness in the case of non-compact support is reflected by the non-uniqueness of the reconstruction.

In what follows we consider the reconstruction problem for functions with compact support. In contrast to the case of non-compact support, the reconstruction is unique for every angular range $[-\Phi, \Phi]$, $0 \leq \Phi < \pi/2$:

Theorem 3.27 ([Nat86, Theorem II.3.5]). *Let $f \in L^2(\mathbb{R}^2)$ have compact support, and suppose $\mathcal{R}_\Phi f(\theta, \cdot) = 0$ for $\theta \in S^1_\Phi$. Then, $f \equiv 0$.* ⌟

Proof. The compact support of f implies that the Fourier transform $\hat{f}$ is analytic. By assumption and the Fourier slice theorem we get $\hat{f}(\sigma\theta) = (2\pi)^{-1/2}\widehat{\mathcal{R}_\Phi f}(\theta, \sigma) = 0$ for all $\sigma \in \mathbb{R}$ and $\theta \in S^1_\Phi$. Since no non-trivial analytic function can vanish on a set with a limit point, we get $\hat{f} \equiv 0$ and thus $f \equiv 0$. ∎

The result of Theorem 3.27 seems at the very first glance surprising since it guarantees a unique reconstruction even from a very small angular range. In particular, it guarantees that even invisible singularities (cf. Definition 3.21) can be reconstructed. However, the proof of the above theorem reveals that the reconstruction is highly unstable. Namely, it shows that reconstructing f from a limited angle data is equivalent to analytic continuation of $\hat{f}$, which is known to be extremely unstable. To see this, let us assume that $\hat{f}, \hat{g}$ are two analytic functions. Then, observe that the difference $\hat{f} - \hat{g}$ is analytic as well, and therefore unbounded if $\hat{f} - \hat{g}$ is not constant. Hence, if we are given perturbed data $\hat{f}_\eta := \hat{f} + \eta$, where $\|\eta\|_\infty < \varepsilon$, $\varepsilon > 0$, on some region $U \subseteq \mathbb{R}^2$, the analytic continuation $\hat{F}_\eta$ of $\hat{f}_\eta$ differs from the analytic continuation $\hat{F}$ of $\hat{f}$. Accordingly, the difference $\hat{F} - \hat{F}_\eta$ is unbounded which means that the reconstruction error might be arbitrarily large. This conclusion is true for every $\varepsilon > 0$. As a result, the analytic continuation and, hence, limited angle tomography is extremely unstable.

In particular, the above discussion shows that the reconstruction becomes extremely unstable

when trying to extrapolate values $\hat{f}(\xi)$ for $\xi \notin W_\Phi$. Note that these are exactly those values which contain the information about the invisible singularities. It seems therefore reasonable to conclude that the main instabilities of limited angle reconstruction occur due to the presence of invisible singularities.

Remark. Assuming the unknown function f to have compact support, the above discussion shows that, in order to get a perfect reconstruction from a limited angle data, the reconstruction algorithm has to perform analytic continuation in the Fourier domain. However, as we have shown in Theorem 3.9, the application of the filtered backprojection (FBP) algorithm to the limited angle data does not recover f but $P_\Phi f$. In this context, the FBP algorithm is not an appropriate reconstruction algorithm for limited angle tomography. ⌟

To quantify the degree of ill-posedness of the limited angle problem we first note the characterization via the singular value decomposition, cf. Definition C.5.

Theorem 3.28 (Singular values of the limited angle Radon transform, [Nat86, Sec. VI.2]). *Assume that $0 \le \Phi \le \pi/2$ and let $\Omega \subseteq \mathbb{R}^2$ be the unit ball of $\mathbb{R}^2$. Then, the singular values $\sigma_{m,l}$ (cf. Theorem B.7) of the limited angle Radon transform*

$$\mathcal{R}_\Phi : L^2(\Omega) \to L^2(Z_\Phi, (1-s^2)^{1/2})$$

are given by

$$\sigma_{m,l} = \left(\frac{2\pi}{m+1}\lambda_l(m+1, \Phi/\pi)\right)^{1/2}, \quad m \in \mathbb{N}_0,\ 0 \le l \le m,$$

where $\lambda_l(m+1, \Phi/\pi)$ satisfies the following condition: for each $0 < \vartheta < 1$ there are constants $c = c(\vartheta) > 0$ and $b = b(\vartheta)$ such that

$$0 \le 1 - \lambda_l(m+1, \Phi/\pi) \le ce^{-bm}, \ \text{for } l \le \vartheta\frac{2\Phi}{\pi}m, \tag{3.46}$$

$$0 \le \lambda_l(m+1, \Phi/\pi) \le ce^{-bm}, \ \text{for } l \ge \vartheta^{-1}\frac{2\Phi}{\pi}m. \tag{3.47}$$

In particular, the singular values $\sigma_{m,l}$ with $l \ge \vartheta^{-1}(2\Phi/\pi)m$ decay exponentially as $m \to \infty$. ⌟

Let us take a closer look at Theorem 3.28. To this end, let $(\sigma_{m,l}, f_{m,l}, g_{m,l})_{(m,l)\in\mathcal{I}}$ denote the singular value decomposition of $\mathcal{R}_\Phi$ and let $\mathcal{I} = \{(m,l) : m \in \mathbb{N}_0, 0 \le l \le m\}$ be the index set of all singular values. Then, by Theorem 3.28 and Theorem B.7, we can write

$$f = \sum_{(m,l)\in\mathcal{I}\setminus\mathcal{I}_0} c_{m,l} f_{m,l} + \sum_{(m,l)\in\mathcal{I}_0} c_{m,l} f_{m,l}, \tag{3.48}$$

where the coefficients $c_{m,l}$ are given by

$$c_{m,l} = \sigma_{m,l} \left\langle \mathcal{R}_\Phi f, g_{m,l} \right\rangle_{L^2(Z_\Phi, (1-s^2)^{1/2})},$$

and

$$\mathcal{I}_0 = \left\{(m,l) \in \mathcal{I} : \ l \ge \vartheta^{-1}(2\Phi/\pi)m\right\},$$

for some $0 < \vartheta < 1$. Now observe that, by (3.47), all but a small finite number of coefficients $c_{m,l}$ with $(m,l) \in \mathcal{I}_0$ are very close to 0. Therefore, the information content of these small coefficients is lost if the data $y = \mathcal{R}_\Phi f$ is corrupted by noise. In this case, the right hand sum in (3.48) consists only of a small (finite) number of summands. Since all singular functions $f_{m,l}$ are smooth, [Lou86], this sum represents a function which does not contain singularities. As a result, only those singularities of f can be reconstructed which have a representation with respect to the system $\{f_{m,l}\}_{m,l\in\mathcal{I}\setminus\mathcal{I}_0}$. In turn, these are exactly the visible singularities. This observation reflects again the microlocal correspondence that was noted in Theorem 3.20.

Finally, we note that the limited angle problem is also severely ill-posed in the sense of Definition C.6, cf. [Nat86, Sec. VI.2]. Also in this context, we will see that the reason for the severe ill-posedness can be explained within the framework of microlocal analysis.

Theorem 3.29. *Let $\alpha \in \mathbb{R}$, $0 \le \Phi \le \pi/2$ and let $\Omega \subseteq \mathbb{R}^2$ be the unit ball of $\mathbb{R}^2$. Then there is a function f such that, for some $C_\alpha > 0$,*

$$\|f\|_{H_0^\alpha(\Omega)} \not\le C_\alpha \|\mathcal{R}_\Phi f\|_{H^{\alpha+1/2}(Z_\Phi)}, \tag{3.49}$$

where

$$\|g\|_{H^\alpha(Z_\Phi)} = \int_{S^1_\Phi} \int_{\mathbb{R}} (1+\sigma^2)^\alpha \, |\hat{g}(\theta,\sigma)|^2 \, \mathrm{d}\sigma \, \mathrm{d}\theta.$$

That is, the left-hand side Sobolev space estimate (cf. Theorem 2.13) does not hold for the limited angle Radon transform. ⌟

Proof. In order to show that an estimate of the form (3.49) cannot hold, it is sufficient to choose a function $f \in H_0^\beta(\Omega)$ with $\beta < \alpha$ such that f has a singularity only with respect to an invisible direction. Then, according to Theorem 3.20, the limited angle Radon transform is $\mathcal{R}_\Phi f$ is smooth (i.e. $\mathcal{R}_\Phi f \in C^\infty(Z_\Phi)$) such that $\|\mathcal{R}_\Phi f\|_{H^{\alpha+1/2}(Z_\Phi)} < \infty$. However, since $f \notin H_0^\alpha(\Omega)$, $\|f\|_{H_0^\alpha(\Omega)} = \infty$. For a concrete example of such a function we refer to [Nat86, Sec. VI.2]. ∎

To sum up, we again emphasize that the main reason for the severe ill-posedness of limited angle tomography is the existence of invisible singularities.

3.5.2 A stabilization strategy for limited angle tomography

In the previous subsection we have shown that the reconstruction procedure becomes extremely unstable as soon as we are trying to reconstruct invisible singularities. In order to stabilize the inversion, it is therefore natural to reconstruct only that part of the sought function f which merely contains the visible singularities. For that reason, we aim at reconstructing functions f that satisfy $\mathrm{WF}(f) \subseteq \mathbb{R}^2 \times W_\Phi$, cf. (3.33). In order to integrate this a-priori information into a reconstruction procedure, we shall assume that

$$\operatorname{supp} \hat{f} \subseteq W_\Phi. \tag{3.50}$$

That is, our goal is to reconstruct $P_\Phi f = \mathcal{F}^{-1}(\chi_{W_\Phi} \hat{f})$ from the limited angle data $y = \mathcal{R}_\Phi f$, rather than f. Note that (3.50) implies $\mathrm{WF}(f) \subseteq \mathbb{R}^2 \times W_\Phi$, but not vice versa.

According to the above discussion, we formulate the *stabilized limited angle reconstruction problem* as follows:

$$\text{given } y^\delta = \mathcal{R}_\Phi f + \eta, \qquad \text{find an approximation to } P_\Phi f. \tag{3.51}$$

In this case, we can restore the Sobolev space estimate (3.49).

Theorem 3.30. *Let $f \in C_c^\infty(\Omega)$. Then, for each $\alpha \in \mathbb{R}$ we have*

$$\sqrt{4\pi}\, \|P_\Phi f\|_{H^\alpha(\mathbb{R}^2)} \leq \|\mathcal{R}_\Phi f\|_{H^{\alpha+1/2}(Z_\Phi)}\,. \tag{3.52}$$

⌟

Proof. The proof is according to [Nat86, Theorem II.5.1]. By using the Fourier slice Theorem 2.3, we first note that

$$\begin{aligned}\|\mathcal{R}_\Phi f\|^2_{H^{\alpha+1/2}(Z_\Phi)} &= \int_{S^1_\Phi}\int_{\mathbb{R}} (1+\sigma^2)^{\alpha+1/2}\, |\mathcal{F}(\mathcal{R}_\Phi f)(\theta,\sigma)|^2 \,\mathrm{d}\sigma\,\mathrm{d}\theta \\ &= 4\pi \int_{S^1_\Phi}\int_0^\infty (1+\sigma^2)^{\alpha+1/2}\, \left|\hat f(\sigma\theta)\right|^2 \,\mathrm{d}\sigma\,\mathrm{d}\theta.\end{aligned}$$

Substituting $\xi = \sigma\theta$ we get

$$\|\mathcal{R}_\Phi f\|^2_{H^{\alpha+1/2}(Z_\Phi)} = 4\pi \int_{W_\Phi} (1+|\xi|^2)^{\alpha+1/2}\, |\xi|^{-1} \left|\hat f(\xi)\right|^2 \,\mathrm{d}\xi, \tag{3.53}$$

$$\geq 4\pi \int_{\mathbb{R}^2} (1+|\xi|^2)^{\alpha} \left|\chi_{W_\Phi}(\xi)\hat f(\xi)\right|^2 \,\mathrm{d}\xi. \tag{3.54}$$

∎

Remark. For $f \in C_c^\infty(\Omega)$, it is straightforward to prove the right-hand side Sobolev estimate

$$\|\mathcal{R}_\Phi f\|_{H^{\alpha+1/2}(Z_\Phi)} \leq C_\alpha \|f\|_{H_0^\alpha(\mathbb{R}^2)}\,,$$

with some constant $C_\alpha > 0$. In order to prove this inequality, it is essential that f has compact support, [Nat86, Theorem 5.1]. However, an estimate of the form

$$\|\mathcal{R}_\Phi f\|_{H^{\alpha+1/2}(Z_\Phi)} \leq C_\alpha \|P_\Phi f\|_{H^\alpha(\mathbb{R}^2)}\,,$$

cannot be proven using the same technique. This is due to the fact that the support of $P_\Phi f$ cannot be compact even though f has compact support. ⌟

Theorem 3.30 shows that the reformulation of the limited angle reconstruction problem (3.3) according to (3.51) indeed stabilizes the reconstruction procedure. In this case, the degree of ill-posedness equals $1/2$ (in the sense of Definition C.6) which is the same as in the case of the full angular range, cf. Theorem 2.13. An appropriate reconstruction algorithm for the stabilized problem (3.51) is given by the filtered backprojection algorithm. This is due to the fact that the limited angle FBP implements an inversion formula for $P_\Phi f$, cf. Theorem 3.9. An artifact reduced version of the FBP algorithm for the problem (3.51) was derived in Section 3.4.

3.6 Summary and concluding remarks

The main goal of this chapter was to understand the image formation principle in limited angle tomography, and to explain all effects that can be observed in practical reconstructions, cf. Figure 3.1. For this purpose, we presented a detailed analysis of the limited angle backprojection operator and characterized the kernel of the limited angle Radon transform in $\mathcal{S}(\mathbb{R}^2)$, cf. Theorem 3.6 and Corollary 3.7, respectively. In addition, we derived an exact formula for filtered backprojection reconstructions at a limited angular range in Theorem 3.9. These characterizations showed that, given tomographic data at the limited angular range $[-\Phi, \Phi]$, only the part $P_\Phi f = \mathcal{F}^{-1}(\chi_{W_\Phi} \hat{f})$ can be reconstructed. In particular, these results explain why limited angle FBP does not perfectly recover the unknown function f.

In Section 3.3, we gave an interpretation of these characterizations in terms visible and invisible singularities at the limited angular range $[-\Phi, \Phi]$. In particular, we showed that a meaningful a-priori information can be extracted from the limited angle data, cf. (3.33). Section 3.4 was devoted to the characterization of limited angle artifacts and the development of an artifact reduction strategy for the filtered backprojection algorithm. These results were stated in Theorem 3.24 and Theorem 3.26. We also presented some numerical experiments on artifact reduction.

In Section 3.5, we discussed three aspects of the severe ill-posedness of limited angle tomography in the context of microlocal analysis. In particular, we showed that the existence of invisible singularities at a limited angular range is mainly responsible for the severe ill-posedness of the limited angle reconstruction problem. Based on this insight, we derived a stabilization strategy for limited angle tomography in Subsection 3.5.2. Basically, this is nothing but the integration of the inherent a-priori information (3.33) into the reconstruction problem.

CHAPTER 4

An adapted and edge-preserving reconstruction method for limited angle tomography

Thus far, we mainly studied the filtered backprojection (FBP) algorithm at a limited angular range. Its main advantage consists in the ability to produce efficacious reconstructions at a small cost. However, the FBP algorithm does not perform well in the presence of noise, [NW01], [Her09], [MS12]. Depending on the choice of the regularization parameter (cf. Subsection 2.4.1), the reconstructions appear either noisy or tend to oversmooth the edges, see Figure 4.1. However, it is of particular importance for medical imaging purposes to reliably reconstruct edges. The need for edge-preserving reconstruction in computed tomography is documented by various publications, see e.g. [DB95], [CD00, CG02], [YF02], [HHK+12], [Kla11, KRR11], most of which use a variant of the total variation reconstruction to preserve edges.

In the present chapter we develop a novel reconstruction algorithm for limited angle tomography that is stable and edge-preserving. We show that this algorithm may be adapted to the limited angle geometry by integrating the inherent a-priori information (3.33) into the reconstruction. As a result, the dimension of the problem can be significantly reduced yielding a considerable speedup of the algorithm while preserving the reconstruction quality.

This chapter is organized as follows. In Section 4.1 we briefly introduce the technique of sparse regularization and recall the definition of curvelets. In particular, we show that the combination of these mathematical tools yields a stable and edge-preserving reconstruction method which we call curvelet sparse regularization (CSR). In Section 4.2, we formulate an adapted version of curvelet sparse regularization (A-CSR) by integrating the inherent a-priori information of limited angle tomography (3.33) into the CSR method. Our main results are presented in Section 4.3, where we first derive an explicit formula for the Radon transform of curvelets and, in particular, prove a characterization of the kernel of the limited angle Radon transform in terms of curvelets. These results are presented in Theorem 4.7 and Theorem 4.8. In Theorem 4.10, we characterize CSR reconstructions at limited angular range. In particular, we show that the adapted approach (A-CSR) leads to the same reconstructions as the non-adapted curvelet sparse regularization. Finally, in Section 4.4, we derive an explicit formula for CSR reconstructions at a full angular range and discuss the relation of CSR to the "curvelet thresholding" approach of [CD02].

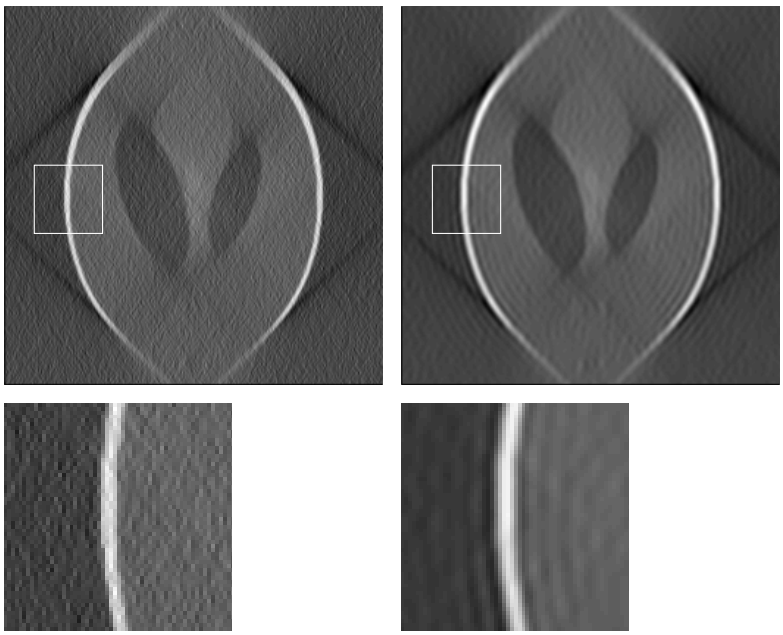

Figure 4.1: Filtered backprojection reconstructions from a noisy data set (noiselevel=2%) at the angular range $[-\Phi, \Phi]$, $\Phi = 45°$ using the Ram-Lak filter with different bandwidths, cf. Section 2.4.1. Top left image was reconstructed using a large bandwidth, whereas the top right image was generated by using a small bandwidth. The second row shows a zoom of the white rectangular regions of the reconstructions in the top row. Reconstructions on the left show poor noise performance while the edges are well preserved. However, the images on the right reveal the opposite phenomenon: The noise performance seems to be quite good, whereas the edges appear to be blurred.

Essential parts of the present chapter were published in the Journal of Applied and Computational Harmonic Analysis [Fri12]. Moreover, the results of Section 4.3 were announced in the Proceedings in Applied Mathematics and Mechanics, [Fri11]. We also note that an alternative approach to adapted curvelet sparse regularization was published in the Proceedings of IEEE International Symposium on Biomedical Imaging, [Fri10].

4.1 A stable and edge-preserving reconstruction method

In this section we develop a stable and edge-preserving reconstruction method for the limited angle reconstruction problem

$$y^\delta = \mathcal{R}_\Phi f + \eta, \tag{4.1}$$

where η denotes the noise level $\delta > 0$, i.e., $\|\eta\|_2^2 = \delta$. In order to stabilize the inversion, it is necessary to integrate additional prior knowledge about the solution into the reconstruction procedure, [EHN96], [Kir96]. A common approach is to use variational formulation of the reconstruction problem, [SGG+09]. In this context, a regularized solution f_α is obtained as a minimizer of the so-called Tikhonov functional,

$$f_\alpha = \arg\min_f \left\{ \left\| \mathcal{R}_\Phi f - y^\delta \right\|_2^2 + \alpha \Lambda(f) \right\}, \tag{4.2}$$

where $\alpha > 0$ denotes the regularization parameter and $\Lambda : \mathrm{dom}(\Lambda) \to [0, \infty]$ is the so-called prior (or regularization) functional. The first term in (4.2) controls the data error, whereas the second term encodes the prior information about the sought object f.

The choice among various prior terms Λ and, thus, regularization techniques, depends on the specific object (which is imaged) and, to some extent, on the desire to preserve or emphasize particular features. A classical strategy is to enforce smoothness of the solution. In this case, it is appropriate to choose Λ to be a smoothness (semi-) norm, [EHN96], [Kir96]. For example, the Besov norm, which allows to adjust the smoothness of the solution at a very fine scale [KSJ$^+$03], [LT08], [RVJ$^+$06].

In what follows, our goal is to design a penalty functional which does not smooth edges. The most prominent prior functional Λ that is used for edge-preserving reconstruction is the total variation (TV) seminorm, see e.g. [HSP11], [HKK$^+$12]. However, as it was pointed out in [HD08], TV reconstruction may not be an appropriate choice for medical imaging purposes. One reason for this is that TV regularization favors piecewise constant functions and, hence, produces staircase effects which may destroy relevant information [CCN07], [Rin00]. To overcome this problem, higher order total variation priors were considered by some authors, see for example [BKP10].

In this section, we apply a different regularization strategy, where instead of enforcing smoothness, sparsity of the solution is enforced with respect to some dictionary (function system), [DDDM04]. Moreover, we will show that by using the curvelet dictionary, [CD05b], this regularization method gives rise to an edge-preserving reconstruction technique.

4.1.1 Regularization by sparsity constraints

In what follows we assume $\{\psi_n\}_{n\in\mathcal{I}}$ to be a frame of $L^2(\Omega)$ with a countable index set $\mathcal{I}$, cf. [Chr03]. That is, for some constants $A, B > 0$ we assume that

$$A\,\|f\|_2^2 \le \sum_{n\in\mathcal{I}} |\langle f, \psi_n\rangle|^2 \le B\,\|f\|_2^2\,, \qquad \text{for all } f \in L^2(\Omega).$$

Moreover, we define the *analysis operator* $T : L^2(\Omega) \to \ell^2(\mathcal{I})$ and the *synthesis operator* $T^* : \ell^2(\mathcal{I}) \to L^2(\Omega)$ by

$$Tf = \{\langle \psi_n, f\rangle\}_{n\in\mathcal{I}}\,, \quad T^*c = \sum_{n\in\mathcal{I}} c_n\psi_n. \tag{4.3}$$

Then, the reconstruction problem (4.1) can expressed with respect to the frame coefficients c via

$$y^\delta = Kc + \eta, \quad K := \mathcal{R}_\Phi T^*. \tag{4.4}$$

We are therefore interested in the recovery of the frame coefficients $c = (c_n)_{n\in\mathcal{I}}$ of f rather than the function f itself.

In order to stabilize the reconstruction problem (4.4), we will assume that the sought function f is sparse with respect to the frame $\{\psi_n\}_{n\in\mathcal{I}}$. That is, we assume that the coefficients $c \in \ell^2(\mathcal{I})$ in the representation $f = T^*c$ have only finitely many entries which are different from zero. Thus, our regularization strategy is to determine a solution of the problem (4.1) such that it is sparse with respect to the frame $\{\psi_n\}_{n\in\mathcal{I}}$. The integration of the sparsity assumptions into the reconstruction

procedure can be achieved by using variational formulation (4.2) with the following regularization term [DDDM04], [BL08b], [GHS08], [Lor09a],

$$\Lambda_{w,p}(c) =: \|c\|_{w,p}^p = \sum_{n\in\mathcal{I}} w_n \left|\langle f, \psi_n\rangle\right|^p , \tag{4.5}$$

where $w = (w_n)_{n\in\mathcal{I}}$ is a weight sequence satisfying $w_n \geq \varepsilon > 0$ for some $\varepsilon > 0$, and $1 \leq p \leq 2$.

To sum up, regularization by sparsity constraints yields a solution of (4.4) by minimizing the following Tikhonov type functional,

$$c_{w,p} = \operatorname*{arg\,min}_{c\in\mathbb{C}^{\mathcal{I}}} \left\{ \frac{1}{2} \left\| Kc - y^\delta \right\|^2_{L^2(S^1\times\mathbb{R})} + \|c\|_{w,p}^p \right\}. \tag{4.6}$$

A regularized reconstruction $f_{w,p}$ for the original problem (4.1) is then obtained by applying the synthesis operator to the regularized coefficients $c_{w,p}$, i.e., $f_{w,p} = T^* c_{w,p}$.

We shall now show that sparse regularization (4.6) of the reconstruction problem (4.1) is well-posed in the sense that a minimizer $c_{w,p}$ exists and continuously depends on the data y^δ. To this end, for $1 \leq p \leq 2$, we define the following shrinkage operator $\mathcal{S}_w^p : \ell^2(\mathcal{I}) \to \ell^2(\mathcal{I})$ by

$$(\mathcal{S}_w^p(c))_n = S^p_{w_n}(x_n) := \begin{cases} \operatorname{sgn}(c_n)\max\{0, |c_n| - w_n\}, & p = 1 \\ G^{-1}_{w_n,p}(c_n) & 1 < p < 2, \\ c_n/(1+2w_n) & p = 2, \end{cases} \tag{4.7}$$

where $G^{-1}_{w_n,p}$ denotes the inverse function of $G_{w_n,p}(y) = y + w_n p \operatorname{sgn}(y)\,|y|^{p-1}$, [Lor09a]. For $p = 1$, the operator $\mathcal{S}_w^1$ is the well-known *soft-thresholding operator* and will be denoted by $\mathcal{S}_w$.

The following proposition follows from results in [GHS08], [Lor09a].

Proposition 4.1. *For every $y^\delta \in L^2(\Omega)$ the Tikhonov functional*

$$\mathcal{T}_{w,p}(c) = \frac{1}{2} \left\| Kc - y^\delta \right\|^2_{L^2(S^1\times\mathbb{R})} + \|c\|_{w,p}^p , \tag{4.8}$$

has a minimizer in $L^2(\Omega)$. Furthermore, for any $\gamma > 0$, the minimizer $c_{w,p}$ of $\mathcal{T}_{w,p}$ is characterized by the fixed point equation

$$c_{w,p} = \mathcal{S}^p_{\gamma w}\left(c_{w,p} - \gamma K^*(Kc_{w,p} - y^\delta)\right). \tag{4.9}$$

⌟

The following proposition shows that regularization by sparsity constraints (4.6) indeed enforces sparsity of the solution.

Proposition 4.2 ([GL08]). *For $p = 1$, each minimizer $c_{w,1}$ of (4.8) is finitely supported. For $1 < p \leq 2$, it holds that $c_{w,p} \in \ell^{2(p-1)}_{w^2}$, where $\ell^q_{w^2} = \{c : \|c\|^q_{w^2,q} \leq \infty\}$ for $q = 2(p-1)$ and $w^2 = (w_n^2)_{n\in\mathcal{I}}$.* ⌟

Finally, we note that sparse regularization is a regularization method in the sense of Appendix C, Definition C.7. The following theorem follows directly by applying [GHS08, Remark 3 and Proposition 7] to the limited angle Radon transform.

Theorem 4.3. *Let $1 \leq p \leq 2$. Assume that the operator equation $Kc = y$ attains a solution in $\ell^p_w = \{c \in \mathbb{C}^{\mathcal{I}} : \|c\|_{w,p} < \infty\}$, and that $\alpha : \mathbb{R}_+ \to \mathbb{R}_+$ satisfies*

$$\lim_{\delta \to 0} \alpha(\delta) = 0, \qquad \lim_{\delta \to 0} \frac{\delta^p}{\alpha(\delta)} = 0.$$

Let $\delta_k \to 0$ and let $y_k \in L^2(S^1 \times \mathbb{R})$ satisfy $\|y - y_k\|_{L^2(S^1 \times \mathbb{R})} \leq \delta_k$. Moreover, let $\alpha_k = \alpha(\delta_k)$ and

$$c^k_{w,p} \in \arg\min \left\{ \frac{1}{2} \|Kc - y_k\|^2_{L^2(S^1 \times \mathbb{R})} + \alpha_k \|c\|^p_{w,p} \right\}.$$

Then, there exists a solution $c^\dagger$ of $Kc = y$ of minimal $\|\cdot\|_{w,p}$-norm and a subsequence $c^{k_j}_{w,p}$ such that

$$\lim_{j \to \infty} \left\| c^{k_j}_{w,p} - c^\dagger \right\|_2 = 0. \qquad \lrcorner$$

4.1.2 A multiscale dictionary for sparse and edge-preserving representations

In the previous section we have shown that imposing sparsity constraints on the solution stabilizes the reconstruction problem of limited angle tomography. However, in order to make this method applicable in practice, we still need to specify the dictionary $\{\psi_n\}_{n \in \mathcal{I}}$. An essential requirement on the dictionary $\{\psi_n\}_{n \in \mathcal{I}}$ is the ability to provide sparse representation of a large class of functions, cf. Subsection 4.1.1. This is necessary in order that the regularized solution is a good approximation of the sought function, cf. Proposition 4.2. In addition to the stabilizing property of the reconstruction method, it is our goal to design an inversion technique that is edge-preserving. To achieve this, our idea consists in combining the technique of sparse regularization with a dictionary that provides sparse and edge-preserving representations. In this subsection, we introduce curvelets, [CD05b], [MP10], to address the problem of finding an appropriate dictionary. Moreover, we give an adequate definition of a class of functions with edges and show that these function can be efficiently approximated by curvelets, [CD04].

The curvelet dictionary

We briefly recall the definition of the curvelet frame. For details we refer to [CD05b], [MP10]. Conceptually, the curvelet dictionary is a wavelet type dictionary that has a multiscale structure and whose elements are highly directional functions. As opposed to wavelets, the curvelet dictionary is not generated by a single mother curvelet. Rather, the generating functions vary from one scale to another.

At scale 2^{-j}, $j \in \mathbb{N}_0$, the generating curvelets $\psi_{j,0,0} : \mathbb{R}^2 \to \mathbb{R}$ are defined in the frequency domain by using polar coordinates (r, ω) as follows:

$$\widehat{\psi}_{j,0,0}(r, \omega) = 2^{-3j/4} \cdot W(2^{-j} \cdot r) \cdot V\left(\frac{2^{\lceil j/2 \rceil + 1}}{\pi} \cdot \omega \right), \tag{4.10}$$

where $W(r)$ is a radial window and $V(\omega)$ is an angular window, respectively. The windows W and

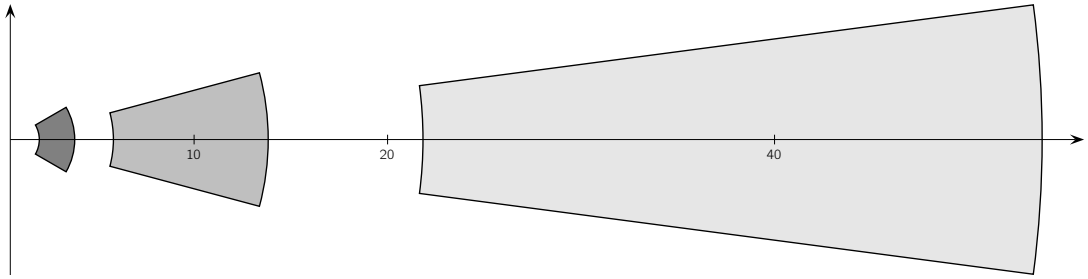

Figure 4.2: Support of curvelets in the Fourier domain for $j = 1$ (dark gray), $j = 3$ (gray) and $j = 5$ (light gray). A similar image can be found in [MP10].

V are assumed to be real and smooth ($W, V \in C^\infty(\mathbb{R})$), such that

$$\operatorname{supp} W \subseteq (1/2, 2), \quad \operatorname{supp} V \subseteq (-1, 1).$$

Moreover, we assume the following admissibility conditions to be satisfied,

$$\begin{aligned} \sum_{j=-\infty}^{\infty} W^2(2^j r) &= 1, \quad r \in (3/4, 3/2); \\ \sum_{l=-\infty}^{\infty} V^2(\omega - l) &= 1, \quad \omega \in (-1/2, 1/2). \end{aligned} \tag{4.11}$$

The family of curvelets $\{\psi_{j,l,k}\}_{j,l,k}$ is now constructed by translation and rotation of generating curvelets $\psi_{j,0,0}$. That is, at scale 2^{-j}, the curvelet $\psi_{j,l,k}$ is defined via

$$\psi_{j,l,k}(x) = \psi_{j,0,0}(R_{\theta_{j,l}}(x - b_k^{j,l})), \tag{4.12}$$

where

$$R_{\theta_{j,l}} = \begin{pmatrix} \cos\theta_{j,l} & -\sin\theta_{j,l} \\ \sin\theta_{j,l} & \cos\theta_{j,l} \end{pmatrix} \tag{4.13}$$

denotes the rotation matrix with respect to the scale-dependent rotation angles $\theta_{j,l}$ and the scale-dependent locations $b_k^{j,l}$ which are defined by

$$\begin{aligned} \theta_{j,l} &= l \cdot \pi \cdot 2^{-\lceil j/2 \rceil - 1}, \quad -2^{\lceil j/2 \rceil + 1} \leq l < 2^{\lceil j/2 \rceil + 1}, \\ b_k^{j,l} &= R_{\theta_{j,l}}^{-1}\left(\frac{k_1}{2^j}, \frac{k_2}{2^{j/2}}\right), \quad k = (k_1, k_2)^\intercal \in \mathbb{Z}^2. \end{aligned} \tag{4.14}$$

Since the window functions W and V are compactly supported, and in particular, since the support of $W(2^j \cdot)$ is contained in $(1/2, \infty)$, it follows from (4.10) and (4.12) that each curvelet is supported on a polar wedge in the Fourier domain which has a positive distance to the origin, cf. Figure 4.2. Thus, we have $\hat{\psi}_{j,l,k}(\xi) = 0$ for all $|\xi| < 1/2$ and all admissible indices (j, l, k)

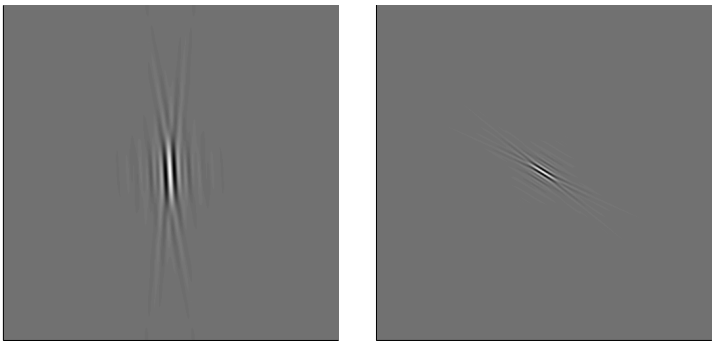

(a) $\psi_{5,0,0}$ **(b)** $\psi_{6,5,0}$

Figure 4.3: Curvelets at different scales and different orientations. Left image shows a curvelet with orientation $\theta_{5,0} = 0°$ whereas the right image shows a curvelet with orientation $\theta_{6,5} = 56.25°$.

according to (4.14). As a result, the region $\bigcup_{(j,l,k)} \operatorname{supp} \hat{\psi}_{j,l,k}$ does not cover all of the $\mathbb{R}^2$ and the system $\{\psi_{j,l,k}\}$ does not contain any low-pass element.

To finish the definition of the curvelet system we define the generating low-pass function $\psi_{-1,0,0}$ in the Fourier domain by

$$\widehat{\psi}_{-1,0,0}(r,\omega) = W_0(r), \quad W_0^2(r) := 1 - \sum_{j=0}^{\infty} W^2(2^{-j}r)$$

and complete the curvelet system by all of its translates $\{\psi_{-1,0,k}\}_{k\in\mathbb{Z}^2}$. Then, the index set of the (completed) curvelet dictionary is given by

$$\mathcal{I} = \left\{(-1,0,k) : \ k \in \mathbb{Z}^2\right\} \cup \left\{(j,l,k) : \ j \in \mathbb{N}_0,\, k \in \mathbb{Z}^2,\, -2^{\lceil j/2\rceil+1} \le l < 2^{\lceil j/2\rceil+1}\right\}. \tag{4.15}$$

Note that each index $(j,l,k) \in \mathcal{I}$ has a 3 parameter structure, where j denotes the *scale*-parameter, $k = (k_1,k_2)$ is the *location* parameter and l is the *orientation* parameter.

Remark. In the spatial domain, the support of curvelets is concentrated around an ellipse which is located near $b_k^{j,l}$ and oriented along the orthogonal direction $\theta_{j,l}^{\perp} = \theta_{j,l} + \pi/2$. The directional localization becomes higher when the scale parameter j increases. Consequently, curvelets are highly oriented at fine scales, see Figure 4.3. ⌟

The curvelet dictionary $\{\psi_{j,l,k}\}_{(j,l,k)\in\mathcal{I}}$ now provides a tiling of the frequency plane, cf. Figure 4.4, and is complete in the sense that it constitutes a tight frame for $L^2(\mathbb{R}^2)$, [CD05b]. That is, for each $f \in L^2(\mathbb{R}^2)$ there is a curvelet representation

$$f = \sum_{(j,l,k)\in\mathcal{I}} \langle \psi_{j,l,k}, f\rangle \psi_{j,l,k} \tag{4.16}$$

and a Parseval relation

$$\|f\|^2_{L^2(\mathbb{R}^2)} = \sum_{(j,l,k)\in\mathcal{I}} \left|\langle \psi_{j,l,k}, f\rangle\right|^2.$$

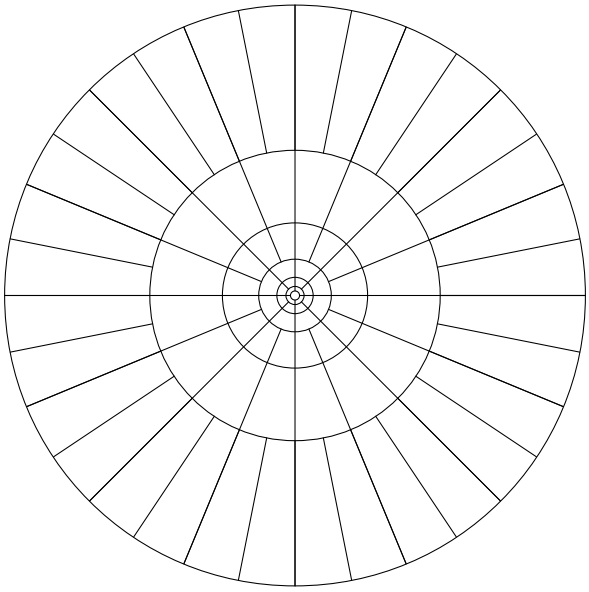

Figure 4.4: Tiling of the frequency plane corresponding to the curvelet dictionary, [CD04].

We conclude our exposition on curvelets with the following example of curvelet window functions W and V that satisfy the admissibility conditions (4.11).

Example. For an explicit construction of a curvelet according to (4.11), the following window functions may be used, [MP10]:

$$W(r) = \begin{cases} \cos\left(\frac{\pi}{2}\nu\left(5-6r\right)\right) & \frac{2}{3} \le r \le \frac{5}{6}, \\ 1 & \frac{5}{6} \le r \le \frac{4}{3}, \\ \cos\left(\frac{\pi}{2}\nu\left(3r-4\right)\right) & \frac{4}{3} \le r \le \frac{5}{3}, \\ 0 & \text{else}, \end{cases}$$

$$V(\omega) = \begin{cases} 1 & |\omega| \le \frac{1}{3}, \\ \cos\left(\frac{\pi}{2}\nu\left(3\,|\omega|-1\right)\right) & \frac{1}{3} \le |\omega| \le \frac{2}{3}, \\ 0 & \text{else}, \end{cases}$$

where

$$\nu(x) = \begin{cases} 0 & x \le 0, \\ \dfrac{s(x-1)}{s(x-1)+s(x)} & 0 < x < 1, \\ 1 & x \ge 1 \end{cases} \quad \text{with} \quad s(x) = \exp\left(-\frac{1}{(1+x)^2} - \frac{1}{(1-x)^2}\right).$$

The corresponding low-pass window W_0 is given by

$$W_0(r) = \begin{cases} 1 & 0 \le r \le \frac{2}{3}, \\ \sin\left(\frac{\pi}{2}\nu(5-6r)\right) & \frac{2}{3} \le r \le \frac{5}{6}, \\ 0 & \text{else}. \end{cases}$$

⌟

Efficient representation of edges via curvelets

We finally note that the curvelet dictionary provides a sparse representation of functions with edges. The following results were proven in [CD04]. We summarize these results in order to make this work self-contained. First of all, we need to formally specify the notion of an edge.

For this purpose, let $\varrho : [0, 2\pi) \to [0, 1]$ be a radius function and consider the following subsets of $\mathbb{R}^2$,

$$B = \left\{ x \in \mathbb{R}^2 : \; x = (r\cos\theta, r\sin\theta),\; r \leq \varrho(\theta) \right\}. \tag{4.17}$$

In particular, the boundary ∂B is parametrized by the curve $\gamma(\theta) = (\varrho(\theta)\cos\theta, \varrho(\theta)\sin\theta)$. In what follows, we are interested in those sets $B \subseteq \mathbb{R}^2$ (defined by (4.17)) whose curvature is bounded by a constant $A > 0$, i.e.,

$$\sup_{\theta\in[0,2\pi)} \left|\varrho''(\theta)\right| < A, \quad \varrho < \varrho_0 < 1. \tag{4.18}$$

Furthermore, we define

$$\mathrm{STAR}^2(A) = \left\{ B \subseteq [0,1]^2 : \; B \text{ is a translate of a set obeying (4.17) and (4.18)} \right\}. \tag{4.19}$$

We are now able to define the set of *functions which are C^2 away from C^2 edges* as

$$\mathcal{E}^2(A) = \left\{ f_1 + f_2\chi_B : \; B \in \mathrm{STAR}^2(A),\; f_1, f_2 \in C^2(\mathbb{R}^2),\; \mathrm{supp}(f_1), \mathrm{supp}(f_2) \subseteq [0,1]^2 \right\}.$$

For this class of functions, the following approximation result holds.

Theorem 4.4 ([CD04]). *Let $f \in \mathcal{E}^2(A)$ and $N \in \mathbb{N}$. Then, the curvelet dictionary $\{\psi_{j,l,k}\}_{(j,l,k)\in\mathcal{I}}$ exhibits the following approximation rate*

$$\|f - f_N\|_2^2 = O(N^{-2}(\log N)^3), \; \text{as } N \to \infty,$$

where

$$f_N = \sum_{(j,l,k)\in\mathcal{I}_N} \langle f, \psi_{j,l,k}\rangle \psi_{j,l,k}$$

is the best N-term approximation and $\mathcal{I}_N \subseteq \mathcal{I}$ is the index set corresponding to the N largest magnitudes of curvelet coefficients $|\langle f, \psi_{j,l,k}\rangle|$. ⌟

The function class $\mathcal{E}^2(A)$ will serve us as a model for functions with edges. By Theorem 4.4, the curvelet dictionary provides a nearly optimal approximation rate (compare to the remark below) for this class of functions. For the same class of functions, wavelet dictionaries typically exhibit an approximation rate, [MP07],

$$\|f - f_N\|_2^2 = O(N^{-1}), \; \text{as } N \to \infty,$$

which is far away from the optimal theoretical approximation rate described in the following remark.

Remark. Under weak technical assumptions, the optimal approximation rate is given by

$$\|f - f_N\|_2^2 = O(N^{-2}),$$

and can be achieved theoretically using adaptive triangulations, see e.g. [CD04] and references therein. However, there is no practical algorithm that can achieve this approximation rate for relatively complex images f, [MP07]. ⌟

4.1.3 Curvelet sparse regularization (CSR)

In previous Subsections 4.1.1 and 4.1.2 we have separately introduced a stabilization strategy which is based on sparsity assumptions and a multiscale dictionary that provides an efficient sparse representation of functions that are C^2 away from C^2 edges. In this subsection we shall combine both of these techniques in order to get a stable and edge-preserving reconstruction method for limited angle tomography which we will refer by the term *curvelet sparse regularization* or CSR.

Since we are interested in applying the reconstruction technique to a practical situation, we consider the discrete version of the reconstruction problem. To this end, we model f as a finite linear combination of curvelets, i.e.,

$$f = \sum_{n=1}^{N} c_n \psi_n, \tag{4.20}$$

where $\mathcal{I}_N \subseteq \mathcal{I}$, $|\mathcal{I}_N| = N \in \mathbb{N}$, denotes a finite subset of the curvelet index $\mathcal{I}$ set, cf. (4.15), and $n = n(j,l,k)$ is an enumeration of $\mathcal{I}_N$. Moreover, we assume to be given a finite number of measurements $y_m = \mathcal{R}_\Phi f(\theta_m, s_m)$, $1 \le m \le M \in \mathbb{N}$. Then, by (4.20), each measurement y_m can be expressed as

$$y_m = \mathcal{R}_\Phi f(\theta_m, s_m) = \sum_{n=1}^{N} c_n \mathcal{R}_\Phi \psi_n(\theta_m, s_m). \tag{4.21}$$

Now, by defining the so-called *system matrix* $\mathrm{K} \in \mathbb{C}^{M\times N}$,

$$\mathrm{K}_{m,n} = \mathcal{R}_\Phi \psi_n(\theta_m, s_m), \quad 1 \le m \le M,\ 1 \le n \le N, \tag{4.22}$$

the discrete version of the limited angle problem (4.4) can be expressed as

$$y^\delta = \mathrm{K}c + \eta, \tag{4.23}$$

where $y^\delta \in \mathbb{R}^M$ denotes the vector of noisy measurements, and $c \in \mathbb{C}^N$ is a vector of curvelet coefficients. Note that the matrix K is the discrete version of the continuous operator $K = \mathcal{R}_\Phi T^*$, cf. (4.4), where T^* denotes the synthesis operator with respect to the curvelet frame, i.e., $f = T^* c$, cf. (4.3).

To solve the discrete problem (4.23), we propose the use of curvelet sparse regularization technique, where a regularized vector of curvelet coefficients $c_{w,p} \in \mathbb{C}^N$ is computed by solving the minimization problem, cf. Subsection 4.1.1,

$$c_{w,p} \in \operatorname*{arg\,min}_{c\in\mathbb{C}^N} \left\{ \frac{1}{2} \left\| \mathrm{K}c - y^\delta \right\|_{L^2(Z)}^2 + \|c\|_{w,p}^p \right\}. \tag{CSR}$$

A regularized reconstruction $f_{w,p}$ for the original limited angle problem (2.25) is subsequently obtained by applying the synthesis operator T^* to the vector $c_{w,p}$, i.e.,

$$f_{w,p} = T^* c_{w,p} = \sum_{n=1}^{N} (c_{w,p})_n \, \psi_n.$$

Eventually, we point out that curvelet sparse regularization is a stable and edge-preserving reconstruction method. This is because of the fact that, on the one hand, the technique of sparse regularization is a regularization method which enforces sparsity with respect to the curvelet frame and, on the other hand, sparse representations with respect to curvelets are edge-preserving, cf. Subsections 4.1.1 and 4.1.2. However, we have to note that curvelet sparse regularization (CSR) preserves only those edges which have visible directions. This is due to the fact that the limited angle Radon transform smoothes invisible singularities, cf. Section 3.3. Moreover, we note that CSR is not yet adapted to the limited angular range. That is, in order to solve the discrete problem (4.23), we need to compute $(c_{w,p})_n$ for all possible curvelet indices $n \in \mathcal{I}_N$. Hence, the dimension of the reconstruction problem (4.23), which is given by $N = |\mathcal{I}_N|$, does not depend on the available angular range. In the next section, we shall show that it is possible to make the dimension of the reconstruction problem (4.23) dependent on the angular range, and hence to adapt the method of sparse regularization to the limited angle tomography.

4.2 Adapted curvelet sparse regularization (A-CSR)

The goal of this section is to formulate an *adapted curvelet sparse regularization* (A-CSR) for the limited angle tomography. To this end, we will apply the stabilization strategy of Section 3.5, which consists in determining a solution f_Φ of the limited angle problem $\mathcal{R}_\Phi f = y$, such that f_Φ is an approximation to $P_\Phi f = \mathcal{F}^{-1}(\chi_{W_\Phi} \hat{f})$. To achieve that, we aim at reconstructing a vector of curvelet coefficients $c_\Phi \in \mathbb{C}^N$ via CSR such that the Fourier transform of $f_\Phi = \sum_{n=}^{N} (c_\Phi)_n \, \psi_n$ is supported near the wedge W_Φ, i.e., $W_\Phi \subseteq \operatorname{supp} \hat{f}_\Phi$ and such that the area $|\operatorname{supp} \hat{f}_\Phi \setminus W_\Phi|$ is small.

First, we need to formulate the constraint "$\hat{f}$ is supported near W_Φ" in terms of curvelet coefficients. To this end, note that a function $f = \sum_{n \in \mathcal{I}_N} c_n \psi_n$ is supported near W_Φ if the following condition is satisfied, cf. Figure 4.5,

$$c_n = 0 \text{ for all } n \in \mathcal{I}_N \text{ with } \operatorname{supp} \hat{\psi}_n \cap W_\Phi = \emptyset. \tag{4.24}$$

Therefore, we have to ensure that the adapted CSR reconstructions curvelet coefficients which satisfy the condition (4.24).

Before integrating the constraint (4.24) into the curvelet sparse regularization, we further note that functions f whose Fourier transform is supported near W_Φ may only contain singularities $(x, \xi) \in \mathrm{WF}(f)$ with directions $\xi \in W_\Phi$. These are exactly the visible singularities at the angular range $[-\Phi, \Phi]$, cf. Subsection 3.3.2. In accordance with Definition 3.21, we now make the following definition.

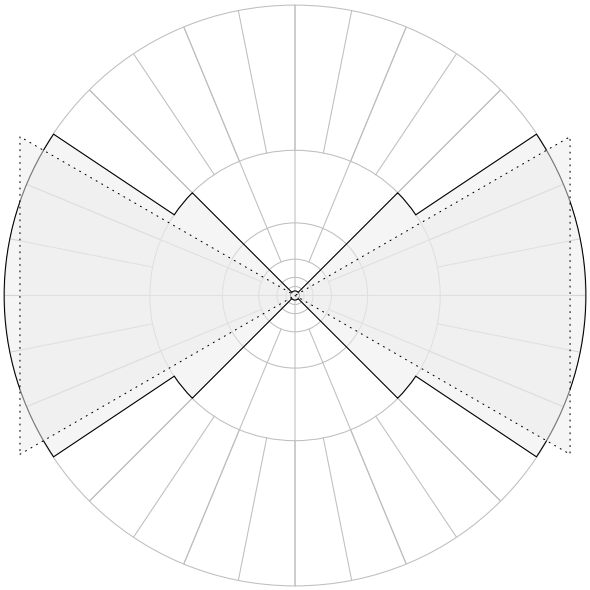

Figure 4.5: The support of the adapted CSR reconstructions in the frequency plane (gray shaded area enclosed in a solid line) for the angular range $[-\Phi, \Phi]$, $\Phi = 30°$. The polar wedge W_Φ is indicated by the gray shaded area enclosed in a dotted line.

Definition 4.5. *Let* $0 \leq \Phi \leq \pi/2$*. Then, we define the* index set of visible curvelet coefficients at the angular range $[-\Phi, \Phi]$ *by*

$$\mathcal{I}_\Phi = \left\{(j,l,k) \in \mathcal{I}_N : \operatorname{supp} \hat{\psi}_{j,l,k} \cap W_\Phi \neq \emptyset\right\}. \tag{4.25}$$

The corresponding index set of invisible curvelet coefficients at the angular range $[-\Phi, -\Phi]$ *is defined by*

$$\mathcal{I}_\Phi^{\text{invisible}} = \mathcal{I}_N \setminus \mathcal{I}_\Phi. \tag{4.26}$$

Accordingly, the curvelets $\psi_{j,l,k}$ *as well as the curvelet coefficients* $c_{j,l,k}$ *are called* visible at the angular range $[-\Phi, \Phi]$*, if their indices satisfy* $(j,l,k) \in \mathcal{I}_\Phi$*. Otherwise they are called* invisible. ⌟

Let us get back to the formulation of the adapted curvelet sparse regularization. We need to integrate the condition (4.24) into the CSR reconstruction method. Since, we a-priori assume that $c_n = 0$ for all $n \in \mathcal{I}_\Phi^{\text{invisible}}$, we have to reconstruct only the visible curvelet coefficients $(c_n)_{n \in \mathcal{I}_\Phi}$. To this end, we reformulate the non-adapted problem (4.23) with respect to visible curvelet coefficients, i.e. , we assume that the unknown function has a representation with respect to visible curvelets such that $f = \sum_{n \in \mathcal{I}_\Phi} c_n \psi_n$. Proceeding as in Subsection 4.1.3, we define an *adapted system matrix* K_Φ with respect to the visible index set $\mathcal{I}_\Phi$ by

$$(\mathrm{K}_\Phi)_{m,n} = \mathcal{R}_\Phi \psi_n(\theta_m, s_m), \quad 1 \leq m \leq M,\ 1 \leq n \leq N_\Phi, \tag{4.27}$$

where $N_\Phi = |\mathcal{I}_\Phi|$, and $n = n(j,l,k)$ denotes an enumeration of $\mathcal{I}_\Phi$. We are now able to formulate the *adapted (or reduced) limited angle problem* as

$$y^\delta = \mathrm{K}_\Phi c + \eta. \tag{4.28}$$

Consequently, the *adapted curvelet sparse regularization* (A-CSR) is given by the application of the CSR method to the problem (4.28), i.e.,

$$c_{w,p}^{\Phi} = \operatorname*{arg\,min}_{c \in \mathbb{C}^{N_\Phi}} \left\{ \frac{1}{2} \left\| \mathrm{K}_\Phi c - y^\delta \right\|_{L^2(Z)}^2 + \|c\|_{w,p}^p \right\}. \tag{A-CSR}$$

An adapted reconstruction $f_{w,p}^{\Phi}$ may be computed by,

$$f_{w,p}^{\Phi} = \sum_{n \in \mathcal{I}_\Phi} (c_{w,p}^{\Phi})_n \, \psi_n. \tag{4.29}$$

We conclude this section with some remarks on the A-CSR method.

Remarks.

- First of all, let us point out that the adaption of the problem (4.28) is reflected by the fact that the reconstruction problem is formulated with respect to an adaptively selected curvelet subdictionary $\{\psi_n\}_{n \in \mathcal{I}_\Phi}$, where the size of the dictionary depends on the angular range. Thus, the adapted system matrix K_Φ is a submatrix of the non-adapted system matrix (4.22). Moreover, since the problem is formulated with respect to a smaller dictionary, this entails a dimensionality reduction in the curvelet domain, where the dimension of the problem (4.28) is highly dependent on the angular range $[-\Phi, \Phi]$. Apparently, the dimension of the adapted problem (4.28) increases as the angular range increases, and vice versa. As a consequence, the computational amount decreases significantly by using the A-CSR framework instead of CSR. In Chapter 5, we will present some numerical results confirming this issue.
- The adapted curvelet sparse regularization (A-CSR) is a stable and edge-preserving reconstruction method. These properties are inherited from the non-adapted curvelet sparse regularization, cf. Section 4.1. However, we have to remark that the edge-preservation applies only to those edges (singularities) with have visible directions $\xi \in W_\Phi$ at the angular range $[-\Phi, \Phi]$. Edges that have invisible directions $\xi \notin W_\Phi$ are smoothed, which is enforced by the assumption that the Fourier transform of the unknown function is supported near the wedge W_Φ. Actually, this smoothing property is also inherent in the non-adapted curvelet sparse regularization, as we have remarked in Subsection 4.1.3.
- Another important property of the A-CSR method is the "reduction of limited angle artifacts". To see this, recall that appearance of limited angle artifacts in reconstruction of the form $P_\Phi f = \mathcal{F}^{-1}(\chi_{W_\Phi} \hat{f})$ was a consequence of the hard truncation (in angular direction) in the Fourier transform domain, cf. Section 3.4. However, a function that is reconstructed via A-CSR has a smooth Fourier transform that is supported near W_Φ, cf. Figure 4.5. In particular, there is no hard truncation in angular direction. Hence, the A-CSR gives rise to an artifact-free reconstruction method. Note that a similar argumentation also shows that the non-adapted CSR already possesses this property.
- The A-CSR approach was first introduced in [Fri10], where the author combined microlocal analysis and curvelets in order to reduce the dimension of the reconstruction problem in the curvelet domain. To this end, the author used the "resolution of the wavefront set property" of continuous curvelet transform, [CD05a], in order to derive a qualitative characterization of visible curvelets. The rationale behind this approach is basically the same

as the one presented in Section 3.5. Namely, it aims at reconstructing that part of the unknown function which contains only the visible singularities. However, the approach of this section is more direct, since it is formulated with respect to the curvelet frame instead of the continuous curvelet transform. In particular, it applies more directly to the practical situation.

4.3 Characterization of curvelet sparse regularizations

In the last Section 4.2 we formulated an adapted curvelet sparse regularization. The basic idea behind this approach is to reconstruct only the visible curvelet coefficients at a given angular range. In contrast to the non-adapted CSR, the invisible curvelet coefficients are ignored and, thus, do not contribute to the reconstruction. It is therefore natural to ask how large the difference between CSR and A-CSR reconstruction is. In this section we are going to investigate the relation of curvelet sparse regularization (CSR) and its adapted version (A-CSR). To this end, we study the action of the limited angle Radon transform on curvelets and, in particular, derive a characterization of its kernel in terms of curvelets. Based on this characterization, we finally will show that reconstructions obtained via curvelet sparse regularization coincide with those obtained via A-CSR.

We recall that the entries of the system matrix for the discrete problem (4.23) were given by $\mathrm{K}_{m,n} = \mathcal{R}_\Phi \psi_n(\theta_m, s_m)$, where $1 \le m \le M$ and $1 \le n \le N$. By (4.27), the system matrix for the adapted problem (4.28) is chosen as a submatrix K_Φ of K, where only the columns with indices $n \in \mathcal{I}_\Phi$ are kept. It is therefore interesting to know, how large the entries $\mathrm{K}_{m,n}$ with $n \in \mathcal{I}_\Phi^{\text{invisible}}$ are. To this end, we are going to derive an exact formula for the Radon transform of curvelets. We first note an auxiliary result.

Lemma 4.6. *Let $f \in \mathcal{S}(\mathbb{R}^2)$ and $\xi = (\xi_1, \xi_2)^\intercal \in S^1$. Moreover, let $\xi^\perp = (-\xi_2, \xi_1)^\intercal$. Then,*

$$\int_{\mathbb{R}} f(t \cdot \xi)\, \mathrm{d}t = \int_{\mathbb{R}} \hat{f}(t \cdot \xi^\perp)\, \mathrm{d}t. \tag{4.30}$$

That is, integration in the spatial domain along a line through the origin corresponds to the integration along a perpendicular line through the origin in the frequency domain. ⌟

Proof. The identity (4.30) follows easily from Corollary 3.4. More specifically, to see (4.30) in

the case $\xi = (1, 0)$ we deduce the assertion as follows:

$$\begin{aligned}
\int_{\mathbb{R}} f(t \cdot \xi)\,\mathrm{d}t &= \int_{\mathbb{R}} f(x_1, 0)\,\mathrm{d}x_1 = \frac{1}{2\pi}\int_{\mathbb{R}}\int_{\mathbb{R}^2} \hat{f}(\xi) e^{ix_1\xi_1}\,\mathrm{d}\xi\,\mathrm{d}x_1 \\
&= \frac{1}{2\pi}\lim_{b\to\infty}\int_{-b}^{b}\int_{\mathbb{R}^2} \hat{f}(\xi) e^{ix_1\xi_1}\,\mathrm{d}\xi\,\mathrm{d}x_1 \\
&= \frac{1}{2\pi}\lim_{b\to\infty}\int_{\mathbb{R}^2} \hat{f}(\xi)\left(\int_{-b}^{b} e^{ix_1\xi_1}\,\mathrm{d}x_1\right)\mathrm{d}\xi \\
&= \lim_{b\to\infty}\int_{\mathbb{R}}\int_{\mathbb{R}} \hat{f}(\xi_1, \xi_2)\delta^b(\xi_1)\,\mathrm{d}\xi_1\,\mathrm{d}\xi_2 \\
&= \int_{\mathbb{R}}\left(\lim_{b\to\infty}\int_{\mathbb{R}} \hat{f}(\xi_1, \xi_2)\delta^b(\xi_1)\,\mathrm{d}\xi_1\right)\mathrm{d}\xi_2 \\
&= \int_{\mathbb{R}} \hat{f}(0, \xi_2)\,\mathrm{d}\xi_2 = \int_{\mathbb{R}} \hat{f}(t \cdot \xi^\perp)\,\mathrm{d}t.
\end{aligned}$$

Above, we have used the function δ^b which was defined in (3.7). Moreover, we note that the change of the integration order as well as the interchange of the limit process and integration are allowed due to Fubini's theorem and the dominated convergence theorem, respectively. The general case follows from an orthogonal change of variables. ∎

We are now able to derive an exact formula for the Radon transform of curvelets.

Theorem 4.7. *Let $\xi(\omega) = (\cos\omega, \sin\omega)^\intercal$, $\omega \in [-\pi, \pi)$. Then, for a curvelet $\psi_{j,l,k}$ (cf.* (4.12)*),*

$$\mathcal{R}\psi_{j,l,k}(\xi(\omega), s) = 2^{j/4} V\left(\frac{2^{\lceil j/2\rceil+1}}{\pi}(\omega + \theta_{j,l})\right)\sqrt{2\pi}\,\widehat{W}\left(2^j\left\langle b_k^{j,l}, \xi(\omega + \theta_{j,l})\right\rangle - 2^j s\right), \tag{4.31}$$

where $b_k^{j,l}$ and $\theta_{j,l}$ are defined in (4.14). ⌟

Proof. Let $\xi := \xi(\omega)$, and $\tau_p f := f(\cdot + p)$, $p \in \mathbb{R}^2$. Note that each curvelet $\psi_{j,l,k}$ is a Schwartz function, which is because its Fourier transform is C^∞ and compactly supported (per definition). Hence, we may apply Lemma 4.6 to get

$$\mathcal{R}_\Phi\psi_{j,l,k}(\xi, s) = \int_{\mathbb{R}} \psi_{j,l,k}(s\xi + t\xi^\perp)\,\mathrm{d}t = \int_{\mathbb{R}} (\tau_{s\xi}\psi_{j,l,k})(t\xi^\perp)\,\mathrm{d}t = \int_{\mathbb{R}} e^{i\langle s\xi, t\xi\rangle}\hat{\psi}_{j,l,k}(t\xi)\,\mathrm{d}t, \tag{4.32}$$

where in the last equation we have also applied (A.5).

According to (4.12), at scale 2^{-j}, each curvelet $\psi_{j,l,k}$ is defined via translation and rotation of a generating curvelet $\psi_{j,0,0}$. Using the relations (A.5) and (A.7) we further note that

$$\hat{\psi}_{j,l,k}(t\xi) = e^{-i\left\langle b_k^{j,l}, R_{\theta_{j,l}}(t\xi)\right\rangle}\hat{\psi}_{j,0,0}(R_{\theta_{j,l}}(t\xi)), \tag{4.33}$$

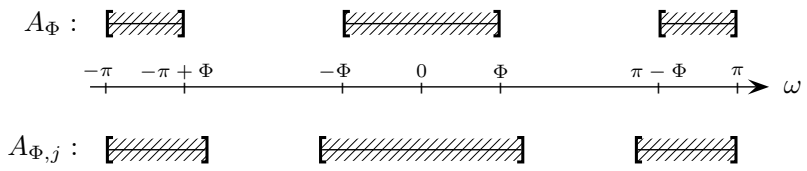

Figure 4.6: The symmetric (visible) angular range of the limited angle Radon transform, A_Φ, and its scale-dependent version, $A_{\Phi,j}$.

where $R_{\theta_{j,l}}$ is defined in (4.13). By substituting (4.33) into (4.32), we obtain

$$\begin{aligned}
\mathcal{R}_\Phi \psi_{j,l,k}(\xi, s) &= \int_{\mathbb{R}} e^{ist} e^{-i\left\langle b_k^{j,l}, R_{\theta_{j,l}}(t\xi)\right\rangle} \hat{\psi}_{j,0,0}(R_{\theta_{j,l}}(t\xi))\,\mathrm{d}t, \\
&= \int_{\mathbb{R}} e^{ist} e^{-it\left\langle b_k^{j,l}, \xi(\omega+\theta_{j,l})\right\rangle} \hat{\psi}_{j,0,0}(t, \omega+\theta_{j,l})\,\mathrm{d}t, \\
&= 2^{-3j/4} V\left(\frac{2^{\lceil j/2\rceil+1}}{\pi}(\omega+\theta_{j,l})\right) \int_{\mathbb{R}} e^{ist} e^{-it\left\langle b_k^{j,l}, \xi(\omega+\theta_{j,l})\right\rangle} W(2^{-j}t)\,\mathrm{d}t, \\
&= 2^{j/4} V\left(\frac{2^{\lceil j/2\rceil+1}}{\pi}(\omega+\theta_{j,l})\right) \int_{\mathbb{R}} e^{-ir[2^j\left\langle b_k^{j,l}, \xi(\omega+\theta_{j,l})\right\rangle - s]} W(r)\,\mathrm{d}r, \\
&= 2^{j/4} V\left(\frac{2^{\lceil j/2\rceil+1}}{\pi}(\omega+\theta_{j,l})\right) \sqrt{2\pi}\,\widehat{W}\left(2^j\left\langle b_k^{j,l}, \xi(\omega+\theta_{j,l})\right\rangle - 2^j s\right). \qquad \blacksquare
\end{aligned}$$

Theorem 4.7 provides an exact formula for the entries of the adapted as well as the non-adapted system matrix defined in (4.22) and (4.27), respectively. Moreover, it enables us to characterize the kernel of the limited angle Radon transform in terms of curvelets and, thus, to identify zero entries of the system matrix (4.22).

Theorem 4.8. *Let* $0 < \Phi < \pi/2$ *and denote* $\mathcal{I}_\Phi^{\text{invisible}}$ *the index set of invisible curvelet coefficients according to Definition 4.5. Then,*

$$\mathcal{R}_\Phi \psi_{j,l,k} \equiv 0 \quad \Leftrightarrow \quad (j,l,k) \in \mathcal{I}_\Phi^{\text{invisible}}. \tag{4.34}$$

⌟

Proof. To abbreviate the notation we let $a_j = \pi^{-1} 2^{\lceil j/2\rceil+1}$. Moreover, we define the symmetric (visible) angular range of the limited angle Radon transform $\mathcal{R}_\Phi$, cf. Figure 4.6, by

$$A_\Phi := [-\pi, -\pi+\Phi] \cup [-\Phi, \Phi] \cup [\pi-\Phi, \pi]$$

To prove the assertion, according to Theorem 4.7, we have to determine all curvelet directions $\theta_{j,l} \in [-\pi, \pi]$ such that $V(a_j(\cdot + \theta_{j,l}))|_{A_\Phi} \equiv 0$. To this end, recall that $\operatorname{supp} V \subseteq (-1, 1)$ (cf. Subsection 4.1.2), whence

$$\forall \omega \in A_\Phi :\ V(a_j(\omega+\theta_{j,l})) = 0 \quad \Leftrightarrow \quad \forall \omega \in A_\Phi :\ \theta_{j,l} \notin (-a_j^{-1} - \omega, a_j^{-1} - \omega)$$

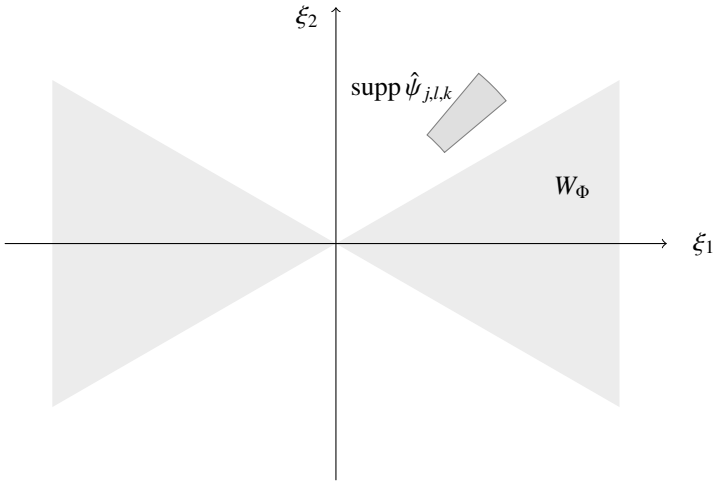

Figure 4.7: Theorem 4.8 states that a curvelet $\psi_{j,l,k}$ lies in the kernel of the limited angle Radon transform whenever the the support of $\widehat{\psi_{j,l,k}}$ lies outside the "visible wedge" $W_\Phi = \{r(\cos\eta, \sin\eta) : r \in \mathbb{R}, \eta \in [-\Phi, \Phi]\}$. That is, $\mathcal{R}_\Phi \psi_{j,l,k} \equiv 0$ whenever $\operatorname{supp} \hat{\psi}_{j,l,k} \cap W_\Phi = \emptyset$.

Therefore, by defining the scale-dependent version of A_Φ via (cf. Figure 4.6)

$$A_{\Phi,j} := [-\pi, -\pi + (\Phi + a_j^{-1})] \cup [-(\Phi + a_j^{-1}), \Phi + a_j^{-1}] \cup [\pi - (\Phi + a_j^{-1}), \pi],$$

we see that $V(a_j(\cdot + \theta_{j,l}))|_{A_\Phi} \equiv 0$ holds whenever $\theta_{j,l} \notin A_{\Phi,j}$. On the other hand, the condition $\theta_{j,l} \notin A_{\Phi,j}$ is equivalent to $\operatorname{supp} \hat{\psi}_{j,l,k} \cap W_\Phi = \emptyset$, which proves the assertion. ∎

Remark. The statement of Theorem 4.8 may be reformulated as follows:

$$\mathcal{R}_\Phi \psi_{j,l,k} \equiv 0 \quad \Leftrightarrow \quad \hat{\psi}_{j,l,k} \subseteq \mathbb{R}^2 \setminus W_\Phi.$$

That is, a curvelet $\psi_{j,l,k}$ lies in the kernel of the limited angle Radon transform iff the support of its Fourier transform does not intersect the wedge W_Φ, cf. Figure 4.7. This is in accordance with the Corollary 3.7, where we have shown that every $f \in \mathcal{S}(\mathbb{R}^2)$ with $\operatorname{supp} \hat{f} \subseteq W_\Phi$ lies in the kernel of $\mathcal{R}_\Phi$. As curvelets are directional, the Theorem 4.8 also confirms the observation of Section 3.2, where we noted that kernel functions of the limited angle Radon transform are directional, and that orientations determine whether a function belongs to the kernel of $\mathcal{R}_\Phi$ or not, cf. Figure 3.3.⌟

Theorem 4.8 shows that invisible curvelets (in the sense of Definition 4.5) are in fact invisible for the limited angle Radon transform. This observation justifies the nomenclature "invisible" in the context of curvelets, cf. Definition 4.5. An even more important fact for us is the identification of the zero-entries of the system matrix (4.22), namely

$$\mathrm{K}_{m,n} = 0$$

for all $1 \leq m \leq M$ and all $n = n(j,l,k)$ with $(j,l,k) \in \mathcal{I}_\Phi^{\text{invisible}}$. Correspondingly, the adapted system matrix (4.27) is formed by deleting all zero-columns of the non-adapted system matrix K.

In this sense, the adapted limited angle problem (4.28) is equivalent to the non-adapted problem (4.23).

Moreover, the fact that the adapted system matrix does not contain the zero-columns of the non-adapted system matrix shows that the condition number of the adapted system matrix improves and, in addition to the dimensionality reduction, stabilizes the limited angle problem.

In what follows, we shall show that the support of a CSR reconstruction, denoted by $c_{w,p}$, is indeed contained in the index set of visible curvelet coefficients, i.e.,

$$\operatorname{supp} c_{w,p} = \{(j,l,k) \in \mathcal{I}_N : \ (c_{w,p})_{j,l,k} \neq 0\} \subseteq \mathcal{I}_\Phi.$$

In order to prove this result we will need the notion of a subdifferential of a proper convex functional, [Roc70]: Let $F : H \to (-\infty, \infty]$ be a proper convex functional on a Hilbert space H, i.e. F takes values in $(-\infty, \infty]$, $F \not\equiv \infty$ and $F(\lambda x + (1-\lambda)y) \leq \lambda F(x) + (1-\lambda)F(y)$ for all $x, y \in H$ and all $0 < \lambda < 1$. An $x^* \in H$ is called *subgradient* of F at $x \in H$ if

$$F(y) \geq F(x) + \langle y - x, x^* \rangle, \qquad \text{for all } y \in H. \tag{4.35}$$

The set of all subgradients of F at $x \in H$ will be denoted by $\partial F(x)$, and is called the *subdifferential* of F at x. Before proceeding to the characterization of curvelet sparse regularizations, we note the following lemma.

Lemma 4.9. *Let $f : \ell^2(\mathcal{I}) \to [-\infty, \infty]$ be defined by $f(x) = \sum_{n\in\mathcal{I}} \varphi(x_n)$, where $\varphi : \mathbb{R} \to \mathbb{R}$ is a convex function such that f is proper. Then, it holds that*

$$y \in \partial f(x) \ \Leftrightarrow \ y_n \in \partial\varphi(x_n) \text{ for all } n \in \mathcal{I}. \tag{4.36}$$

⌟

Proof. Since f is proper, by the definition of a subgradient (4.35), we have $\partial f(x) = \emptyset$ if $f(x) = \infty$. We may therefore assume without loss of generality that $f(x) < \infty$. Now suppose that $y_n \in \partial\varphi(x_n)$ for all $n \in \mathcal{I}$. Then, by definition of the subgradient (4.35) we have

$$\forall z_n \in \mathbb{R} : \ \varphi(z_n) \geq \varphi(x_n) + y_n(z_n - x_n).$$

Summing over n implies

$$\forall z \in \ell^2(\mathcal{I}) : \ \sum_{n\in\mathcal{I}} \varphi(z_n) \geq \sum_{n\in\mathcal{I}} (\varphi(x_n) + y_n(z_n - x_n)) = \sum_{n\in\mathcal{I}} \varphi(x_n) + \langle y, z - x \rangle,$$

which is by definition of f equivalent to $y \in \partial f(x)$. This proves the implication "$\Leftarrow$" of the statement.

On the other hand, if $y \in \partial f(x)$, then $f(z) \geq f(x) + \langle y, z - x\rangle$ for all $z \in \ell^2(\mathcal{I})$. In particular, this holds for all $z = x + he_n$ with $h \in \mathbb{R}$ and $n \in \mathcal{I}$, where $e_n = (\delta_{i,n})_{i\in\mathcal{I}}$ and $\delta_{i,n}$ denotes the Kronecker delta. Therefore, we have

$$\begin{aligned}
\forall h \in \mathbb{R}\, \forall n \in \mathcal{I} : f(x + he_n) &\geq f(x) + \langle y, he_n\rangle \\
&\Leftrightarrow \ \sum_{i\in\mathcal{I}} \varphi(x_i + \delta_{i,n}h) - \sum_{i\in\mathcal{I}} \varphi(x_i) \geq y_n h \\
&\Leftrightarrow \ \varphi(x_n + h) - \varphi(x_n) \geq y_n h \\
&\Leftrightarrow \ y_n \in \partial\varphi(x_n).
\end{aligned}$$

∎

Finally, we are able to derive the announced characterization of CSR reconstructions at a limited angular range.

Theorem 4.10. *Let* $0 < \Phi < \pi/2$, $y^\delta \in \operatorname{ran}(\mathcal{R}_\Phi)$ *and let* $\mathcal{I}_\Phi^{\text{invisible}}$ *be defined by* (4.26). *Then, for each* $1 \le p \le 2$, *the minimizer*

$$c_{w,p} \in \operatorname*{arg\,min}_{c \in \mathbb{C}^N} \left\{ \frac{1}{2} \left\| \mathrm{K}c - y^\delta \right\|_{L^2(Z)}^2 + \|c\|_{w,p}^p \right\}$$

satisfies

$$(c_{w,p})_{j,l,k} = 0 \text{ for all } (j,k,l) \in \mathcal{I}_\Phi^{\text{invisible}}. \qquad \lrcorner$$

Proof. Since the Tikhonov functional $\mathcal{T}_{w,p}$ (cf. (4.8)) is a proper convex functional, each minimizer $\hat{c} \in \arg\min \mathcal{T}_{w,p}(c)$ is characterized by the the requirement, [Roc70],

$$0 \in \partial \mathcal{T}_{w,p}(\hat{c}) = K^*(K\hat{c} - y^\delta) + \partial \|\hat{c}\|_{w,p}^p$$

which is equivalent to

$$-K^*(K\hat{c} - y^\delta) \in \partial \|\hat{c}\|_{w,p}^p . \tag{4.37}$$

On the other hand, since $y^\delta \in \operatorname{ran}(\mathcal{R}_\Phi)$, we have $y^\delta = Kc^\delta = \mathcal{R}_\Phi T^* c^\delta$ for some curvelet coefficient vector $c^\delta \in \mathbb{C}^N$. Thus,

$$\hat{x} := -K^*(K\hat{c} - y^\delta) = -K^*K(\hat{c} - c^\delta) = -K^* \left(\sum_{j,l,k} (\hat{c} - c^\delta)_{j,l,k} \mathcal{R}_\Phi \psi_{j,l,k} \right).$$

By Theorem 4.8, we have

$$\hat{x}_{j,l,k} = 0 \text{ for all } (j,k,l) \in \mathcal{I}_\Phi^{\text{invisible}}. \tag{4.38}$$

To see that (4.38) already implies the assertion, let $(j,l,k) \in \mathcal{I}_\Phi^{\text{invisible}}$ and note that, by (4.37) and (4.38), the Lemma 4.9 implies that $0 \in \partial(w_{j,l,k} |\cdot|^p)(\hat{c}_{j,l,k})$. In turn, this means that $\hat{c}_{j,l,k}$ minimizes the function $f = w_{j,l,k} |\cdot|^p$. However, since $w_{j,l,k} > 0$, the only minimum of the function $f(x) = w_{j,l,k} |x|^p$ is $x = 0$ and therefore we get that $\hat{c}_{j,l,k} = 0$. ∎

Theorem 4.10 provides a mathematical justification for the adaption strategy that was presented in Section 4.2. It shows that only visible curvelet coefficients can be reconstructed by the CSR method and, consequently, that the A-CSR reconstructions coincide with the CSR reconstructions at a limited angular range. In particular, this shows that the adapted curvelet sparse regularization inherits all properties of the non-adapted CSR, such as edge-preservation.

4.4 Relation to biorthogonal curvelet decomposition (BCD) for the Radon transform

In this section we shall show that, if the data is available at a full angular range, a closed form formula can be derived for the curvelet sparse regularization (CSR). This formula is based on

the biorthogonal curvelet decomposition (BCD) for the Radon transform [CD02]. We will see that this formula is closely related to a curvelet thresholding approach that was also proposed in [CD00, CD02]. Eventually, we will discuss the application of the BCD approach to the case of limited angle tomography and interpret the curvelet sparse regularization as a natural generalization of the BCD reconstruction.

4.4.1 A closed form formula for CSR at a full angular range

We first briefly recall the definition of the BCD for the Radon transform. For details we refer to [CD02]. If not otherwise stated, we let $n = n(j,l,k) \in \mathcal{I}_N$ and denote the curvelet frame by $\{\psi_n\}$. In order to derive the BCD for the Radon transform a pair of frames $\{U_n\}$ and $\{V_n\}$ is constructed for $\operatorname{ran}(\mathcal{R}) \subseteq L^2(\mathbb{R}\times S^1)$ such that

$$\mathcal{R}\psi_n = 2^{-j}V_n, \quad \mathcal{R}^*U_n = 2^{-j}\psi_n,$$

and a quasi-biorthogonal relation $\langle V_n, U_{n'}\rangle_{L^2(Z)} = 2^{j-j'}\langle \psi_n, \psi_{n'}\rangle$ holds for all $n, n' \in \mathcal{I}_N$. In particular, there is a L^2-norm equivalence property

$$\sum_{n\in\mathcal{I}_N} \left|\langle g, U_n\rangle_{L^2(Z)}\right|^2 \asymp \|g\|^2_{L^2(Z)},$$

for all $g \in \operatorname{ran}(\mathcal{R})$. Similar relations hold for $\{V_n\}$. Using these notations, the BCD of the Radon transform is given by the following reproducing formula

$$f = \sum_{n\in\mathcal{I}_N} 2^j \langle \mathcal{R}f, U_n\rangle_{L^2(Z)}\,\psi_n, \tag{4.39}$$

where $f \in L^2(\mathbb{R}^2)$ is assumed to be a finite sum of curvelets $\{\psi_n\}$ [CD02]. Note that the curvelet coefficients of f are computed from the Radon transform data $\mathcal{R}f$.

We now use the above the frames (U_n), (V_n) and its relations with $\mathcal{R}$ and $\mathcal{R}^*$, respectively, to compute the minimizer of the ℓ^1-penalized Tikhonov functional. We assume that $y^\delta \in \operatorname{ran}(\mathcal{R})$, and denote $\langle\cdot,\cdot\rangle = \langle\cdot,\cdot\rangle_{L^2(\mathbb{R}^2)}$ as well as $[\cdot,\cdot] = \langle\cdot,\cdot\rangle_{L^2(Z)}$. Then, with $y^\delta_n = [y^\delta, U_n]$,

$$\begin{aligned}
\left\|\mathcal{R}f - y^\delta\right\|^2_{L^2(Z)} &\asymp \sum_{n\in\mathcal{I}_N} \left|[\mathcal{R}f - y^\delta, U_n]\right|^2 \\
&= \sum_{n\in\mathcal{I}_N} \left|[\mathcal{R}f, U_n] - [y^\delta, U_n]\right|^2 \\
&= \sum_{n\in\mathcal{I}_N} \left|\langle f, \mathcal{R}^*U_n\rangle - [y^\delta, U_n]\right|^2 \\
&= \sum_{n\in\mathcal{I}_N} \left|\left\langle f, 2^{-j}\psi_n\right\rangle - [y^\delta, U_n]\right|^2 \\
&= \sum_{n\in\mathcal{I}_N} \left|2^{-j}c_n - y^\delta_n\right|^2.
\end{aligned}$$

Using the definition of $\|\cdot\|_{w,p}^p$, we see that

$$\frac{1}{2}\left\|Kc - y^\delta\right\|_{L^2(Z)}^2 + \|c\|_{w,p}^p \asymp \frac{1}{2}\sum_{n\in\mathcal{I}_N}\left(\left|y_n^\delta - 2^{-j}c_n\right|^2 + \alpha w_n\,|c_n|^p\right),$$

where $K = \mathcal{R}T^*$ and T^* denotes again the synthesis operator with respect to the curvelet frame. We now assume that there is an $\alpha > 0$ such that

$$\begin{aligned} c_{w,p} &= \operatorname*{arg\,min}_{c\in\mathbb{C}^N}\left\{\frac{1}{2}\left\|Kc - y^\delta\right\|_{L^2(Z)}^2 + \|c\|_{w,p}^p\right\} \\ &= \operatorname*{arg\,min}_{c\in\mathbb{C}^N}\left\{\sum_{n\in\mathcal{I}_N}\left(\frac{1}{2}\left|2^{-j}c_n - y_n^\delta\right|^2 + \alpha w_n\,|c_n|^p\right)\right\}. \end{aligned} \tag{4.40}$$

Then, the functional (4.40) can be minimized by minimizing each term separately. Note that each term in (4.40) is of the form $\frac{1}{2}|ax-y|^2 + b|x|^p$ and that its minimum is given by $S^p_{b/a^2}(y/a)$, cf. [Lor04], where S^p_w is the thresholding operator defined in (4.7) with respect to the threshold $w = b/a^2$. Therefore, the regularized curvelet coefficients $\hat{c}$ are given by

$$\hat{c}_n = S^p_{2^{2j}\alpha w_n}(2^j y_n^\delta).$$

We summarize the results in the following theorem.

Theorem 4.11. *Assume that there is an $\alpha > 0$ satisfying* (4.40)*. Then, the solution of the full angular problem $y^\delta = \mathcal{R}f + \eta$ via curvelet sparse regularization is given by the (closed) formula*

$$f_{w,p} = \sum_{n\in\mathcal{I}_N} S^p_{2^{2j}\alpha w_n}(2^j y_n^\delta)\psi_n. \tag{4.41}$$

⌟

The relation between the reproducing formula (4.39) and (4.41) is now clear. Apparently, (4.41) reduces to (4.39) if the thresholding sequence satisfies $w \equiv 0$. On the other hand, if the data is corrupted by noise then the curvelet sparse regularized solution is simply a thresholded version of the BCD reproducing formula. The stabilizing character of the curvelet sparse regularization is reflected by the inherent thresholding of the curvelet coefficients (compare to (5.2)). Moreover, if the thresholding sequence $w = w(\delta)$ in (4.41) satisfies $w_n(\delta) \to 0$ as $\delta \to 0$, we see that the $f_{w(\delta),p} \to f$ as $\delta \to 0$, cf. Appendix C.3.

Remark. Note the ill-posed nature of the reproducing formula (4.39). This is evident because the coefficients $2^j\langle \mathcal{R}f, U_\mu\rangle_{L^2(Z)}$ corresponding to fine scales (large j) are amplified by the factor 2^j. Since noise is a fine scale phenomenon, there will be very large reconstruction errors when the data is corrupted by noise. ⌟

A closely related reconstruction technique was introduced in [CD02]. Starting form the BCD reproducing formula (4.39), the authors proposed to use soft-thresholding of curvelet coefficients with a scale dependent threshold τ_j, i.e.,

$$\hat{f} = \sum_{n\in\mathcal{I}_N} S_{\tau_j}\left(2^j\left\langle y^\delta, U_n\right\rangle_{L^2(\mathbb{R}\times S^1)}\right)\psi_n. \tag{4.42}$$

We see that this formula coincides with (4.41) for $p = 1$ and a suitably chosen thresholding sequence $\tau = (\tau_j)$.

4.4.2 CSR as a generalization of the BCD approach

In order to extend the above observation for curvelet sparse regularization (CSR) at a limited angular range tomography, a biorthogonal curvelet decomposition (BCD) for the limited angle Radon transform would be needed. To our knowledge there is no such BCD available for the limited angle Radon transform. Consequently, in the case of limited angle tomography, the CSR reconstruction (CSR) can not be expressed explicitly as it was done for the full angular range in (4.41). In particular, the BCD reconstruction of Candès and Donoho [CD02] can not be applied in this situation.

In contrast to the BCD approach, a reconstruction of the limited angle problem can be computed by the CSR method. Hence, curvelet sparse regularization can be understood as the natural generalization of the thresholded BCD reconstruction.

Curvelet sparse regularization offers even more flexibility compared to the BCD method. For example, the implementation of the thresholded BCD reconstruction is difficult for acquisition geometries which are different from the parallel-beam geometry. This is because the BCD method requires discretization of the functions U_n which live in the Radon domain. The implementation of the curvelet sparse regularization approach, however, does not rely on a specific acquisition geometry. One needs only to implement the system matrix. Moreover, the generalization to higher dimensions is also easier accessible via curvelet sparse regularization approach.

4.5 Summary and concluding remarks

The objective of this chapter was to design a reconstruction method for limited angle tomography that is stable, edge-preserving and adapted to the limited angular range. To address the first two issues, we have developed the method of curvelet sparse regularization (CSR) in Section 4.1. The idea behind this approach was to combine the regularization by sparsity, [DDDM04], [BL08a], [GHS08], [Lor09a], with the curvelet dictionary that is known to provide sparse and edge-preserving representations, [CD04]. In Section 4.2, we presented an adapted version of curvelet sparse regularization (A-CSR). The adaptivity was achieved by formulating the limited angle reconstruction problem with respect to an adaptively selected curvelet subdictionary, where the selection process was based on the stabilization strategy that we derived in Subsection 3.5.2. In this way, we could significantly reduce the dimension of the limited angle problem in the curvelet domain (depending on the angular range). In Section 4.3, a justification of the adaption procedure was given through a comprehensive mathematical analysis of the CSR approach. In particular, we presented a characterizations of the kernel of the limited angle Radon transform in terms of curvelets, and derived a precise characterization of CSR reconstructions. The last section of this chapter was devoted to the study of CSR reconstructions at a full angular range. In this case, we derived that explicit formula for CSR reconstruction by using the biorthogonal curvelet decomposition of the Radon transform, [CD02]. Finally, we have discussed that curvelet sparse regularization can be understood as natural generalization of the curvelet thresholding approach [CD00] to the limited angluar range.

We conclude this chapter with some further remarks.

The role of curvelets in the limited angle tomography. We would like to emphasize that, in this chapter, we have used curvelets for two different reasons. On the one hand, for the formulation of an adapted limited angle reconstruction problem in Section 4.2, cf. (4.28), and, on the other hand, for the developmen of a stable and edge-preserving reconstruction method. In order to adapt the problem to the limited angular range, we applied the stabilization strategy of Section 3.5 and performed a dimensionality reduction in the curvelet domain. So far, the adapted formulation was not related to any reconstruction algorithm (which is the reason why the adapted formulation can be interpreted as preconditioning procedure). For the development of a stable and edge-preserving reconstruction method, we exploited the ability of curvelets to provide sparse representations of functions with an optimal encoding of edges. In this context, curvelets seem to be optimally suited for the use in limited angle tomography.

General angular ranges. So far, all results of this chapter were formulated with respect to a symmetric angular range $[-\Phi, \Phi]$, where $0 < \Phi < \pi/2$. We would like to point out that this assumption is not restrictive. The results of Section 4.3 can be easily formulated for a general angular range $[\varphi_1, \varphi_2]$, $0 \leq \varphi_1 < \varphi_2 \leq \pi$. To this end, note that $[\varphi_1, \varphi_2] = [\varphi_0 - \Phi, \varphi_0 + \Phi]$ for some $\varphi_0 \in [0, \pi]$ and $0 < \Phi < \pi/2$. In this case, the corresponding wedge $W_{\Phi,\varphi_0} = R_{\varphi_0}(W_\Phi)$ is a rotation of W_Φ (cf. (3.5)) by the angle φ_0, where $R_{\varphi_0}(W_\Phi) = \{R_{\varphi_0}\xi : \xi \in W_\Phi\}$. Consequently, the statements of Theorem 4.8 and Theorem 4.10 are valid with the following definition of the index set of invisible curvelet coefficients,

$$\mathcal{I}_\Phi^{\text{invisible}} = \left\{(j,l,k) \in \mathcal{I}_N : \operatorname{supp} \hat{\psi}_{j,l,k} \cap W_{\Phi,\varphi_0} = \emptyset\right\},$$

Computation of the system matrix. In Theorem 4.7 we have derived an expression for the Radon transform of a curvelet $\psi_{j,l,k}$. This expression can be used to compute the entries of the system matrix K, cf. (4.22), analytically, if both, the angular window V and the Fourier transform of the radial window $\widehat{W}$ are known analytically. This is useful for practical application since, in this case, the system matrix can be precomputed and needs not to be set up in every iteration of the minimization of the ℓ^p-penalized Tikhonov functional.

The use of other directional multiscale dictionaries. We also would like to mention that our approach can be formulated with respect to other "curvelet-like" systems. An important example in this context are shearlets, see e.g. [LLKW05], [KL07], [ELL08], because they exhibit most of the properties of the curvelet dictionary. More precisely, shearlets are also highly directional, compactly supported in the Fourier domain, and they provide an optimally sparse representation of cartoon-like objects, [GL07]. Besides, there is also a biorthogonal shearlet decomposition of the Radon transform [CEGL10]. Accordingly, the results of this chapter can also be formulated with respect to the shearlet dictionary. The theorems and proofs can be adopted almost literally in this situation.

Generalization to 3D. Furthermore, we would like to note that the general idea of this chapter can be generalized to the three-dimensional setting. The results of this chapter carry over to this situation, even though, the analysis is more technical in this case. In order to do this, one has to work with the three-dimensional variant of the curvelet transform, [YDC05], or the shearlet transform, [DST09], [GL12], respectively.

Related work. The use of curvelets for edge-preserving tomographic reconstructions was firstly documented in [CD00, CD02, CG02]. These works develop a reconstruction strategy for the full angular tomographic problem that is based on the biorthogonal curvelet decomposition of the Radon transform. An analogical approach was formulated with respect to the shearlet dictionary in [CEGL10], [GL12]. For a detailed discussion of this approach and its relation to curvelet sparse regularization, we refer to Section 4.4. To our knowledge, the first method that exploits sparsity in the curvelet domain and is adapted to the limited angle geometry was presented in [Fri10]. In this work, the author combines the characterization of visible singularities, according to [Qui93], with the "the resolution of wavefront set property" of the continuous curvelet transform [CD05a] in order to get a characterization of visible curvelets. In this way, he derives an adapted curvelet sparse regularizaiton (A-CSR) that is closely related to our approach in Section 4.2. However, the results of [Fri10] are stated without proofs.

CHAPTER 5

Implementation of curvelet sparse regularization and numerical experiments

In the previous chapter, we theoretically developed the method of curvelet sparse regularization (CSR) and its adapted version (A-CSR) for limited angle tomography. We argued that this approach provides stable and edge-preserving reconstructions. In this chapter, we are concerned with the numerical implementation and performance analysis of CSR and A-CSR in a practical setting. To this end, we consider only the case $p = 1$, where CSR / A-CSR are obtained by minimizing the ℓ^1-penalized Tikhonov functional, cf. Section 4.1 and 4.2. In particular, it is our goal to show that the theoretical results of Chapter 4 directly translate into practice.

The present chapter is organized as follows. We start by giving the details of our implementation in Section 5.1 and proceed with the presentation of numerical experiments in Sections 5.2 and 5.3. These experiments are basically divided into two parts. The first part, presented in Section 5.2, is devoted to the illustration of the visibility of curvelets under the limited angle Radon transform. In particular, this experiment illustrates the result of Theorem 4.8 and justifies the dimensionality reduction that was applied in Section 4.2. In the second part of our experiments, we analyze the CSR and A-CSR reconstructions in terms of execution times, similarity and reconstruction quality, cf. Section 5.3. We show that a significant speedup can be achieved by using the adapted approach (A-CSR), while preserving the reconstruction quality of the CSR method. In both cases, the reconstructions are found to be superior to those obtained via filtered backprojection (FBP). In Section 5.4, we eventually adopt the artifact reduction strategy of Section 3.4 to the adapted curvelet sparse regularization and illustrate its performance in numerical experiments.

Essential parts of this chapter were published in [Fri12].

5.1 Implementation of curvelet sparse regularization

In what follows, we shall describe the implementation of the curvelet sparse regularization (CSR) and its adapted version (A-CSR) simultaneously. To this end, the symbol K will be used to denote the full system matrix K (cf. (4.22)) or the adapted system matrix K_Φ (cf. (4.27)), respectively,

i.e.,

$$K \in \{ \mathrm{K},\ \mathrm{K}_\Phi \}.$$

Moreover, in all of our experiments we are going to consider only the case $p = 1$, such that the computation of CSR and A-CSR reconstructions consists essentially in the minimization of the ℓ^1-penalized Tikhonov functional (4.8), i.e.,

$$c_w = \operatorname*{arg\,min}_{c \in \mathcal{I}_N} \left\{ \frac{1}{2} \left\| Kc - y^\delta \right\|^2_{L^2(Z)} + \|c\|_{1,w} \right\}, \tag{5.1}$$

where $w = (w_n)_{n \in \mathcal{I}_N}$ is a weight sequence satisfying $w_n \geq w_1 > 0$.

In order to formulate an explicit minimization procedure for (5.1), we first recall that the minimizer of the ℓ^1-penalized Tikhonov functional is characterized by the fixed point equation, cf. Proposition 4.1,

$$c_w = \mathcal{S}_{\gamma w} \left(c_w - \gamma K^* (K c_w - y^\delta) \right), \tag{5.2}$$

where $\mathcal{S}_{\gamma w}$ denotes the soft-thresholding operator

$$(\mathcal{S}_w(c))_n = \operatorname{sgn}(c_n) \max \{0, |c_n| - w_n\}.$$

A minimization algorithm for (5.1) can be now formulated by using a fixed point iteration of the above equation (5.2). Namely,

$$c^{n+1} = \mathcal{S}_{\tau^n} \left(c^n - s_n K^* (K c^n - y^\delta) \right). \tag{5.3}$$

Thus, the iteration (5.3) consists of a gradient descent step followed by a soft-thresholding with respect to the thresholding sequence $\tau = (\tau^n)$. It can be shown that this minimizaiton procedure, known under the name *iterated soft-thresholding*, converges to a minimizer of (5.1) provided that the step length s_n satisfies

$$0 < \underline{s} \leq s_n \leq \overline{s} < 2/\|K\|^2, \tag{5.4}$$

for all $n \in \mathbb{N}$, where $\underline{s}, \overline{s} > 0$, cf. [DDDM04], [BL08b].

For the purpose of this chapter, we implemented a variant of this soft-thresholding algorithm in Matlab. We now give the details of our implementation. We start by noting that, instead of computing the matrix K and storing it in the memory, we implemented the matrix-vector multiplications $c \mapsto Kc$ and $y \mapsto K^* y$ using the Matlab functions `radon` and `iradon`, respectively, together with the Matlab toolbox CurveLab version 2.1.2, [CDDY08], where in the adapted case, the index set of visible curvelet indices $\mathcal{I}_\Phi$ was precomputed according to Definition 4.5. For the implementation of the iterated soft-thresholding, we shall always use a constant step length $s_n = s$, $s > 0$, satisfying (5.4).

According to (5.2), the thresholding sequence $\tau = (\tau_{(j,l,k)})$ may depend on all curvelet parameters $(j, l, k) \in \mathcal{I}_N$ and is given by $\tau = sw$, where w denotes the ℓ^1-norm weight sequence w (cf. (5.1)) and s is the step length in (5.3). The thresholding sequence is a free parameter and has to be selected appropriately because it greatly influences the reconstruction quality. In general, there is no rule for choosing such a thresholding sequence τ. In our experiments, we are going to

apply basically two different choice rules for τ. First, we will set τ to be a constant sequence, i.e.,

$$\tau_{(j,l,k)} = \alpha, \tag{5.5}$$

where $\alpha > 0$. In this case, the value of α will be set manually for each reconstruction and is based on the visual inspection of the reconstruction quality. Second, the thresholding sequence $\tau = (\tau_{(j,l,k)})$ will be chosen adaptively and scale-dependent via

$$\tau_{(j,l,k)} = 2^{j-J}\sigma\sqrt{2\log_e N_{j,l}}, \tag{5.6}$$

where σ is the standard deviation of the noise η, $N_{j,l}$ denotes the number of curvelet coefficients at scale 2^{-j} and at orientation $\theta_{j,l}$, and $J \in \mathbb{N}$ is the largest available scale parameter for the image size of interest[1]. We note that this thresholding rule was adapted from [CD02, Sec. 6]. To mimic practical situations, we will assume throughout this chapter that the data $y^\delta = y + \eta$ is corrupted by an additive white Gaussian noise $\eta \in \mathcal{N}(0, \sigma^2)$, where the standard deviation σ is not known a priori. In order to automatize the reconstruction procedure, we will estimate σ as follows, cf. [Mal09, p. 565],

$$\sigma \approx 1.4826 \cdot \mathrm{MAD}(c_J^n). \tag{5.7}$$

Above, $\mathrm{MAD}(c_J^n)$ denotes the median of the absolute values of curvelet coefficients c_J^n corresponding to the finest scale 2^{-J} at iteration n. Finally, we would like to note that, as opposed to the first choice rule, the second choice rule yields a reconstruction procedure that is free of any parameter.

To complete the description of our algorithm we have to specify the choice of an initial guess c^0 for the iteration (5.3). To this end, note that, since the ℓ^1-penalized Tikhonov functional is convex, the iteration (5.3) always converges to a global minimizer. Therefore, the choice of an initial guess does not matter in theory. However, in practice it influences the speed of convergence. In all of our experiments we will make the following choices,

$$c^0 \in \{\, \mathbf{0},\ c_{\mathrm{FBP}} \,\}, \tag{5.8}$$

where $\mathbf{0}$ denotes the zero vector and c_{FBP} denotes the vector of curvelet coefficients of a filtered backprojection reconstruction. To obtain c_{FBP}, we first computed a FBP reconstruction f_{FBP} using the Matlab function `iradon` and, subsequently, applied the curvelet transform to the vector c_{FBP} of the CurveLab toolbox.

A summarized description of our reconstruction procedure is given in Algorithm 1.

5.2 Visibility of curvelets and dimensionality reduction

This section is devoted to the illustration of theoretical results that were presented in Section 4.3. In particular, we are going to investigate the visibility of curvelets under the limited angle Radon

Algorithm 1 Reconstruction algorithm

Require: Noisy data y^δ; Angular range $[-\Phi, \Phi]$; Image size $N \times N$;

$\mathcal{I}_\Phi \leftarrow$ visible index set at the angular range $[-\Phi, \Phi]$ according to (4.25);

$K \in \{\, \mathrm{K},\ \mathrm{K}_\Phi \,\}$ according to (4.22), (4.27);

$s \leftarrow$ step length, such that (5.4) is satisfied;

$c^0 \leftarrow$ initial guess according to (5.8);

$\tau_{(j,l,k)} \leftarrow$ thresholding sequence according to (5.5), or (5.6)+(5.7);

$n_{\max} \leftarrow$ maximum number of iterations;

$n \leftarrow 0$;

while $(n \leq n_{\max})$ **do**

    $c^n \leftarrow \mathcal{S}_{\tau^n}\left(c^n - sK^*(Kc^n - y^\delta)\right)$ with $\mathcal{S}_\tau$ defined in (5.1);

    $n \leftarrow \mathrm{n} + 1$;

end while

$f_{\mathrm{rec}} \leftarrow$ inverse curvelet transform of $c^{n_{\max}}$;

transform in a practical situation, and show how this leads to a dimensionality reduction in the limited angle reconstruction problem.

In order to illustrate the visibility of curvelets at different angular ranges $[-\Phi, \Phi]$ let us consider the function

$$f = \psi_1 + \psi_2 + \psi_3 + \psi_4, \tag{5.9}$$

where the curvelets ψ_i, $i \in \{1, 2, 3, 4\}$, are chosen at a fixed scale 2^{-4} with different orientations $\theta_1 = 0°$, $\theta_2 = 20°$, $\theta_3 = 60°$ and $\theta_4 = 90°$. For our experiment, we generated an image of the function (5.9) in Matlab by using the CurveLab toolbox, cf. Figure 5.1, and computed the limited angle Radon transform of this function as well as its inverse for two different angular ranges $[-\Phi, \Phi]$, namely $\Phi \in \{35°, 80°\}$, using the Matlab functions `radon` and `iradon`, respectively. Within the considered angular range the Radon transform was sampled equidistantly with a sampling distance $\Delta\theta = 1°$. The total number of measurements M_Φ was given by $M_{35°} = 51759$ and $M_{80°} = 117369$.

The results of this experiment are shown in Figure 5.2. The first column shows the limited angle Radon transforms $\mathcal{R}_\Phi f$ for $\Phi \in \{35°, 80°\}$, whereas the second column contains the corresponding inverse Radon transforms $\mathcal{R}_\Phi^{-1}\mathcal{R}_\Phi f$. In the first row of Figure 5.2 we can observe that only two curvelets are visible in the Radon transform domain. As a result, the corresponding reconstruction shows only two curvelets, namely those with orientations $\theta_1 = 0°$ and $\theta_2 = 20°$, i.e.,

$$\mathcal{R}_{35°}^{-1}\mathcal{R}_{35°} f = \psi_1 + \psi_2.$$

[1] For an image of size $N \times N$ the maximum scale parameter J was set to be $J = \lceil \log_2 N \rceil - 2$. This is according to the implementation of CurveLab version 2.1.2, [CDDY08].

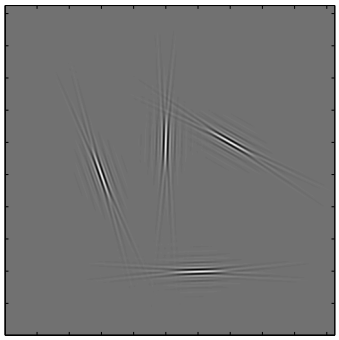

Figure 5.1: A Matlab generated 512×512 image of the function given in (5.9).

In the second row, we can observe a similar phenomenon. Namely, we can see that another curvelet becomes visible in the Radon transform domain. This curvelet also appears in the corresponding reconstruction in the second column, so that

$$\mathcal{R}_{80^\circ}^{-1}\mathcal{R}_{80^\circ} f = \psi_1 + \psi_2 + \psi_3.$$

To explain this effect let us compute the index set of visible curvelets $\mathcal{I}_\Phi$ according to (4.25). It is not hard to see that

$$\mathcal{I}_{35^\circ} = \{1, 2\} \text{ and } \mathcal{I}_{80^\circ} = \{1, 2, 3\}.$$

Consequently, our above observations imply that only visible curvelets appear in limited angle reconstructions $\mathcal{R}_\Phi^{-1}\mathcal{R}_\Phi f$. This is of course in accordance with Theorem 4.8. Thus, the numerical experiments confirm the result of Theorem 4.8.

Apparently, the above observation generalizes to a slightly more general situation, where a function f is given as finite linear combination of curvelets $f = \sum_{n\in\mathcal{I}} c_n\psi_n$. In this case, we can separate the visible and invisible parts of this function (from the angular range $[-\Phi, \Phi]$) as follows:

$$\begin{aligned} f &= \sum_{n\in\mathcal{I}_\Phi} c_n\psi_n + \sum_{n\in\mathcal{I}_\Phi^{\text{invisible}}} c_n\psi_n, \\ &= f_{\text{visible}} + f_{\text{invisible}}. \end{aligned}$$

Note that this separation depends only on the parameter Φ. According to Theorem 4.8 and the above observations, we have $\mathcal{R}_\Phi^{-1}\mathcal{R}_\Phi f = f_{\text{visible}}$. Accordingly, reconstructing a function f from limited angle data $y = \mathcal{R}_\Phi f$ amounts to determining only the visible curvelet coefficients at a given angular range. This is observation is in accordance with the adaption strategy of Section 4.2, where an adapted limited angle problem was derived (cf. (4.28)). We see that the dimension of the problem in the curvelet domain may be reduced by the number of invisible curvelets $|\mathcal{I}_\Phi^{\text{invisible}}|$.

We finally investigate the degree of dimensionality reduction in a practical situation. To this end, we computed the dimension of the adapted problem, $d(\Phi) := |\mathcal{I}_\Phi|$, for various values of Φ.[2] The plot of $d(\Phi)$ is shown in Figure 5.3 for an image of size 256×256. We can observe that

[2]Note that the dimension $|\mathcal{I}_N|$ of the reconstruction problem depends on the size of the considered image f.

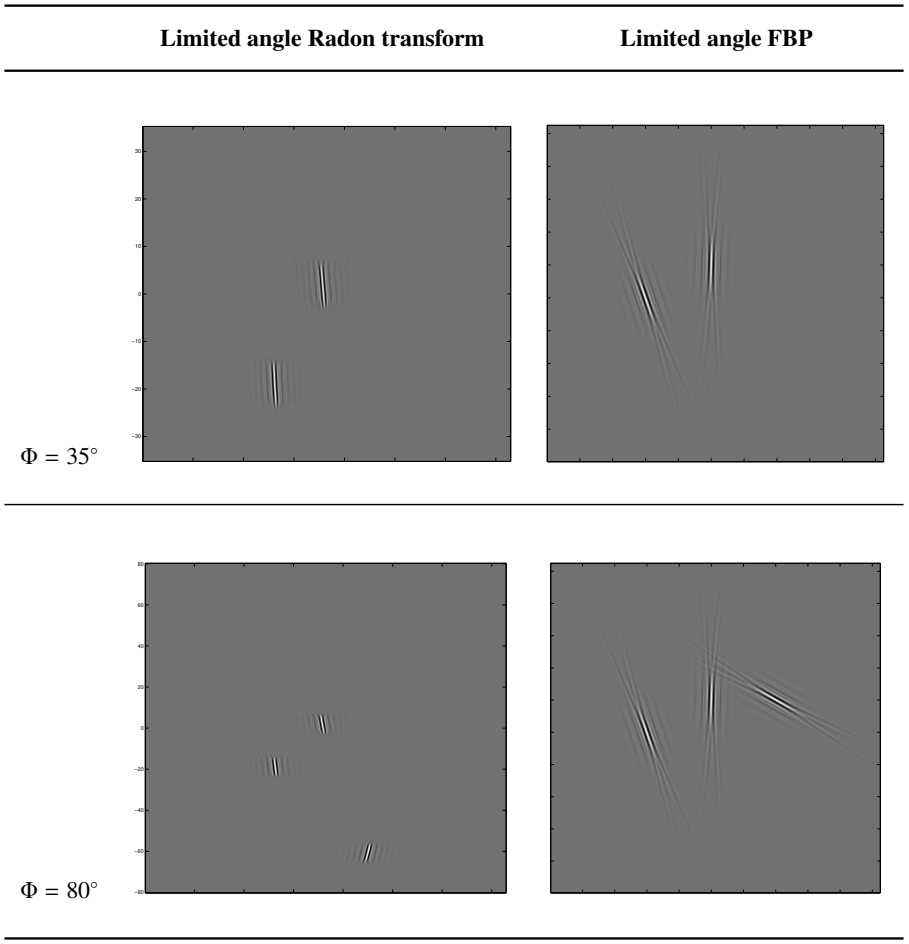

Figure 5.2: Limited angle Radon transform $\mathcal{R}_\Phi f$ and the corresponding reconstructions $\mathcal{R}_\Phi^{-1}\mathcal{R}_\Phi f$ of the function given in (5.9) (cf. Figure 5.1) at an angular range $[-\Phi, \Phi]$, $\Phi \in \{35°, 80°\}$, and an angular sampling distance $\Delta\Phi = 1°$. Observe that, for $\Phi = 35°$ (first row), the only visible curvelets are those with orientations $\theta_1 = 0°$ and $\theta_2 = 20°$. However, after enlarging the angular range to $\Phi = 80°$ (second row) another curvelet with orientation $\theta_3 = 60°$ becomes visible.

the graph of $d(\Phi)$ exhibits the expected behavior: The dimension of the non-adapted problem in the curvelet domain is constant for all angular ranges. This is of course due to the fact that the non-adapted problem is formulated with respect to all curvelet coefficients. Hence, it is independent of Φ. However, the dimension of the adapted problem shows a strong dependence on the available angular range. We can observe a significant dimensionality reduction for any angular range parameter satisfying $\Phi \leq 153°$. Moreover, the reduced dimension $d(\Phi)$ seems to exhibit a piecewise constant behavior. The values of $d(\Phi)$ increase stepwise linearly as the angular range increases. The reason for this stepwise structure lies in the fact that curvelets remain visible as long as $\operatorname{supp} \hat{\psi}_{j,l,k} \cap W_\Phi \neq \emptyset$, see also Figure 4.7. The length of one such step therefore corresponds to the length of the of the support of the angular window V of curvelets at the finest scale 2^{-J}, i.e., to $\left|\operatorname{supp} V(2^{\lceil J/2 \rceil + 1} \cdot /\pi)\right|$.

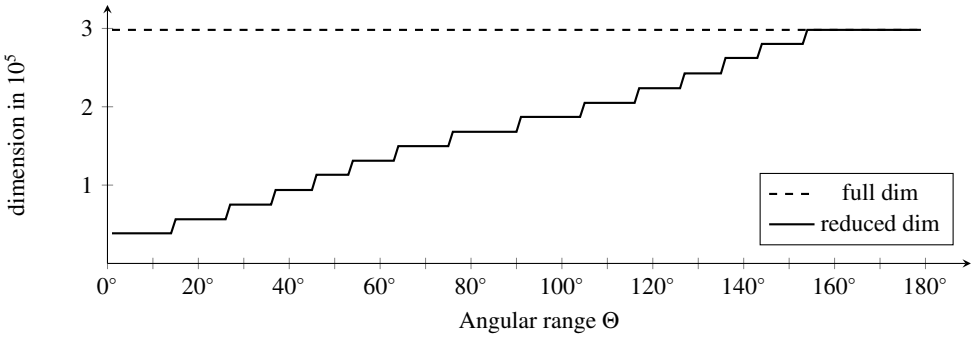

Figure 5.3: Dimension of the full problem (4.23), - - - , and of the adapted problem (4.28), ——, for an image of size 256×256. The plot shows the dependence of the full and reduced dimension on the available angular range $[0, \Theta]$. Because the full problem is formulated in terms of all curvelet coefficients, its dimension is constant for all angular ranges. The adapted problem, however, is formulated only in terms of visible curvelet coefficients. Hence, the reduced dimension depends strongly on the available angular range.

5.3 Execution times and reconstruction quality

In the following experiments we are going to investigate execution times and the reconstruction quality of CSR and A-CSR reconstructions at a limited angular range. We will also compare the reconstruction quality of CSR and A-CSR reconstructions to those reconstructions obtained via filtered backprojection.

5.3.1 Experimental setup

In order to minimize the influence of specific image features, we have used three different types of images for our experiments. These images are shown in Figure 5.4. We note that all of the following computations were done in Matlab. The generation of the limited angle Radon transform data $y = \mathcal{R}_\Phi f$ was done by the function `radon` of the Matlab Image Processing Toolbox.

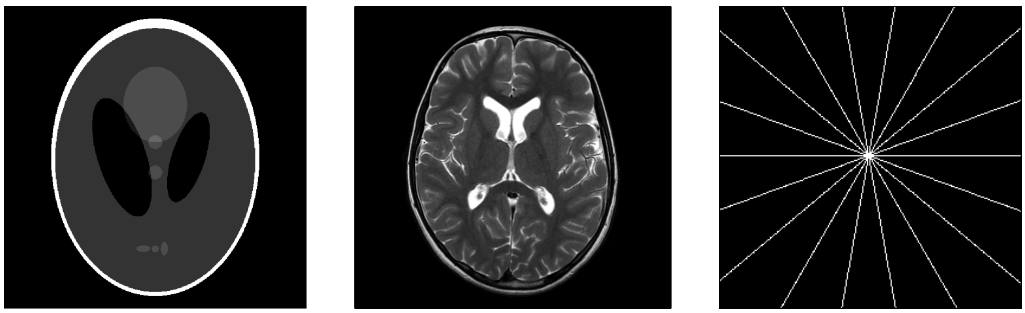

(a) Shepp-Logan head phantom **(b)** Brainstem [Bra10] **(c)** Radial pattern

Figure 5.4: Original images.

To mimic practical conditions, the generated data was corrupted by an additive white Gaussian noise, which was generated by the Matlab function `randn`, i.e., $y^\delta = \mathcal{R}_\Phi f + \eta$ with $\eta \in \mathcal{N}(0, \sigma^2)$ and $\sigma = 0.02 \cdot (\max \mathcal{R}_\Phi f - \min \mathcal{R}_\Phi f)$ (noise level = 2%). The total number of measurements $y^\delta \in \mathbb{R}^M$ was given by $M = L_\Phi \cdot \lceil \sqrt{2} \cdot (N+2) \rceil$, where L_Φ is the number of angles and $N \times N$ denotes the size of the image f. In all of our experiments, the angular sampling distance was set to $\Delta\Theta = 1°$ and, hence, $L_\Phi = 2\Phi + 1$ if the angular range is given by $[-\Phi, \Phi]$ and $L_\Phi = \Phi + 1$ if the angular range is $[0, \Phi]$. The corresponding noisy limited angle data sets y^δ are depicted in Figure 5.6. Given these noisy data sets, we computed CSR, A-CSR and filtered backprojection (FBP) reconstructions at various angular ranges. For the computation of CSR and A-CSR reconstructions, we have used the Algorithm 1, whereas FBP reconstructions were computed using the Matlab function `iradon` of the Image Processing Toolbox. The resulting reconstructions are presented in Figures 5.7, 5.8 and 5.9.

5.3.2 Execution times

We start by examining the execution times of the curvelet sparse regularization (CSR) and its adapted version A-CSR. For this purpose, we computed several CSR and A-CSR reconstructions of the Shepp-Logan head phantom of size 256×256 at different angular ranges $[0, \Theta]$. This experiment was repeated for two different numbers of iterations in the Algorithm 1. In both cases, the angular range parameter Θ was chosen to vary between 1° and 180° (with an angular increment $\Delta\Theta = 1°$). The results of these tests are plotted in Figure 5.5, where the dashed lines (- - -) indicate the execution times of the CSR reconstructions, and the solid lines (——) show the execution times of the adapted approach A-CSR. The plots in Figure 5.5(a) and (b) show that the dependence of the execution times on the available angular range exhibits an linear behavior. In both cases, the adapted procedure shows a significant speedup, especially, for small angular range parameters $\Theta \leq 120°$. This behavior is of course a consequence of the dimensionality reduction and its dependence on the angular range, cf. Figure 5.3.

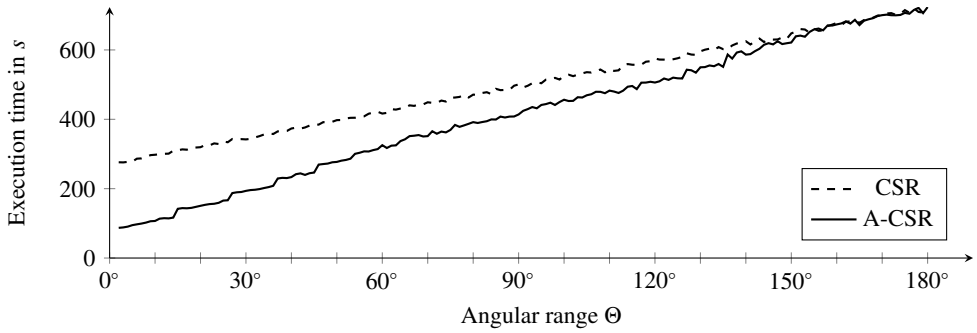

(a) 100 Iterations

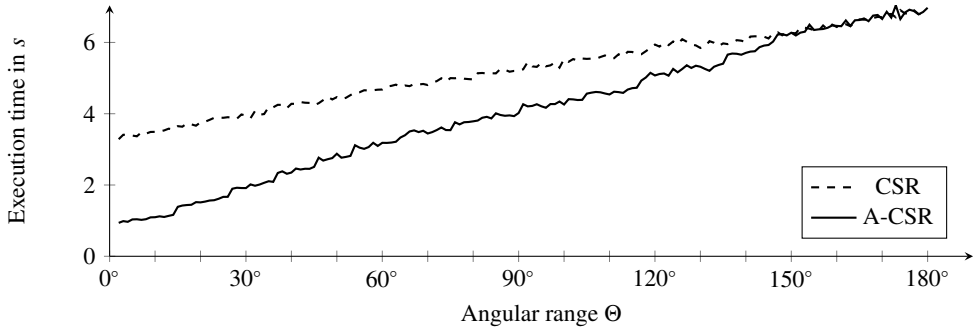

(b) 2 Iterations

Figure 5.5: Reconstruction of the Shepp-Logan head phantom of size 256×256 (Figure 5.4(a)) at different angular ranges $[0, \Theta]$, $\Theta \in \{1°, \ldots, 180°\}$. The plots show the execution times for CSR and A-CSR reconstruction using 100 iterations (a) and 2 iterations (b) of Algorithm 1. In both cases a significant speedup of the reconstruction procedure A-CSR can be observed.

5.3.3 Reconstruction quality

In order to evaluate the reconstruction quality of our method, we performed reconstructions at two different limited angular ranges, namely $[-45°, 45°]$ and $[-80°, 80°]$, using the methods CSR, A-CSR and FBP. For each computation of CSR and A-CSR reconstruction, we have used an individual set of parameters in Algorithm 1. These parameter sets differ in the number of iterations $n_{\max}$, the initial guess c^0 and the thresholding sequence τ (cf. Section 5.1). FBP reconstructions were computed using the Matlab's function `iradon` with its default parameters. The resulting reconstructions are show in Figures 5.7, 5.8 and 5.9, where the exact values of the reconstruction parameters are listed in the captions. Each of these figures shows a matrix of images, which is organized as follows: The upper half of the matrix contains images that were reconstructed at the angular range $[-45°, 45°]$, whereas the lower half shows reconstructions at the angular range $[-80°, 80°]$. Moreover, each row of the image matrices contains only those CSR and A-CSR reconstructions that were generated using the same parameter set for the Algorithm 1. The original images can be viewed in Figure 5.4.

The goal of this experiment is twofold: On the one hand, we want to illustrate the similarity of CSR and A-CSR reconstructions and, on the other hand, to compare the reconstruction quality of CSR / A-CSR reconstructions to those obtained via FBP.

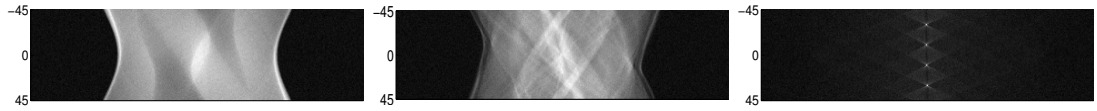

(a) Angular range $[-45°, 45°]$

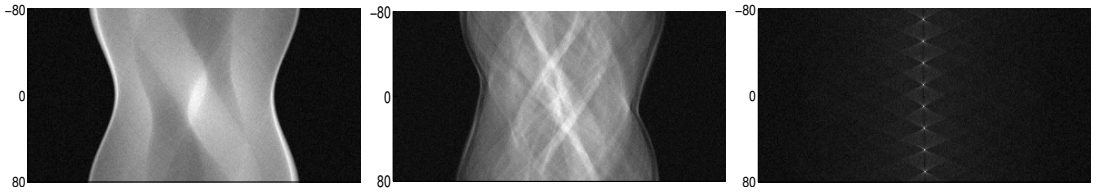

(b) Angular range $[-80°, 80°]$

Figure 5.6: Noisy Radon transforms at a noise level of 2%: Shepp-Logan head phantom (left), brainstem (middle) and radial pattern (right), cf. Figure 5.4.

Similarity of CSR and A-CSR reconstructions. Let's have a look at the CSR / A-CSR reconstructions in Figures 5.7, 5.8 and 5.9. We compare the reconstructed images that are located within the same row because these reconstructions were generated using the same parameter set. We first note that, by visually inspecting the images, no difference in reconstruction quality can be observed. That is, the CSR and A-CSR reconstruction look visually identical, for which reason we conclude that curvelet sparse regularization and its adapted version produce reconstructions of the same visual quality when the same parameters are used in Algorithm 1. To make this observation independent of visual perception, we computed the discrepancy between the CSR reconstruction f_{CSR} and the A-CSR reconstruction $f_{\mathrm{A-CSR}}$ with respect to the mean squared error (MSE),

$$\mathrm{MSE}(f_{\mathrm{CSR}}, f_{\mathrm{A-CSR}}) = \frac{1}{N^2} \sum_{n,m=1}^{N} \left| f_{\mathrm{CSR}}[n,m] - f_{\mathrm{A-CSR}}[n,m] \right|^2, \tag{5.10}$$

where $N \in \mathbb{N}$ corresponds to the size $N \times N$ of the reconstructed images. This quantity gives the average difference between gray values of the CSR and A-CSR reconstructions. The MSE values, corresponding to reconstructions in Figures s5.7, 5.8 and 5.9, are given in Table 5.1. Observe that these values vary in the range from 10^{-4} to 10^{-6}. Since the gray values of the original images (cf. Figure 5.4) lie between 0 and 1, these MSE values indicate that the average difference between the gray values of the CSR and A-CSR reconstructions is rather small. Thus, this quantitative comparison confirms the visual impression, namely that the CSR and A-CSR reconstructions are of a similar quality.

However, since MSE values are not equal to zero, there is a difference between CSR and A-CSR reconstructions, depending on the angular range and the particular image. In Table 5.1, the MSE values at a large angular range are slightly smaller than those at a small angular range. This phenomenon may be explained as follows: The reconstructed sequence of curvelet coefficients c^{CSR} contains visible and invisible components. However, the invisible part of this vector might be not zero after a finite number of iterations and, hence, create a contribution to the MSE values. Since there are more invisible curvelet coefficients at a small angular range, this contribution is larger than in the case of a large angular range. Another source for differences in CSR and A-CSR reconstructions is the estimation of the standard deviation via (5.7). This is due to the

	Shepp-Logan head phantom		**Brainstem**		**Radial pattern**	
	constant	adaptive	constant	adaptive	constant	adaptive
$\Phi = 45°$	$2.89 \cdot 10^{-5}$	$6.72 \cdot 10^{-5}$	$6.37 \cdot 10^{-4}$	$3.04 \cdot 10^{-4}$	$4.03 \cdot 10^{-4}$	$4.17 \cdot 10^{-4}$
$\Phi = 80°$	$4.78 \cdot 10^{-6}$	$1.02 \cdot 10^{-5}$	$1.09 \cdot 10^{-6}$	$2.07 \cdot 10^{-5}$	$7.89 \cdot 10^{-5}$	$9.08 \cdot 10^{-5}$

Table 5.1: The $\mathrm{MSE}(f_{\mathrm{CSR}}, f_{\mathrm{A-CSR}})$ values (cf. (5.10)) corresponding to reconstructions in Figures 5.7, 5.8 and 5.9. Each row contains values corresponding to the reconstructions from the angular range $[-\Phi, \Phi]$. The columns with the label "constant" contain MSE values that correspond to those CSR / A-CSR reconstructions that were generated by using a constant thresholding sequence (5.5), whereas the column "adaptive" contains the values where an adaptive threshold (5.6) was used. Small values indicate similarity of reconstructions f_{CSR} and $f_{\mathrm{A-CSR}}$.

fact that the median of absolute values of all curvelet coefficients might be different from the median of absolute values of the visible curvelet coefficients. The difference in this estimation procedure is again bigger in the case of a small angular range than in the case of a large angular range. Of course, the latter explanation applies only if the generic thresholding rule (5.6) is used in Algorithm 1. As a result, the MSE values are usually larger in this case.

Reconstruction quality. Eventually, we compare the reconstruction quality of CSR / A-CSR reconstructions to the quality of filtered backprojection reconstruction. In what follows, we shall not distinguish between CSR and A-CSR reconstructions, because their similarity was already observed above. We again start by visually inspecting the reconstructions in Figures 5.7, 5.8 and 5.9. First of all, we observe that the FBP reconstructions contain more noise than reconstructions obtained via curvelet sparse regularization. The visual quality of FBP reconstructions seems to be poor and inferior to the CSR reconstructions. This is particularly evident for reconstructions that were obtained at the angular range $[-80°, 80°]$. On the other hand, the visual impression of curvelet sparse regularizations in the Figures 5.7, 5.8 and 5.9 is better than that of FBP reconstructions. In particular, the CSR / A-CSR reconstructions appear significantly less noisy than the FBP reconstructions. Besides the better noise performance of CSR reconstructions, we also observe that all details are well preserved and that the edges are clearly visible. These conclusions apply to all parameter sets that we used for generating CSR and A-CSR reconstructions.

To verify our visual impression, we have computed the peak signal-to-noise-ratio (PSNR),

$$\mathrm{PSNR}(f_{\mathrm{rec}}) = 10 \cdot \log\left(\frac{1}{\mathrm{MSE}(f, f_{\mathrm{rec}})}\right),$$

for all reconstructions $f_{\mathrm{rec}} \in \{ f_{\mathrm{FBP}}, f_{\mathrm{CSR}}, f_{\mathrm{A-CSR}} \}$ with respect to the original images f, cf. Figure 5.4. The PSNR is a quality measure that is expressed on a logarithmic scale, and where large values indicate a good reconstruction quality. The values corresponding to reconstructions in Figures 5.7, 5.8 and 5.9 are listed in Table 5.2. Note that the PSNR values of curvelet sparse regularizations (CSR as well as A-CSR) are considerably larger than those of the FBP reconstruc-

	Shepp-Logan head phantom			**Brainstem**			**Radial pattern**		
	CSR	A-CSR	FBP	CSR	A-CSR	FBP	CSR	A-CSR	FBP
	18.0736	18.1281	13.8553	18.8445	18.8523	12.6658	15.6230	15.5148	10.8178
$\Phi = 45°$	16.2103	16.1676	13.8553	16.3861	16.1246	12.6658	15.5850	15.5017	10.8178
	22.2812	22.3060	20.5724	21.0306	21.0319	17.5463	16.8074	16.8429	12.7346
$\Phi = 80°$	22.0945	22.1058	20.5724	22.5522	22.5906	17.5463	16.8025	16.8587	12.7346

Table 5.2: PSNR values corresponding to reconstructions in Figures 5.7, 5.8 and 5.9. The upper half contains PSNR values of reconstructions at the angular range $[-\Phi, \Phi]$, where $\Phi = 45°$. Whereas, the lower half contains PSNR values of reconstructions corresponding to $\Phi = 80°$. For each angular range parameter $\Phi \in \{45°, 80°\}$, there are two rows of PSNR values. The PSNR values of CSR / A-CSR reconstructions that are located in the first row correspond to the *parameter set 1*, whereas the PSNR values of CSR / A-CSR reconstructions that are located in the second row correspond to the *parameter set 2*.

tions, independently of test image and angular range. As a result, the PSNR values indicate that the image quality of CSR / A-CSR reconstructions is considerably better that of FBP reconstructions. This conclusion applies to every parameter set that we have used in the computation of CSR and A-CSR reconstructions. Once again, our visual impression is confirmed by the values of an objective quality measure.

Finally, we would like to comment on the differences of CSR / A-CSR reconstructions when using different parameter sets. To this end, we first remark that essentially two parameter sets were used for the CSR / A-CSR reconstructions. The characteristics of these parameter sets are as follows: On the one hand, *parameter set 1* consists of a large number of iterations $n_{\max}$, a constant thresholding sequence (5.5) together with a relatively poor initial guess $c^0 = 0$. Reconstructions that were computed with such a parameter set are located in rows 1 and 3 of Figures 5.7, 5.8 and 5.9, whereas the corresponding PSNR values are given in rows 1 and 3 of Table 5.2. On the other hand, the *parameter set 2* consists of only a small number of iterations, an adaptive thresholding sequence (5.6), and a quite good initial guess $c^0 = c_{\text{FBP}}$. These reconstructions are located in rows 2 and 4 of Figures 5.7, 5.8 and 5.9 and corresponding PSNR values are listed in rows 2 and 4 of Table 5.2. By visually inspecting the reconstructions, we first of all observe that the use of different parameter sets results in different quality characteristics of curvelet sparse regularizations. However, in this case it is difficult to compare the quality of reconstructions on a visual basis. Comparing the PSNR values in Table 5.2, we observe that *parameter set 1* leads to a slightly better reconstruction quality for the Shepp-Logan head phantom and for the brainstem image at the angular range $[-45°, 45°]$. In other cases, the PSNR values seem to be comparable. Nevertheless, there is an advantage in using the *parameter set 2*, which stems from the fact that the resulting algorithm is free of any parameters. This is because the thresholding sequence is chosen automatically for each reconstruction, cf. (5.6), and, thus, has not to be determined in a series of experiments. In addition, this choice results in a faster computation which is due to the

better initial estimate $c^0 = c_{\mathrm{FBP}}$.

5.4 Artifact reduction in curvelet sparse regularizations

At the end of Section 4.2, we have remarked that curvelet sparse regularization (CSR) and its adapted version (A-CSR) give rise to artifact-free reconstruction methods. In order to investigate whether this statement applies to practical CSR / A-CSR reconstructions, let us take a look at the limited angle reconstructions that are presented in Figures 5.7 and 5.8. Here, it is easy to observe that reconstructions of the Shepp-Logan head phantom as well as reconstructions of the brainstem image contain streak artifacts. The artifacts are particularly evident in reconstructions from the smaller angular range $[-45°, 45°]$. Apparently, these artifacts are a consequence of the limited angular range, and can be explained analogously to Section 3.4. Namely, at the angular range $[-\Phi, \Phi]$, the artifacts appear along straight lines which are tangent to singularities $(x, \xi_\Phi) \in \mathrm{WF}(f)$ of the original object f, where $\xi_{\pm\Phi} = (\cos(\pm\Phi), \sin(\pm\Phi))^\intercal$. This is in accordance with Theorem 3.24. Note that no limited angle artifacts are visible in reconstructions that are shown in Figure 5.9. This is due to the fact that the original image, cf. Figure 5.4(c), does not contain singularities $(x, \xi_{\pm\Phi})$ for $\Phi \in \{45°, 80°\}$.

In order to reduce the production of the limited angle artifacts, we applied the artifact reduction strategy of Subection 3.4.2 to the adapted curvelet sparse regularization. For this purpose, we modified the definition of the adapted system matrix (4.27) according to

$$(\mathrm{K}_{\kappa\Phi})_{m,n} = \kappa_\Phi(\theta_m) \cdot \mathcal{R}_\Phi \psi_n(\theta_m, s_m), \quad 1 \le m \le M,\ 1 \le n \le N_\Phi, \tag{5.11}$$

where $\kappa_\Phi = \kappa_{\Phi,\varepsilon}$ is a smooth truncation function defined in (3.45), and used Algorithm 1 together with the matrix $\mathrm{K}_{\kappa\Phi}$ to compute artifact reduced A-CSR reconstructions. The resulting reconstructions for $\Phi = 45°$ and $\varepsilon = 35°$ are shown in Figure 5.10. Here, we can observe that the artifacts, that were present in Figures 5.7 and 5.8, are clearly reduced. However, we can also observe that singularities $(x, \xi) \in \mathrm{WF}(f)$ with directions ξ close to $\xi_{\pm\Phi} = (\cos(\pm\Phi), \sin(\pm\Phi))^\intercal$ were smoothed.

Remark. Basically, the artifact reduction strategy (5.11) consists in solving a modified limited angle problem rather than the original one. This modified problem is given by

$$y^\delta = \mathcal{K}_\Phi \mathcal{R}_\Phi y + \eta,$$

where the operator $\mathcal{K}_\Phi \mathcal{R}_\Phi$ is defined by $\mathcal{K}_\Phi \mathcal{R}_\Phi f(\theta, s) = \kappa_\Phi(\theta) \cdot \mathcal{R}_\Phi f(\theta, s)$, cf. Theorem 3.26. ⌟

5.5 Summary and concluding remarks

The main part of this chapter was devoted to the numerical analysis of curvelet sparse regularization (CSR) and its adapted version (A-CSR). In particular, our goal was to demonstrate the practical relevance of these methods. For this purpose, we implemented the CSR / A-CSR approach

in Matlab, cf. Section 5.1, and investigated its performance in a series of numerical experiments. In our first experiment, we illustrated the visibility of curvelets in practical reconstructions, cf. Section 5.2. We found that the theoretical result of Theorem 4.8 directly translates into practice, and consequently justifies the dimensionality reduction in the adapted approach, cf. Section 4.2. In the second part of our experiments, we investigated the execution times and the quality of CSR and A-CSR reconstructions. The experiments in Section 5.3 showed that A-CSR produces reconstructions that are of the same quality as CSR reconstructions. This observation is in accordance with the Theorem 4.10. Moreover, our experiments confirmed that the adapted curvelet sparse regularization is stable and edge-preserving with respect to visible edges. The reconstruction quality is controlled by the number of iterations, the choice of the initial guess and the thresholding sequence. However, we observed that the thresholding sequence had the most crucial impact on the reconstruction quality. According to that, the choice of this sequence should be made carefully and individually for each reconstruction problem. In practice, this is often done by trial and error. To overcome this, we introduced an adaptive thresholding rule in Section 5.1, and found that this procedure leads to good quality reconstructions. In addition to that, the resulting reconstruction algorithm is free of any parameter. In the final Section 5.4, we noted that the limited angle artifacts are still present in CSR / A-CSR reconstructions and presented an artifact reduction approach for curvelet sparse regularization.

Finally, we would like to point out that the minimization algorithm (Algorithm 1) that we used to implement the curvelet sparse regularization is known to be slow, [BL08b], [Lor09b]. In addition to that, our Matlab implementation is very rudimentary. Accordingly, the execution times that are presented in Figure 5.5 may be improved by a more elaborate implementation of Algorithm 1 or by using a more sophisticated minimization procedure.

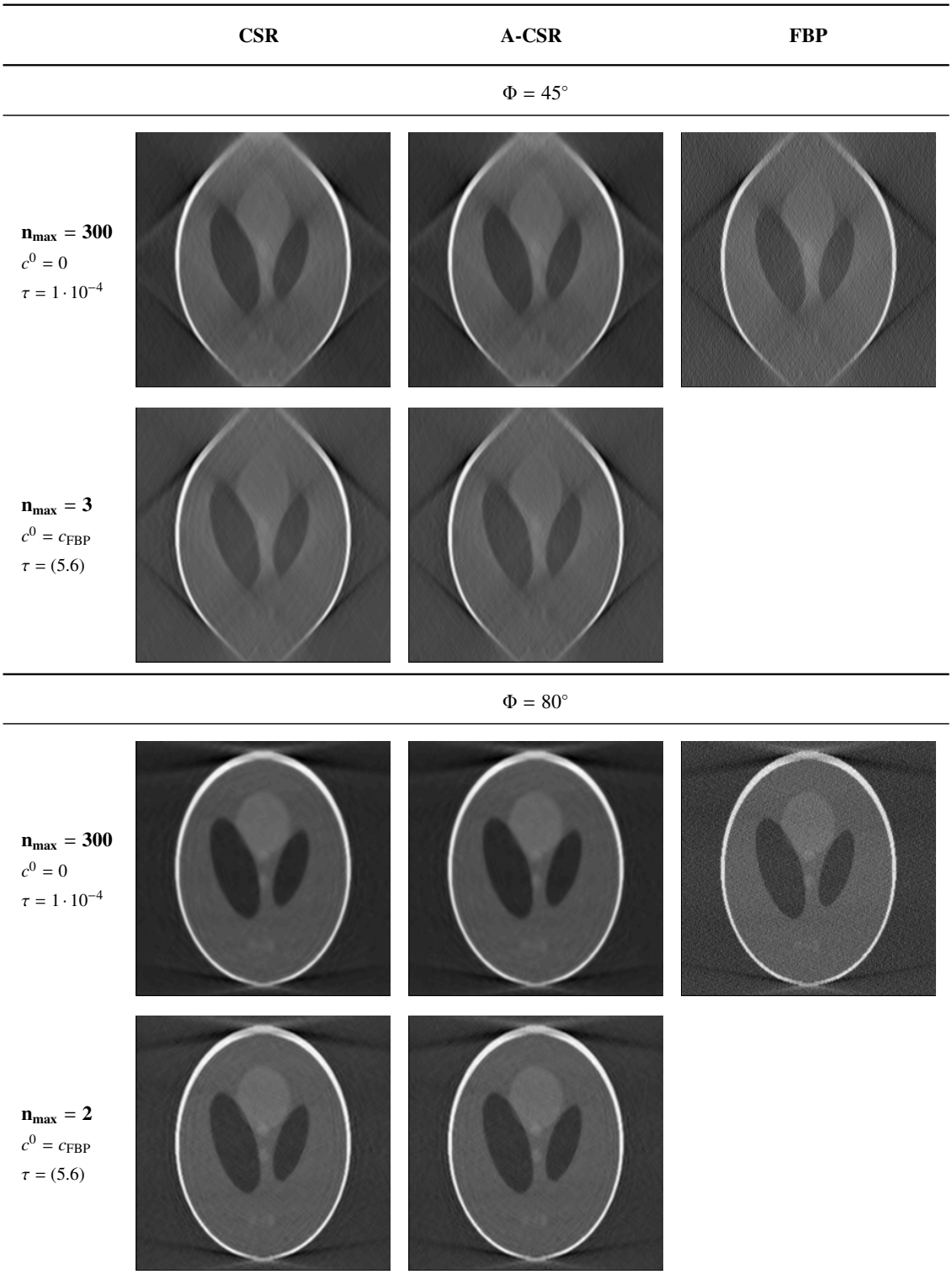

Figure 5.7: Reconstructions of the Shepp-Logan head phantom of size 256×256 (Figure 5.4(a)) at the angular range $[-\Phi, \Phi]$ and noise level 2% by using CSR (left column), A-CSR (middle column) and FBP (right column). The upper half shows reconstructions corresponding to the angular range parameter $\Phi = 45°$, whereas the lower half contains reconstructions corresponding to $\Phi = 80°$. CSR as well as A-CSR reconstructions were computed by using Algorithm 1 with the following parameters: *Row 1:* $n_{\max} = 300$, $c^0 = 0$, constant threshold $\tau = 1 \cdot 10^{-4}$; *Row 2:* $n_{\max} = 3$, $c^0 = c_{\mathrm{FBP}}$, adaptive thresholding rule (5.6); *Row 3:* $n_{\max} = 300$, $c^0 = 0$, constant threshold $\tau = 1 \cdot 10^{-4}$; *Row 4:* $n_{\max} = 2$, $c^0 = c_{\mathrm{FBP}}$, adaptive thresholding rule (5.6).

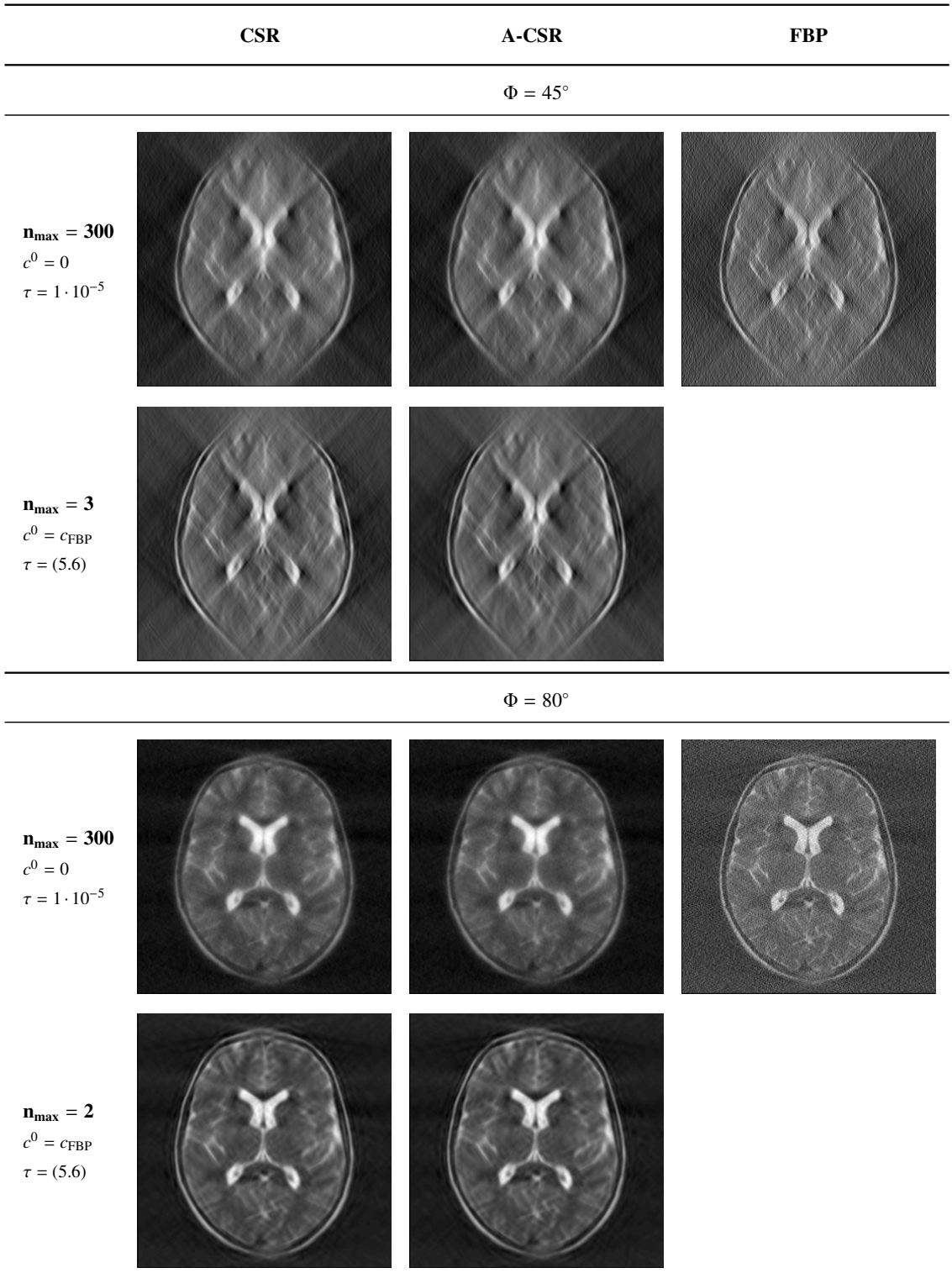

Figure 5.8: Reconstructions of the brainstem glioma of size 300×300 (Figure 5.4(b)) at the angular range $[-\Phi, \Phi]$ and noise level 2% using CSR (left column), A-CSR (middle column) and FBP (right column). The upper half shows reconstructions corresponding to the angular range parameter $\Phi = 45°$, whereas the lower half contains reconstructions corresponding to $\Phi = 80°$. CSR as well as A-CSR reconstructions were computed by using Algorithm 1 with the following parameters: *Row 1:* $n_{\max} = 300$, $c^0 = 0$, constant threshold $\tau = 1 \cdot 10^{-5}$; *Row 2:* $n_{\max} = 3$, $c^0 = c_{\mathrm{FBP}}$, adaptive thresholding rule (5.6); *Row 3:* $n_{\max} = 300$, $c^0 = 0$, constant threshold $\tau = 1 \cdot 10^{-5}$; *Row 4:* $n_{\max} = 2$, $c^0 = c_{\mathrm{FBP}}$, adaptive thresholding rule (5.6).

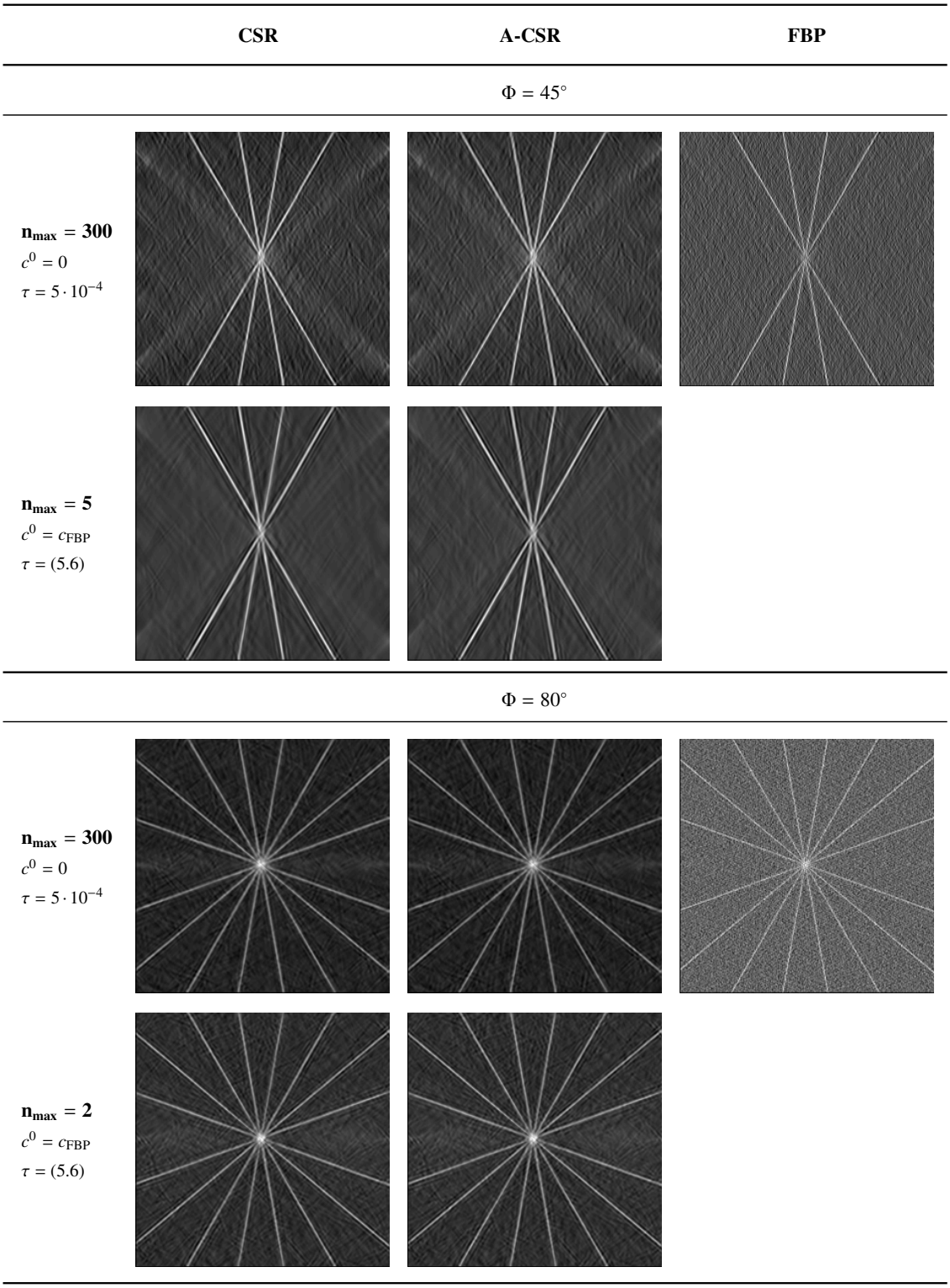

Figure 5.9: Reconstructions of the radial pattern of size 256×256 (Figure 5.4(c)) at the angular range $[-\Phi, \Phi]$ and noise level 2% using CSR (left column), A-CSR (middle column) and FBP (right column). The upper half shows reconstructions corresponding to the angular range parameter $\Phi = 45°$, whereas the lower half contains reconstructions corresponding to $\Phi = 80°$. CSR as well as A-CSR reconstructions were computed by using Algorithm 1 with the following parameters: *Row 1:* $n_{\max} = 300$, $c^0 = 0$, constant threshold $\tau = 5 \cdot 10^{-4}$; *Row 2:* $n_{\max} = 5$, $c^0 = c_{\mathrm{FBP}}$, adaptive thresholding rule (5.6); *Row 3:* $n_{\max} = 300$, $c^0 = 0$, constant threshold $\tau = 5 \cdot 10^{-4}$; *Row 4:* $n_{\max} = 2$, $c^0 = c_{\mathrm{FBP}}$, adaptive thresholding rule (5.6).

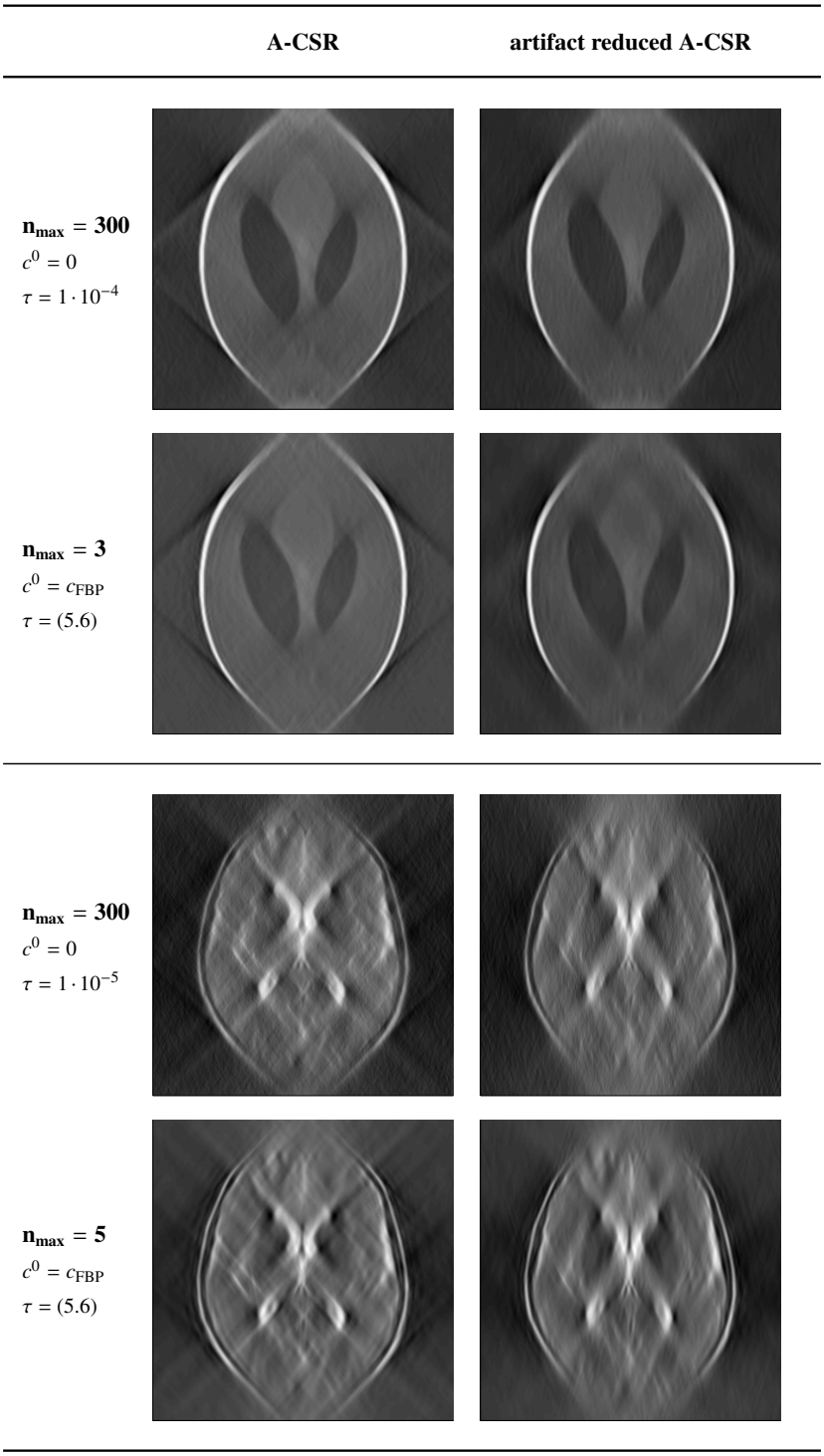

Figure 5.10: Limited angle reconstructions at the angular range $[-45°, 45°]$. Each row shows an A-CSR reconstruction from Figure 5.7 or 5.8, respectively, and a corresponding artifact reduced A-CSR reconstruction. All reconstructions were computed by using Algorithm 1 with the parameters that are given in the corresponding rows.

Appendix A

The Fourier transform and Sobolev spaces

In this chapter we summarize some basic facts about the regular and the distributional Fourier transforms and introduce the Sobolev spaces H^s. For details on Fourier analysis and distribution theory we refer to [SW71], [RS72], [Rud91], [Hör03], for details on Sobolev spaces we refer to [AF03].

A.1 The Fourier transform

The Fourier transform is a basic tool in tomography, and hence it is used extensively throughout this work. In this section we define the Fourier transform on various function spaces such as $L^1(\mathbb{R}^n)$, $L^2(\mathbb{R}^n)$ and $\mathcal{S}(\mathbb{R}^n)$. Moreover, we will give the basic definitions of tempered distributions and define the distributional Fourier transform which will be particularly used in Sections 3.3 and 3.4.

We state the definition of the Fourier transform first and list some of its properties.

Definition A.1 (Fourier transform). *Let $f \in L^1(\mathbb{R}^n)$. The Fourier transform of f is defined via*

$$\mathcal{F}f(\xi) := \hat{f}(\xi) = (2\pi)^{-n/2} \int_{\mathbb{R}^n} f(x) e^{-ix\xi} \, \mathrm{d}x. \qquad \lrcorner$$

It is easy to see that the Fourier transform of a function $f \in L^1(\mathbb{R}^n)$ is well-defined. The first important observation is that in this case the Fourier transform is even continuous. In particular, the pointwise evaluation makes sense.

Lemma A.2 (Riemann-Lebesgue, [SW71, Theorem 1.1 + 1.2]). *If $f \in L^1(\mathbb{R}^n)$, then $\hat{f}$ is uniformly continuous and $\lim_{|\xi|\to\infty} \left|\hat{f}(\xi)\right| = 0$. Furthermore, if $C_0(\mathbb{R}^n)$ denotes the space of continuous functions vanishing at infinity, then the Fourier transform $\mathcal{F} : L^1(\mathbb{R}^n) \to C_0(\mathbb{R}^n)$ is a bounded operator with $\|\mathcal{F}\| \leq (2\pi)^{-n/2}$.* $\lrcorner$

Although, by Lemma A.2, the Fourier transform of $f \in L^1(\mathbb{R}^n)$ vanishes at infinity, it does not necessarily hold that $\hat{f} \in L^1(\mathbb{R}^n)$. In order to define the inverse Fourier transform, we therefore have to assume that $\hat{f} \in L^1(\mathbb{R}^n)$. In this case we make the following definition.

Definition A.3 (Inverse Fourier transform). *Let $g \in L^1(\mathbb{R}^n)$. The inverse Fourier transform of f is defined via*

$$\mathcal{F}^{-1}g(x) := \check{g}(x) = (2\pi)^{-n/2} \int_{\mathbb{R}^n} f(\xi) e^{ix\xi} \, \mathrm{d}\xi. \qquad \lrcorner$$

Indeed, if $\hat{f} \in L^1(\mathbb{R}^n)$, it holds that $\mathcal{F}^{-1}(\hat{f})(x) = f(x)$, cf. [SW71, Cor. 1.21]. In this case, by the lemma of Riemann-Lebesgue, the function f is continuous and the equality holds pointwise.

Another important property is the following.

Proposition A.4 (Parseval's identity, [SW71, Theorem 1.15]). *If $f, g \in L^1(\mathbb{R}^n)$, then*

$$\int_{\mathbb{R}^n} \hat{f}(x) g(x) \, \mathrm{d}x = \int_{\mathbb{R}^n} f(x) \hat{g}(x) \, \mathrm{d}x. \qquad \lrcorner$$

One of the most fundamental properties of the Fourier transform is the following convolution theorem that states that the Fourier transform maps convolution into multiplication and vice versa.

Proposition A.5 (Convolution theorem, [SW71, Theorem 1.4]). *The convolution of two functions $f, g \in L^1(\mathbb{R}^n)$,*

$$f * g(x) = \int_{\mathbb{R}^n} f(y - x) g(y) \, \mathrm{d}y,$$

satisfies

$$\mathcal{F}(f * g) = (2\pi)^{n/2} \, \hat{f} \cdot \hat{g}. \tag{A.1}$$

If in addition $\hat{f}, \hat{g} \in L^1(\mathbb{R}^n)$, then

$$\mathcal{F}(f \cdot g) = (2\pi)^{-n/2} \, \hat{f} * \hat{g}. \tag{A.2}$$

$\lrcorner$

In order to define the Fourier transform on $L^2(\mathbb{R}^n)$, we first observe that, for all $f \in L^1(\mathbb{R}^n) \cap L^2(\mathbb{R}^n)$, the following identity holds, [SW71, Thm. 2.1]

$$\|f\|_2 = \left\|\hat{f}\right\|_2. \tag{A.3}$$

Since $L^1(\mathbb{R}^n) \cap L^2(\mathbb{R}^n) \subseteq L^2(\mathbb{R}^n)$ is dense, we can continuously extend the Fourier transform to a unitary operator $\mathcal{F} : L^2(\mathbb{R}^n) \to L^2(\mathbb{R}^n)$. In the literature, this operator is often called the *Plancherel transform*. However, in this work we will always use the term Fourier transform. The inverse Fourier transform on $L^2(\mathbb{R}^n)$ can be defined by letting $\mathcal{F}^{-1}f(x) = \mathcal{F}f(-x)$. We see that the Fourier transform as well as its inverse are defined the whole of $L^2(\mathbb{R}^n)$ and that according to (A.3) it is an isometry. However, defining the Fourier transform on $L^2(\mathbb{R}^n)$ has the disadvantage that the point evaluation $\mathcal{F}f(\xi)$ makes sense only almost everywhere.

A central role in the theory of Fourier transforms is played by the space of Schwartz functions which we now define.

Definition A.6 (Schwartz space). *The Schwartz space $\mathcal{S}(\mathbb{R}^n)$ is defined as a set of all functions $f \in C^\infty(\mathbb{R}^n)$ for which*

$$\|f\|_{\alpha,\beta} := \sup_{x\in\mathbb{R}^n} \left| x^\beta D^\alpha f(x) \right| < \infty \tag{A.4}$$

for all multi-indices $\alpha, \beta \in \mathbb{N}_0^n$, where $D^\alpha = \partial^\alpha / \partial x^\alpha$. The natural topology on $\mathcal{S}(\mathbb{R}^n)$ is considered to be the one induced by the family of seminorms $\|\cdot\|_{\alpha,\beta}$. ⌟

The importance of the space $\mathcal{S}(\mathbb{R}^n)$ is due to the following result, [SW71, Sec. I.3].

Proposition A.7. *The Fourier transform $\mathcal{F} : \mathcal{S}(\mathbb{R}^n) \to \mathcal{S}(\mathbb{R}^n)$ is an automorphism and its inverse is defined in Definition A.3.* ⌟

We list some more properties of the Fourier transform, [SW71], [Rud91, Chap. 7].

Proposition A.8. *Let $f \in \mathcal{S}(\mathbb{R}^n)$.*

(i) For $y \in \mathbb{R}^n$ and $\tau_y f(x) := f(x - y)$ it holds that

$$\widehat{\tau_y f}(\xi) = e^{-iy\xi} \hat{f}(\xi). \tag{A.5}$$

(ii) For $a > 0$ and $D_a f(x) := f(ax)$ it holds that

$$\widehat{D_a f}(\xi) = a^{-n} \hat{f}(a^{-1}\xi). \tag{A.6}$$

(iii) Let R be a rotation and $\varrho f(x) := f(Rx)$. Then,

$$\widehat{\varrho f}(\xi) = \hat{f}(R\xi). \tag{A.7}$$

(iv) Let $\alpha \in \mathbb{N}_0^n$ a multi-index and $D^\alpha = \partial^\alpha / \partial \xi^\alpha$ or $D^\alpha = \partial^\alpha / \partial x^\alpha$, respectively. Then

$$D^\alpha(\mathcal{F} f) = (-i)^{|\alpha|} \mathcal{F}(x^\alpha f), \quad \mathcal{F}(D^\alpha f) = i^{|\alpha|} \xi^\alpha \mathcal{F} f. \tag{A.8}$$

⌟

We shall now define the Fourier transform for distributions. To this end, we first introduce the notion of a tempered distribution.

Definition A.9 (Tempered distributions). *The topological dual space of $\mathcal{S}(\mathbb{R}^n)$ with respect to the natural topology, denoted by $\mathcal{S}'(\mathbb{R}^n)$, is called the space of tempered distributions.* ⌟

We note that $L^p(\mathbb{R}^n) \subseteq \mathcal{S}'(\mathbb{R}^n)$ for $1 \le p \le \infty$, in the sense that for each $f \in L^p(\mathbb{R}^n)$ the functional $T_f : \mathcal{S}(\mathbb{R}^n) \to \mathbb{R}$,

$$T_f(\varphi) = \int_{\mathbb{R}^n} f(x)\varphi(x)\,\mathrm{d}x$$

is a tempered distribution, [Rud91, Chap. 7]. Distributions of the form T_f are called regular.

In what follows, we denote the action of the tempered distributions $T \in \mathcal{S}'(\mathbb{R}^n)$ on test functions $\varphi \in \mathcal{S}(\mathbb{R}^n)$ by $\langle T, \varphi \rangle = T(\varphi)$.

Definition A.10 (Fourier transform of a tempered distribution). *Let $T \in \mathcal{S}'(\mathbb{R}^n)$. The Fourier transform $\widehat{T}$ defined by*

$$\langle \widehat{T}, \varphi \rangle = \langle T, \widehat{\varphi} \rangle, \quad \varphi \in \mathcal{S}(\mathbb{R}^n).$$ ⌟

We note that the Fourier transform of a tempered distribution is itself a tempered distribution, [Rud91, Chap. 7]. If $T \in \mathcal{S}'(\mathbb{R}^n)$ is a regular distribution, i.e., $T = T_f$ for some function f, we have $\widehat{T}_f = T_{\hat{f}}$ whenever $\hat{f}$ is defined. That is, the definition of the classical and the distributional Fourier transform coincide.

As in the case of the Schwartz space $\mathcal{S}(\mathbb{R}^n)$, the space of tempered distributions plays also a central role for Fourier analysis.

Proposition A.11 ([Hör03, Thm. 7.1.5]). *The Fourier transform is an automorphism of $\mathcal{S}'(\mathbb{R}^n)$ with respect to the weak topology, and the inverse Fourier transform is given by*

$$\langle \check{T}, \varphi \rangle = \langle T, \check{\varphi} \rangle, \quad \varphi \in \mathcal{S}(\mathbb{R}^n).$$ ⌟

Many properties of the ordinary Fourier transform carry over to the distributional Fourier transform. However, in order to do that, corresponding operations must be defined for distributions. We begin by restating the property (A.8) for the distributional differentiation. To this end, we recall that, for $T \in \mathcal{S}'(\mathbb{R}^n)$, the tempered distribution $D^\alpha T$ is defined via

$$\langle D^\alpha T, \varphi \rangle = (-1)^{|\alpha|} \langle T, D^\alpha \varphi \rangle, \tag{A.9}$$

for all $\varphi \in \mathcal{S}(\mathbb{R}^n)$. With this definition, the property (A.8) also holds in the distributional setting. However, in order to understand (A.8) in the distributional setting, we note that the multiplication of a tempered distribution $T \in \mathcal{S}'(\mathbb{R}^n)$ with a function $f \in C^\infty(\mathbb{R}^n)$ of at most polynomial growth is defined by $\langle fT, \varphi \rangle = \langle T, f\varphi \rangle$ for all $\varphi \in \mathcal{S}(\mathbb{R}^n)$.

We proceed to the distributional definition of convolution, [Hör03, Chap. IV].

Definition A.12 (Convolution of a tempered distribution with a function). *Let $f \in \mathcal{S}(\mathbb{R}^n)$, $T \in \mathcal{S}'(\mathbb{R}^n)$ and denote $\widetilde{f}(x) = f(-x)$. Then, the convolution of f and T is the tempered distribution $T * f$ defined by*

$$\langle T * f, \varphi \rangle = \langle T, \widetilde{f} * \varphi \rangle,$$

for all $\varphi \in \mathcal{S}(\mathbb{R}^n)$. ⌟

It is also possible to define convolution of distributions. However, this is possible only if one of these distributions has compact support.

Definition A.13 (Distributions with compact support). *The support of a tempered distribution $T \in \mathcal{S}'(\mathbb{R}^n)$, denoted by* $\operatorname{supp} T$*, is defined as the complement of the biggest open set $U \in \mathbb{R}^n$ for which $\langle T, \varphi \rangle = 0$ for all $\varphi \in \mathcal{S}(\mathbb{R}^n)$ with* $\operatorname{supp} \varphi \in U$*. The set of all distributions of compact support is denoted by $\mathcal{E}'(\mathbb{R}^n)$.* ⌟

Now we can define the convolution of two distributions, [Hör03, Chap. IV].

Definition A.14. *Let $T \in \mathcal{S}'(\mathbb{R}^n)$ and $S \in \mathcal{E}'(\mathbb{R}^n)$. The convolution $\Lambda := T * S$ is the distribution $\Lambda \in \mathcal{S}'(\mathbb{R}^n)$ defined via*

$$\Lambda * \varphi = T * (S * \varphi), \quad \varphi \in \mathcal{S}(\mathbb{R}^n). \tag{A.10}$$

⌟

Actually, it is not obvious that the convolution of $T \in \mathcal{S}'(\mathbb{R}^n)$ and $S \in \mathcal{E}'(\mathbb{R}^n)$ is well-defined and, in particular, that $T * S \in \mathcal{S}'(\mathbb{R}^n)$. For a detailed exposition we refer to [Hör03, Chap. IV]. However, for all distributional convolutions defined above, there is a convolution theorem for the (distributional) Fourier transform.

Proposition A.15 (Convolution theorem, [Hör03, Thm. 7.1.18]). *Let $T \in \mathcal{S}'(\mathbb{R}^n)$ and $S \in \mathcal{E}'(\mathbb{R}^n)$ or $S \in \mathcal{S}(\mathbb{R}^n)$. Then,*

$$\mathcal{F}(T * S) = (2\pi)^{n/2} \widehat{T} \cdot \widehat{S}. \tag{A.11}$$

⌟

We remark that the product (A.11) is well-defined: In the case $S \in \mathcal{S}(\mathbb{R}^n)$ this is clear. The other case, $S \in \mathcal{E}'(\mathbb{R}^n)$, is due to the following proposition.

Proposition A.16 ([Hör03, Thm. 7.1.14]). *The Fourier transform of a distribution $S \in \mathcal{E}'(\mathbb{R}^n)$ is the function*

$$\widehat{S}(\xi) = \left\langle S, e^{-i\langle \cdot, \xi \rangle} \right\rangle. \tag{A.12}$$

Moreover, the function $\widehat{S}(\xi)$ is defined for every complex number $\xi \in \mathbb{C}$ and is a real analytic function of ξ. In particular, $\widehat{S} \in C^\infty(\mathbb{R}^n)$. ⌟

Eventually, we note another property that will be used in this work.

Proposition A.17 ([Hör03, Thm. 7.1.16]). *Let $T \in \mathcal{S}'(\mathbb{R}^n)$ be homogeneous of degree α. That is, $\langle T, \varphi \rangle = t^\alpha \langle T, \varphi_t \rangle$ for all $\varphi \in \mathcal{S}(\mathbb{R}^n)$, where $\varphi_t(x) = t^n \varphi(tx)$, $t > 0$. Then $\widehat{T}$ is homogeneous of degree $-\alpha - n$.* ⌟

A.2 Sobolev spaces

We give some basic definitions and facts about Sobolev spaces. These are of particular interest for the understanding of the ill-posedness of an inverse problem (cf. Chapter C) and especially the ill-posedness of computed tomography (cf. Subsections 2.3.3 and Section 3.5). In particular, we will state the characterization of Sobolev spaces by means of the Fourier transform. For details we refer to [AF03].

We begin with the standard definition of Sobolev spaces. For $m \in \mathbb{N}$ we define the Sobolev space $H^m(\mathbb{R}^n)$ as

$$H^m(\mathbb{R}^n) = \left\{ f \in L^2(\mathbb{R}^n) : \ \|f\|_{H^m(\mathbb{R}^n)} < \infty \right\}, \tag{A.13}$$

where

$$\|f\|^2_{H^m(\mathbb{R}^n)} = \sum_{|\alpha| \le m} \left\| D^\alpha f \right\|_2^2, \tag{A.14}$$

for a multi-index $\alpha \in \mathbb{N}_0^n$ and $D^\alpha = \partial^\alpha / \partial x^\alpha$. We have to remark that in the above definition the differential $D^\alpha f$ of a function $f \in L^2(\mathbb{R}^n)$ is understood in the distributional sense, cf. (A.9). In addition, it is assumed that the tempered distribution $D^\alpha f$ is actually a function. Then, the definition (A.13) together with (A.14) implies that the space $H^m(\mathbb{R}^n)$ consists of all $f \in L^2(\mathbb{R}^n)$ whose derivatives $D^\alpha f$, $|\alpha| \leq m$, are also in in $L^2(\mathbb{R}^n)$. In this case, the function f is called weakly differentiable of order m.

Before stating the properties of Sobolev spaces, we note an equivalent characterization of spaces $H^m(\mathbb{R}^n)$ via the Fourier transform. To this end, we note that

$$\|f\|_m := \left(\int_{\mathbb{R}^d} \left| \hat{f}(\xi) \right|^2 (1 + \|\xi\|_2^2)^m \, \mathrm{d}\xi \right)^{\frac{1}{2}} \tag{A.15}$$

defines an equivalent norm to (A.14). Observe that this characterization relates the decay properties of the Fourier transform $\hat{f}$ to the weak differentiability of $f \in L^2(\mathbb{R}^n)$. An essential ingredient to the proof of this norm equivalence is the property (A.8). So, replacing the norm $\|\cdot\|_{H^m(\mathbb{R}^n)}$ in the definition of (A.13) does not change the space H^m.

The characterization of Sobolev spaces by means of the Fourier transform does not only give a handy tool to investigate smoothness of a function but also offers a possibility to generalize the definition of Sobolev spaces of integer order $H^m(\mathbb{R}^n)$ to spaces $H^s(\mathbb{R}^n)$ of arbitrary smoothness $s \in \mathbb{R}$. To this end, we only need to replace the integer m in the definition (A.15) by the real number s. However, if $s < 0$, we have to enlarge the basic set from $L^2(\mathbb{R}^n)$ (cf. (A.13)) to the space of tempered distributions $\mathcal{S}'(\mathbb{R}^n)$. That is, for $s \in \mathbb{R}^n$, we define

$$H^s(\mathbb{R}^n) = \left\{ f \in \mathcal{S}'(\mathbb{R}^n) : \ \hat{f} \text{ is a function and } \|f\|_s < \infty \right\}, \tag{A.16}$$

where $\|\cdot\|_s$ denotes the norm defined in (A.15) with m replaces by s.

Finally we define the Sobolev spaces $H_0^s(\Omega)$, where $\Omega \in \mathbb{R}^n$ is an open subset, by

$$H_0^s(\Omega) = \left\{ f \in H^s(\mathbb{R}^n) : \ \operatorname{supp} f \subseteq \overline{\Omega} \right\}. \tag{A.17}$$

The norm in $H_0^s(\Omega)$ is the same as in $H^s(\mathbb{R}^n)$, namely (A.15).

We eventually list some properties of Sobolev spaces.

(i) The spaces $H^s(\mathbb{R}^n)$ and $H_0^s(\Omega)$ are Hilbert spaces with the following inner product,

$$\langle f, g \rangle_s = \int_{\mathbb{R}^n} (1 + \|\xi\|_2^2)^s \hat{f}(\xi) \overline{\hat{g}}(\xi) \, \mathrm{d}\xi.$$

(ii) $H^s(\mathbb{R}^n) \subseteq H^t(\mathbb{R}^n)$ if $t < s$.

(iii) Every distribution with compact support $f \in \mathcal{E}'(\mathbb{R}^n)$ lies in some $H^s(\mathbb{R}^n)$.

(iv) The dual of $H^s(\mathbb{R}^n)$ is topologically isomorphic to $H^{-s}(\mathbb{R}^n)$.

Appendix B

Singular value decomposition of compact operators

In order to make this thesis self-contained, we summarize the basic definitions and properties of compact operators. In particular, we present the spectral theory and singular value decomposition of compact operators. For further reading we refer to [RS72] and [RY08].

B.1 Some properties of compact operators

Definition B.1 (Compact operator). *Let X and Y be normed spaces. A linear operator $T : X \to Y$ is compact if for any bounded set $B \subseteq X$ the image $T(B)$ is relatively compact, i.e., the closure $\overline{T(B)}$ is compact in Y. The set of compact operators is denoted by $K(X, Y)$.* ⌟

Equivalently, an operator T is compact if for any sequence $\{x_n\} \subseteq X$ the sequence $\{Tx_n\} \subseteq Y$ contains a convergent subsequence.

The basic properties of compact operators are summarized in the following proposition, [RY08, Chapter 7].

Proposition B.2. *Let X, Y, Z be normed spaces.*

(i) Every compact operator $T \in K(X, Y)$ is bounded.

(ii) $K(X, Y)$ is a closed linear subspaces of $\mathcal{L}(X, Y)$, where $\mathcal{L}(X, Y)$ is the space of all linear bounded operators. Especially, if $\{T_n\} \subseteq K(X, Y)$ converges to a $T \in \mathcal{L}(X, Y)$, then T is compact.

(iii) If $S \in \mathcal{L}(X, Y)$, $T \in \mathcal{L}(Y, Z)$ and at least one of the operators S, T is compact, then $TS \in K(X, Z)$.

(iv) If $\dim X = \infty$ and $T \in K(X, X)$, then T is not invertible.

(v) If $T \in K(X, Y)$ then $\operatorname{ran}(T)$ and $\overline{\operatorname{ran}(T)}$ are separable, i.e., even if the space X is big (not separable), the range of T is still small (not separable).

(vi) A compact operator maps weakly convergent sequences into strongly convergent sequences.

(vii) *Let X be a normed space and H a Hilbert space. Further, let $F(X,H)$ denote the set of all operators $F \in \mathcal{L}(X,H)$ which have a finite rank, i.e., $r(F) = \dim(\operatorname{ran}(F)) < \infty$. Then, for every $T \in K(X,H)$ there is a sequence $\{T_n\} \subseteq F(X,H)$ converging strongly (in $\mathcal{L}(X,H)$) to T, i.e., $\overline{F(X,H)} = K(Y,H)$.* ⌟

Moreover, we have the following properties of compact operators on Hilbert spaces, [RY08, Lem. 7.13, Thm. 7.14].

Proposition B.3. *Let H be a Hilbert space and $T \in \mathcal{L}(H) := \mathcal{L}(H,H)$. If T^* denotes the Hilbert spaces adjoint of T, then*

(i) *$r(T) = r(T^*)$. In particular, T has finite rank if and only if T^* has finite rank.*

(ii) *T is compact if and only if T^* is compact.* ⌟

B.2 Spectral theorem and singular value decomposition of compact operators

Although we are interested only in the Hilbert space setting, we recall the basic definitions from the spectral theory of operators on Banach spaces.

Definition B.4. *Let X be a Banach space and $T \in \mathcal{L}(X)$.*

(i) *The* resolvent set *of T is defined by*

$$\varrho(T) = \left\{\lambda \in \mathbb{C} : (\lambda - T)^{-1} \text{ exists in } \mathcal{L}(X)\right\}.$$

(ii) *The* spectrum *of T is defined by*

$$\sigma(T) = \mathbb{C} \setminus \varrho(T).$$

(iii) *The* point spectrum *of T is defined by*

$$\sigma_p(T) = \{\lambda \in \sigma(T) : (\lambda - T) \text{ is not injective}\}.$$

The elements of $\sigma_p(T)$ are called eigenvalues. *For $\lambda \in \sigma_p(T)$ there is a corresponding* eigenvector *or* eigenfunction *$x \in X$ such that $x \neq 0$ and $Tx = \lambda x$.* ⌟

In what follows we let $K(H)$ be the set of all compact operators $T : H \to H$ on a Hilbert space H. The following theorem shows that non-zero elements of the spectrum $\sigma(T)$ are actually eigenvalues of T.

Theorem B.5. *Let H be a Hilbert space and $T \in K(H)$. Then, $\sigma(T)$ is a discrete (countable) set having no limit points except perhaps $\lambda = 0$. Further, any nonzero $\lambda \in \sigma(T)$ is an eigenvalue of finite multiplicity (i.e., the corresponding space of eigenvectors if finite dimensional). In particular, if $\{\lambda_n\} \subseteq \sigma_p(T)$ is any sequence of distinct eigenvalues of T, then* $\lim_{n\to\infty} \lambda_n = 0$. ⌟

We have the following spectral theorem for self-adjoint compact operators, [RS72, Sec. VI.5], [RY08, Sec. 7.2].

Theorem B.6 (Spectral theorem for self-adjoint compact operators). *Let H be a Hilbert space and let $T \in K(H)$ be self-adjoint. Then, there exists an orthonormal system $\{\psi_n\} \subseteq H$ and a (maybe finite) sequence $\{\lambda_n\} \in \mathbb{C} \setminus \{0\}$ with $\lim_n \lambda_n = 0$ such that the following relations hold:*

$$H = \ker(T) \oplus \overline{\operatorname{span}\{\psi_1, \psi_2, \dots\}}$$

and

$$Tx = \sum_n \lambda_n \langle x, \psi_n \rangle \psi_n \qquad \forall x \in H.$$

Here, the values λ_n are eigenvalues of T, and ψ_n are the corresponding eigenfunctions. Furthermore it holds that

$$\|T\| = \sup_n |\lambda_n|. \qquad \lrcorner$$

The above spectral theorem does not apply for general compact operators $T : X \to Y$. However, applying the spectral theorem to the self-adjoint compact operator T^*T we get the following analog to Theorem B.6, cf. [RS72, Sec. VI.5], [RY08, Sec. 7.2].

Theorem B.7 (Singular value decomposition of a compact operator). *Let X and Y be Hilbert spaces and let $T \in K(X, Y)$. There exist orthonormal systems $\{v_n\} \subseteq X$, $\{u_n\} \subseteq Y$ and a sequence $\sigma_1 \geq \sigma_2 \geq \cdots > 0$ with $\lim_n \sigma_n = 0$, such that the following relations hold:*

$$Tv_n = \sigma_n u_n, \tag{B.1}$$

$$T^*u_n = \sigma_n v_n, \tag{B.2}$$

$$Tx = \sum_n \sigma_n \langle x, v_n \rangle u_n, \qquad x \in X, \tag{B.3}$$

$$T^*y = \sum_n \sigma_n \langle y, u_n \rangle v_n, \qquad y \in Y. \tag{B.4}$$

$(\sigma_n; v_n, u_n)$ is called singular system *of T; σ_n are the* singular values *of T; the representation* (B.3) *is called* singular value decomposition *(SVD) of T.* $\lrcorner$

Appendix C

Basic facts about inverse problems

The goal of this chapter is to recall the basic definitions and notations from the theory of inverse problems and regularization. For details we refer to [EHN96], [Kir96], [Lou89].

C.1 Ill-posedness

In what follows we assume $R : X \to Y$ to be a compact linear operator between Hilbert spaces X and Y. We consider an inverse problem which is given by the operator equation

$$y = Rf. \tag{C.1}$$

That is, given y, we are interested in determining (or reconstructing) the unknown function f. Mathematically, the problem consists in solving the operator equation (C.1). In the context of inverse problems the operator R is called *forward operator* whereas y is the *data* or, alternatively, the *measurements* of the object f.

In practice, the measurements $y \in Y$ are usually corrupted by noise $\eta \in Y$, $\|\eta\|_Y \leq \delta$. Hence, given the *noisy data* $y^\delta = y + \eta$, the goal is to solve the perturbed problem

$$y^\delta = Rf + \eta. \tag{C.2}$$

In this situation it is natural to ask how the measurement errors are propagated through the solution process. In order to study this behavior, the concept of well-posedness of a problem is used.

Definition C.1. *Let X and Y be Hilbert spaces, $R : X \to Y$ a linear operator. The problem $Rf = y$ is called* well-posed *by Hadamard if the following conditions are satisfied:*

(i) Existence: *For every $y \in Y$ there is a $f \in X$ such that $Rf = y$.*

(ii) Uniqueness: *For every $y \in Y$ there is at most one $f \in X$ with $Rf = y$.*

(iii) Stability: *The solution f depends continuously on y.*

Problems for which at least one of the above conditions is violated are called ill-posed. ⌟

Note that in Definition C.1 the properties (i) and (ii) are of pure algebraic nature. However, condition (iii) requires the continuity of the solution operator which involves topological structure of the spaces X and Y.

If the data is corrupted by noise and if $\operatorname{ran}(R) \neq Y$, we generally have $y^\delta \notin \operatorname{ran}(R)$. In this case the problem (C.2) can not be solved in the classical setting. Nevertheless, we can obtain an approximate solution f by minimizing the error term $\|y - Rf\|_Y$. In this case, the approximate solution is called *least-squares solution*. Formally, f is a least-squares solution if

$$\|y - Rf\|_Y = \inf \{\|y - Rg\|_Y : \ g \in X\}. \tag{C.3}$$

Note that, if $y \in \operatorname{ran}(R) \oplus \operatorname{ran}(R)^\perp$, the set of all least-squares solution is characterized by the *normal equation*

$$R^*Rf = R^*y. \tag{C.4}$$

Moreover, note that the least-squares solution is not unique if R is not injective. A standard way to restore uniqueness is to choose a least-squares solution with the smallest norm. Such solutions are called *best approximate solutions* or *generalized solutions* of $Rf = y$ and are denoted by $f^\dagger$. Formally, $f^\dagger$ is a best approximate solution of $Rf = y$ if

$$\|f^\dagger\|_X = \inf \{\|g\|_X : \ f \text{ is a least-squares solution of } Rf = y\}. \tag{C.5}$$

Because of the above considerations it is very natural to study the operator which maps the data $y = Rf$ to the best approximate solution $f^\dagger$.

Definition C.2 (Moore-Penrose generalized inverse). *Let $R : X \to Y$ be a bounded linear operator between Hilbert spaces X and Y. The* Moore-Penrose generalized inverse $R^\dagger$ *of R is defined as*

$$R^\dagger : \mathcal{D}(R^\dagger) := \operatorname{ran}(R) \oplus \operatorname{ran}(R)^\perp \to X, \quad y \mapsto f^\dagger. \tag{C.6}$$

⌟

Proposition C.3 (Properties of the Moore-Penrose generalized inverse, [EHN96, Sec. 2.1]). *Let R be a bounded linear operator between Hilbert spaces X and Y, then*

(i) $\ker\left(R^\dagger\right) = \operatorname{ran}(R)^\perp$ *and* $\operatorname{ran}\left(R^\dagger\right) = \ker(R)^\perp$.

(ii) Let P and Q be the orthogonal projections onto $\ker(R)$ *and* $\overline{\operatorname{ran}(R)}$*, respectively. Then, the four Moore-Penrose equations hold:*

$$RR^\dagger R = R, \tag{C.7}$$

$$R^\dagger RR^\dagger = R^\dagger, \tag{C.8}$$

$$R^\dagger R = \mathrm{id}_X - P, \tag{C.9}$$

$$RR^\dagger = Q|_{\mathcal{D}(R^\dagger)}. \tag{C.10}$$

These equations uniquely characterize $R^\dagger$.

(iii) $R^\dagger$ has a closed graph $gr(R^\dagger)$.

(iv) $R^\dagger$ is bounded if and only if $\operatorname{ran}(R)$ *is closed.*

(v) For $y \in \mathcal{D}(R^\dagger)$, $f^\dagger = R^\dagger y$ is the unique generalized solution of $Rf = y$. The set of all least-squares solution is given by $f^\dagger + \ker(R)$. ⌟

The concept of the generalized inverse, though it provides a unique solution, does not remedy the lack of continuous dependence of the solution on the data, cf. Proposition C.3 (iv). In general we have

$$R^\dagger y^\delta \not\to R^\dagger y \text{ for } \delta \to 0. \tag{C.11}$$

Therefore, if the problem is ill-posed, even small data errors can cause huge reconstruction errors. A handy tool for the study of ill-posedness is the singular value decomposition (SVD), cf. Chapter B. Using the SVD, there is a simple representation of the Moore-Penrose generalized inverse $R^\dagger$.

Theorem C.4 ([EHN96, Th. 2.8]). *Let R be a compact linear operator between Hilbert spaces X and Y, and let $(\sigma_n; v_n, u_n)$ be a singular system for R. Then, the following statements hold.*

(i) Picard condition:

$$y \in \mathcal{D}(R^\dagger) \;\Leftrightarrow\; \sum_{n=1}^{\infty} \frac{|\langle y, u_n\rangle|^2}{\sigma_n^2} < \infty. \tag{C.12}$$

(ii) For any $y \in \mathcal{D}(R^\dagger)$

$$R^\dagger y = \sum_{n=1}^{\infty} \frac{\langle y, u_n\rangle}{\sigma_n} v_n. \tag{C.13}$$

⌟

The Theorem C.4 show that a best-approximate solution of the problem $Rf = y$ exists if the Picard condition (C.13) is satisfied. Moreover, the representation (C.13) gives a considerable insight into the inherent ill-posedness of the problem $Rf = y$: Since R is compact, it follows from Theorem B.7 that $\sigma_n \to 0$ for $n \to \infty$. Hence, the error components are amplified by the factors $1/\sigma_n$, which increase without bound. For example, if $y_{\delta,n} := y + \delta u_n$, then $\left\|y_{\delta,n} - y\right\|_Y = \delta$, but

$$\left\|R^\dagger y - R^\dagger y_{\delta,n}\right\|_X = \frac{\delta}{\sigma_n} \to \infty \text{ as } n \to \infty.$$

This means that the reconstruction error can be arbitrarily large even if the data error is small. As a result, the practical reconstruction algorithms are sensitive to noise. To stabilize the reconstruction a regularization strategy has to be applied, cf. Section C.3.

C.2 Classification of ill-posedness

Following the above discussion, it is obvious that the amplification of measurement errors depends on the decay properties of the singular values $\{\sigma_n\}$ of the operator R. The faster the decay rate of $\{\sigma_n\}$, the more amplification of the data error is inherent in the problem. This observation leads to the following classification of the degree of ill-posedness.

Definition C.5. *Let R be a compact linear operator between Hilbert spaces X and Y, and let $(\sigma_n; v_n, u_n)$ be a singular system for R. A problem $Rf = y$ is called*

(i) ill-posed of degree α *if there exists* $\alpha > 0$ *such that* $\sigma_n = O(n^{-\alpha})$,

(ii) severely ill-posed *if the singular values* $\{\sigma_n\}$ *decay exponentially.* ⌟

Another classification of ill-posedness can be defined in terms of Sobolev scales, see for example [Lou89].

Definition C.6. *Let* $R : L^2(\mathbb{R}^n) \to L^2(\mathbb{R}^n)$. *A problem* $Rf = y$ *is called ill-posed of degree* $\alpha > 0$ *if for some* $C_1, C_2 > 0$

$$C_1 \|f\|_2 \leq \|Rf\|_{H^\alpha} \leq C_2 \|f\|_2 .$$

The problem is called severely ill-posed if there are no such estimates. ⌟

The above classification of the degree of ill-posedness is based on the smoothing properties of the operator R. Definition C.6 states that the operator R is a smoothing operator of order α, i.e., the data y is α times smoother than f. The ill-posedness is therefore pronounced by the fact that, in order to solve the problem $Rf = y$ one has to invert this smoothing, i.e., one has to restore the non-smooth parts of f from smooth data y. For example, Theorem 2.13 shows that the tomographic problem $\mathcal{R}f = y$, where $\mathcal{R}$ denotes the Radon transform, is ill-posed of order $\alpha = 1/2$ in the sense of Definition C.6.

If a problem is severely ill-posed in the sense of the above definition, one can think of the involved operator R as a smoothing operator of order ∞. As a result, there is a dramatic loss of information in this situation. Unfortunately, this is exactly the case in limited angle tomography, since no Sobolev space estimate is available for the limited angle Radon transform, cf. Section 3.5.

C.3 Regularization

In order to get stable numerical algorithms, continuous dependence of the solution operator on the data is of great importance. To this end, *regularization methods* are used to compute an approximation, say $f_{\alpha,\delta}$, to $f^\dagger$ which depend continuously on the data and tends to $f^\dagger$ as $\delta \to 0$.

Definition C.7. *Let* $R : X \to Y$ *be a bounded linear operator between Hilbert spaces* X *and* Y. *A* regularization for $R^\dagger$ *is a family of linear bounded operators*

$$\{R_\alpha\}_{\alpha>0}\,,\ R_\alpha : Y \to X \tag{C.14}$$

if for all $y \in \mathcal{D}(R^\dagger)$ *there exists a* parameter choice rule

$$\alpha : \mathbb{R}_+ \times Y \to \mathbb{R}_+ \tag{C.15}$$

such that

$$\limsup_{\delta\to 0} \left\{ \left\| R_{\alpha(\delta,y^\delta)} y^\delta - R^\dagger y \right\|_X :\ y^\delta \in Y, \left\| y - y^\delta \right\|_Y \leq \delta \right\} = 0 \tag{C.16}$$

and

$$\limsup_{\delta\to 0} \left\{ \alpha(\delta, y^\delta) :\ y^\delta \in Y, \left\| y - y^\delta \right\|_Y \leq \delta \right\} = 0. \tag{C.17}$$

For a specific $y \in \mathcal{D}(R^\dagger)$, a pair (R_α, α) is called a regularization method for solving $Rf = y$; α is the regularizaiton parameter and $f_\alpha^\delta := R_\alpha y^\delta$ is called regularized solution.

If the parameter choice rule α does not depend on y^δ, but only on δ, i.e., $\alpha = \alpha(\delta)$, then α is called a-priori parameter choice rule. *Otherwise, α is called* a-posteriori parameter choice rule. ⌟

Remark. It follows directly from Definition C.7 that for all $y \in \mathcal{D}(R^\dagger)$ it holds

$$\lim_{\delta \to 0} R_{\alpha(\delta, y^\delta)} y^\delta = R^\dagger y. \tag{C.18}$$

In particular, $\{R_\alpha\}_\alpha$ converges pointwise to $R^\dagger$ on $\mathcal{D}(R^\dagger)$ as $\alpha \to 0$. As a consequence of the uniform boundedness principle (theorem of Banach-Steinhaus), we have for any regularization $\{R_\alpha\}_\alpha$ that $\|R_\alpha\| \to \infty$ as $\alpha \to 0$, whenever $\operatorname{ran}(R)$ is non-closed. ⌟

Having introduced the notion of a regularization it is very natural to ask how to construct such regularizations for $R^\dagger$. A preliminary answer to that question is given by the next proposition.

Proposition C.8 ([EHN96, Prop. 3.4]). *Let R_α be a continuous operator for all $\alpha > 0$. Then, the family $\{R_\alpha\}$ is a regularization for $R^\dagger$ if*

$$R_\alpha \to R^\dagger \text{ pointwise on } \mathcal{D}(R^\dagger) \text{ as } \alpha \to 0. \tag{C.19}$$

In this case, there exists, for every $y \in \mathcal{D}(R^\dagger)$, an a-priori parameter choice rule α such that (R_α, α) is a regularization method for solving $Rf = y$. ⌟

According to Proposition C.8, the construction of regularizations for $R^\dagger$ may be split into the construction of continuous pointwise approximations $\{R_\alpha\}_\alpha$ of $R^\dagger$ and the construction of appropriate parameter choice rules $\alpha = \alpha(\delta)$. In what follows, a family of bounded operators $\{R_\alpha\}_\alpha$ that converges pointwise to $R^\dagger$ will be called a *regularization strategy* for $R^\dagger$, [Kir96]. Now let us assume that we have constructed a regularization strategy $\{R_\alpha\}_\alpha$ for $R^\dagger$. In order to derive an appropriate parameter choice rule, let us consider the error $\|f_\alpha^\delta - f^\dagger\|_X$, where $f_\alpha^\delta = R_\alpha y^\delta$. Now, we can observe that the reconstruction error of a (linear) regularization is composed of a *data error* and an *approximation error*:

$$\begin{aligned}
\left\| f_\alpha^\delta - f^\dagger \right\|_X &= \left\| R_\alpha y^\delta - R^\dagger y \right\|_X \\
&\leq \underbrace{\left\| R_\alpha (y^\delta - y) \right\|_X}_{\text{data error}} + \underbrace{\left\| R_\alpha y - R^\dagger y \right\|_X}_{\text{approximation error}} \\
&\leq \delta \|R_\alpha\| + \left\| R_\alpha y - R^\dagger y \right\|_X .
\end{aligned}$$

Assuming that the a-priori parameter choice rule satisfies $\alpha(\delta) \to 0$ as $\delta \to 0$, we can observe that, on the one hand, the approximation error tends to zero as $\delta \to 0$. However, the data error can be arbitrarily large since $\|R_\alpha\| \to \infty$ as $\alpha \to 0$. In order to turn a regularization strategy into a regularization method, we have to design an appropriate parameter choice rule $\alpha = \alpha(\delta)$. A sufficient condition is given by the next proposition.

Proposition C.9 ([EHN96, Prop. 3.7]). *Let $\{R_\alpha\}$ be a linear regularization for $R^\dagger$. For every $y \in \mathcal{D}(R^\dagger)$ let $\alpha : \mathbb{R}^+ \to \mathbb{R}^+$ be an a-priori parameter choice rule. Then, (R_α, α) is a regularization method if and only if*

$$\lim_{\delta \to 0} \alpha(\delta) = 0 \tag{C.20}$$

and

$$\lim_{\delta \to 0} \delta \left\| R_{\alpha(\delta)} \right\| = 0 \tag{C.21}$$

holds. ⌟

Eventually, we want to point out that the notion of regularization depends on the concept of the solution for $Rf = y$. In Definition C.7, we formulated the regularization with respect to the Moore-Penrose generalized inverse $R^\dagger$. However, it is straightforward to reformulate Definition C.7 with respect to a general notion of a solution. To this end, one merely has to replace $R^\dagger$ in the Definition C.7 by a different (more general) solution operator. For example, one possibility is to choose a least-squares solution of $Rf = y$ which has minimum (semi-) norm on a certain (convex) subset C of X. This leads to a different notion of the solution of $Rf = y$. In this work, we will use the concept of least-squares solutions which has a minimal ℓ^1-norm in an appropriate coefficient space, cf. Chapter 4.

Bibliography

[AF03] Robert A. Adams and John J. F. Fournier, *Sobolev spaces*, second ed., Pure and Applied Mathematics, vol. 140, Elsevier/Academic Press, Amsterdam, 2003.

[BKP10] Kristian Bredies, Karl Kunisch, and Thomas Pock, *Total Generalized Variation*, SIAM Journal on Imaging Sciences **3** (2010), no. 3, 492 – 526.

[BL08a] Kristian Bredies and Dirk Lorenz, *Iterated Hard Shrinkage for Minimization Problems with Sparsity Constraints*, SIAM Journal on Scientific Computing **30** (2008), no. 2, 657.

[BL08b] _____, *Linear convergence of iterative soft-thresholding*, Journal of Fourier Analysis and Applications **14** (2008), 813–837.

[BLZ08] Mario Bertero, Henri Lantéri, and Luca Zanni, *Iterative image reconstruction: a point of view*, Mathematical methods in biomedical imaging and intensity-modulated radiation therapy (IMRT), CRM Series, vol. 7, Ed. Norm., Pisa, 2008, pp. 37–63.

[Bra10] *Radiopedia.org*, 2010, `http://radiopaedia.org/cases/brainstem-glioma`.

[CCN07] Vicent Caselles, Antonin Chambolle, and Matteo Novaga, *The discontinuity set of solutions of the TV denoising problem and some extensions*, Multiscale Modeling & Simulation **6** (2007), no. 3, 879–894.

[CD00] Emmanuel J. Candes and David L. Donoho, *Curvelets and reconstruction of images from noisy radon data*, Proceedings of SPIE, Wavelet Applications in Signal and Image Processing VIII, 2000, pp. 108–117.

[CD02] Emmanuel J. Candès and David L. Donoho, *Recovering edges in ill-posed inverse problems: optimality of curvelet frames*, The Annals of Statistics **30** (2002), no. 3, 784–842, Dedicated to the memory of Lucien Le Cam.

[CD04] _____, *New tight frames of curvelets and optimal representations of objects with piecewise C^2 singularities*, Communications on Pure and Applied Mathematics **57** (2004), no. 2, 219–266.

[CD05a] _____, *Continuous curvelet transform. I. Resolution of the wavefront set*, Applied and Computational Harmonic Analysis **19** (2005), no. 2, 162–197.

[CD05b] _____, *Continuous curvelet transform. II. Discretization and frames*, Applied and Computational Harmonic Analysis **19** (2005), no. 2, 198–222.

[CDDY08] Emmanuel Candès, Laurent Demanet, David L. Donoho, and Lexing Ying, *CurveLab-2.1.2*, `http://www.curvelet.org/`, 2008.

[CEGL10] Flavia Colonna, Glenn Easley, Kanghui Guo, and Demetrio Labate, *Radon transform inversion using the shearlet representation*, Applied and Computational Harmonic Analysis **29** (2010), no. 2, 232–250.

[CG02] Emmanuel J. Candès and Franck Guo, *New multiscale transforms, minimum total variation synthesis: applications to edge-preserving image reconstruction*, Signal Processing **82** (2002), no. 11, 1519–1543.

[Chr03] Ole Christensen, *An introduction to frames and Riesz bases*, Applied and Numerical Harmonic Analysis, Birkhäuser Boston Inc., Boston, MA, 2003.

[Cor63] Alan M. Cormack, *Representation of a Function by Its Line Integrals, with Some Radiological Applications*, Journal of Applied Physics **34** (1963), no. 9, 2722.

[Cor64] _____, *Representation of a Function by Its Line Integrals, with Some Radiological Applications. II*, Journal of Applied Physics **35** (1964), no. 10, 2908–2913.

[CS11] Daniela Calvetti and Erkki Somersalo, *StatisticalMethods in Imaging*, Handbook of Mathematical Methods in Imaging (Ottmar Scherzer, ed.), Springer, 2011, pp. 913–957.

[Dav83] Mark E. Davison, *The ill-conditioned nature of the limited angle tomography problem*, SIAM Journal on Applied Mathematics **43** (1983), no. 2, 428–448.

[DB95] A. H. Delaney and Y. Bresler, *Efficient edge-preserving regularization for limited-angle tomography*, Image Processing, 1995. Proceedings., International Conference on, vol. 3, oct 1995, pp. 176 –179 vol.3.

[DDDM04] Ingrid Daubechies, Michel Defrise, and Christine De Mol, *An iterative thresholding algorithm for linear inverse problems with a sparsity constraint*, Communications on Pure and Applied Mathematics **57** (2004), no. 11, 1413–1457.

[DRK68] D. J. De Rosier and A. Klug, *Reconstruction of Three Dimensional Structures from Electron Micrographs*, Nature **217** (1968), no. 5124, 130–134.

[DST09] Stephan Dahlke, Gabriele Steidl, and Gerd Teschke, *The Continuous Shearlet Transform in Arbitrary Space Dimensions*, Journal of Fourier Analysis and Applications **16** (2009), no. 3, 340–364.

[EHN96] Heinz W. Engl, Martin Hanke, and Andreas Neubauer, *Regularization of Inverse Problems*, Kluwer Academic Publishers, Dordrecht, 1996.

[ELL08] Glenn Easley, Demerito Labate, and Wang-Q Lim, *Sparse directional image representations using the discrete shearlet transform*, Applied and Computational Harmonic Analysis **25** (2008), no. 1, 25–46.

[Eps08] Charles L. Epstein, *Introduction to the mathematics of medical imaging*, second ed., Society for Industrial and Applied Mathematics (SIAM), Philadelphia, PA, 2008.

[FP11] Jalal M. Fadili and Gabriel Peyre, *Total Variation Projection With First Order Schemes*, IEEE Transactions on Image Processing **20** (2011), no. 3, 657–669.

[Fri98] F. G. Friedlander, *Introduction to the theory of distributions*, second ed., Cambridge University Press, Cambridge, 1998, With additional material by M. Joshi.

[Fri10] Jürgen Frikel, *A new framework for sparse regularization in limited angle x-ray tomography*, 2010 IEEE International Symposium on Biomedical Imaging: From Nano to Macro, IEEE, April 2010, pp. 824–827.

[Fri11] Jürgen Frikel, *Short communication: Dimensionality reduction of curvelet sparse regularizations in limited angle tomography*, Proceedings in Applied Mathematics and Mechanics (PAMM) **11** (2011), no. 1, 847–848.

[Fri12] ———, *Sparse regularization in limited angle tomography*, Applied and Computational Harmonic Analysis (2012).

[GHS08] Markus Grasmair, Markus Haltmeier, and Otmar Scherzer, *Sparse regularization with ℓ^q penalty term*, Inverse Problems **24** (2008), no. 5, 055020.

[GL07] Kanghui Guo and Demetrio Labate, *Optimally Sparse Multidimensional Representation Using Shearlets*, SIAM Journal on Mathematical Analysis **39** (2007), no. 1, 298–318.

[GL08] Roland Griesse and Dirk Lorenz, *A semismooth newton method for tikhonov functionals with sparsity constraints*, Inverse Problems **24** (2008), no. 3, 035007 (19pp).

[GL12] Kanghui Guo and Demetrio Labate, *Optimal recovery of 3d x-ray tomographic data via shearlet decomposition*, Advances in Computational Mathematics (2012), 1–29.

[Gro96] H. Groemer, *Geometric applications of Fourier series and spherical harmonics*, Encyclopedia of Mathematics and its Applications, vol. 61, Cambridge University Press, Cambridge, 1996.

[Grü80] F Alberto Grünbaum, *A study of fourier space methods for "limited angle" image reconstruction* *, Numerical Functional Analysis and Optimization **2** (1980), no. 1, 31–42.

[GS08] Loukas Grafakos and Christopher Sansing, *Gabor frames and directional time-frequency analysis*, Applied and Computational Harmonic Analysis **25** (2008), no. 1, 47–67.

[HD08] Gabor T. Herman and Ran Davidi, *Image reconstruction from a small number of projections*, Inverse Problems **24** (2008), no. 4, 045011.

[Her80] Gabor T. Herman, *Image reconstruction from projections*, Academic Press Inc. [Harcourt Brace Jovanovich Publishers], New York, 1980, The fundamentals of computerized tomography, Computer Science and Applied Mathematics.

[Her09] ———, *Fundamentals of Computerized Tomography*, Springer, London, 2009, Image Reconstruction from Projections (Advances in Computer Vision and Pattern Recognition) .

[HHK+12] Keijo Hämäläinen, Andreas Hauptmann, Aki Kallonen, Esa Niemi, and Samuli Siltanen, *Total variation regularization for X-ray tomography*, Preprint.

[HKK+12] Keijo Hämäläinen, Aki Kallonen, Ville Kohlemainen, Matti Lassas, Kati Niinimäki, and Samuli Siltanen, *Sparse tomography*, Preprint.

[HKL+10] Nuutti Hyvönen, Martti Kalke, Matti Lassas, Henri Setälä, and Samuli Siltanen, *Three-dimensional dental X-ray imaging by combination of panoramic and projection data*, Inverse Problems and Imaging **4** (2010), no. 2, 257–271.

[Hör03] Lars Hörmander, *The analysis of linear partial differential operators. I*, Classics in Mathematics, Springer-Verlag, Berlin, 2003, Distribution theory and Fourier analysis, Reprint of the second (1990) edition [Springer, Berlin].

[Hou73] Godfrey N. Hounsfield, *Computerized transverse axial scanning (tomography): Part 1. Description of system*, British Journal of Radiology **46** (1973), no. 552, 1016–1022.

[HSP11] Per Christian Hansen, Emil Y. Sidky, and Xiaochuan Pan, *Accelerated gradient methods for total-variation-based CT image reconstruction*, arXiv.org **math.NA** (2011).

[IG03] James T. Dobbins III and Devon J. Godfrey, *Digital x-ray tomosynthesis: current state of the art and clinical potential*, Physics in Medicine and Biology **48** (2003), no. 19, R65 – R106.

[III09] James T. Dobbins III, *Tomosynthesis imaging: At a translational crossroads*, Medical Physics **36** (2009), no. 6, 1956–1967.

[Ino79] Tamon Inouye, *Image Reconstruction with Limited Angle Projection Data*, Proceedings of IEEE Transactions on Nuclear Science **26** (1979), no. 2, 2665–2669.

[Kei89] Fritz Keinert, *Inversion of k-plane transforms and applications in computer tomography*, SIAM Review **31** (1989), no. 2, 273–298.

[Kir96] Andreas Kirsch, *An introduction to the mathematical theory of inverse problems*, Applied Mathematical Sciences, vol. 120, Springer-Verlag, New York, 1996.

[KL07] Gitta Kutyniok and Demetrio Labate, *Construction of Regular and Irregular Shearlet Frames*, Journal of Wavelet Theory and Applications **1** (2007), no. 1, 1–12.

[Kla11] Esther Klann, *A Mumford–Shah-Like Method for Limited Data Tomography with an Application to Electron Tomography*, SIAM Journal on Mathematical Analysis **4** (2011), no. 4, 1029–1048.

[KLQ12] Venkateswaran P. Krishnan, Howard Levinson, and Eric Todd Quinto, *Microlocal Analysis of Elliptical Radon Transforms with Foci on a Line*, The Mathematical Legacy of Leon Ehrenpreis, Springer Milan, 2012, pp. 163–182.

[KRR11] Esther Klann, Ronny Ramlau, and Wolfgang Ring, *A Mumford-Shah level-set approach for the inversion and segmentation of SPECT/CT data*, Inverse Problems and Imaging **5** (2011), no. 1, 137–166.

[KS88] Avinash C. Kak and Malcom Slaney, *Principle of Computerized Tomographic Imaging*, IEEE Press, 1988.

[KS05] Jari Kaipo and Erkki Somersalo, *Statistical and Computational Inverse Problems*, Applied Mathematical Sciences, vol. 160, Springer-Verlag, New York, 2005.

[KSJ+03] Ville Kolehmainen, Samuli Siltanen, Seppo Järvenpää, et al., *Statistical inversion for medical x-ray tomography with view radiographs: II. Application to dental radiology*, Physics in Medicine and Biology **48** (2003), 1465ñ–1490.

[LLKW05] Demetrio Labate, Wang-Q Lim, Gitta Kutyniok, and Guido Weiss, *Sparse multidimensional representation using shearlets*, Proceedings of SPIE, Wavelets XI, vol. 5914, 2005, pp. 254–262.

[LM90] Alfred K. Louis and Peter Maass, *A mollifier method for linear operator equations of the first kind*, Inverse Problems **6** (1990), no. 3, 427.

[LMKH08] Jasmina Ludwig, Thomas Mertelmeier, Holger Kunze, and Wolfgang Härer, *A novel approach for filtered backprojection in tomosynthesis based on filter kernels determined by iterative reconstruction techniques*, Digital Mammography / IWDM, Lecture Notes in Computer Science, vol. 5116, Springer, 2008, pp. 612–620.

[Lor04] Dirk Lorenz, *Variational Denoising in Besov Spaces and Interpolation of Hard and Soft Wavelet Shrinkage*, Tech. report, Preprint series of the DFG priority program 1114 "Mathematical methods for time series analysis and digital image processing", March 2004.

[Lor09a] Dirk Lorenz, *On the role of sparsity in inverse problems*, Journal of Inverse and Ill-Posed Problems **17** (2009), no. 1, 61–68.

[Lor09b] Ignace Loris, *On the performance of algorithms for the minimization of l_1-penalized functionals*, Inverse Problems **25** (2009), no. 3, 035008 (16pp).

[Lou79] Alfred K. Louis, *Picture Reconstruction from Projections in Restricted Range*, Tech. report, 1979.

[Lou84] ———, *Orthogonal function series expansions and the null space of the Radon transform*, SIAM Journal on Mathematical Analysis **15** (1984), no. 3, 621–633.

[Lou86] ———, *Incomplete data problems in x-ray computerized tomography. I. Singular value decomposition of the limited angle transform*, Numerische Mathematik **48** (1986), no. 3, 251–262.

[Lou89] ———, *Inverse und schlecht gestellte Probleme*, Teubner Studienbücher Mathematik. [Teubner Mathematical Textbooks], B. G. Teubner, Stuttgart, 1989.

[LT08] Dirk Lorenz and Dennis Trede, *Optimal convergence rates for tikhonov regularization in besov scales*, Inverse Problems **24** (2008), no. 5, 055010.

[Mad90] W. R. Madych, *Summability and Approximate Reconstruction from Radon Transform Data*, Contemporary Mathematics **113** (1990), 189–219.

[Mad04] ———, *Radon's Inversion Formulas*, Transactions of the American Mathematical Society **356** (2004), no. 11, 4475–4491.

[Mal09] Stéphane Mallat, *A wavelet tour of signal processing*, third ed., Elsevier/Academic Press, Amsterdam, 2009, The sparse way, With contributions from Gabriel Peyré.

[MP07] Stéphane Mallat and Gabriel Peyre, *A review of Bandlet methods for geometrical image representation*, Numerical Algorithms **44** (2007), no. 3, 205–234.

[MP10] Jianwei Ma and Gerlind Plonka, *The Curvelet Transform*, Signal Processing Magazine, IEEE **27** (2010), no. 2, 118 –133.

[MS12] Jennifer L. Mueller and Samuli Siltanen, *Linear and Nonlinear Inverse Problems with Practical Applications*, SIAM, October 2012.

[N+97] L. T. Niklason et al., *Digital tomosynthesis in breast imaging.*, Radiology **205** (1997), no. 2, 399–406.

[Nat86] Frank Natterer, *The mathematics of computerized tomography*, B. G. Teubner, Stuttgart, 1986.

[NW01] Frank Natterer and Frank Wübbeling, *Mathematical methods in image reconstruction*, SIAM Monographs on Mathematical Modeling and Computation, Society for Industrial and Applied Mathematics (SIAM), Philadelphia, PA, 2001.

[Per79] Asher Peres, *Tomographic Reconstruction from Limited Angular Data*, Journal of Computer Assisted Tomography **3** (1979), no. 6, 800–808003.

[PSV09] Xiaochuan Pan, Emil Y. Sidky, and Michael Vannier, *Why do commercial CT scanners still employ traditional, filtered back-projection for image reconstruction?*, Inverse Problems **25** (2009), no. 12, 123009.

[Qui93] Eric Todd Quinto, *Singularities of the X-ray transform and limited data tomography in* $\mathbb{R}^2$ *and* $\mathbb{R}^3$, SIAM Journal on Mathematical Analysis **24** (1993), no. 5, 1215–1225.

[Qui06] ———, *An introduction to X-ray tomography and Radon transforms*, The Radon transform, inverse problems, and tomography, Proc. Sympos. Appl. Math., vol. 63, American Mathematical Society, Providence, RI, 2006, pp. 1–23.

[Rad17] Johann Radon, *Über die Bestimmung von Funktionen durch ihre Integralwerte längs gewisser Mannigfaltigkeiten*, Berichte über die Verhandlungen der Sächsische Akademie der Wissenschaften **69** (1917), 262–277.

[Rad86] ———, *On the determination of functions from their integral values along certain manifolds*, IEEE Transactions on medical imaging **5** (1986), no. 4, 170–176, Translated by P. C. Parks from the original German text.

[Ram91] Alexander G. Ramm, *Inversion of Limited Angle Tomographic data*, Computers Math. Applic. **22** (1991), no. 4/5, 101–111.

[Ram92] ———, *Inversion of limited angle tomographic data II*, Applied Mathematics Letters **5** (1992), no. 2, 47–49.

[Rin00] Wolfgang Ring, *Structural properties of solutions to total variation regularization problems*, Mathematical modelling and numerical analysis **34** (2000), no. 4, 799–810.

[RK96] Alexander G. Ramm and Alexander I. Katsevich, *The Radon transform and local tomography*, CRC Press, Boca Raton, FL, 1996.

[Roc70] R. Tyrrell Rockafellar, *Convex analysis*, Princeton Mathematical Series, No. 28, Princeton University Press, Princeton, N.J., 1970.

[RS72] Michael Reed and Barry Simon, *Methods of modern mathematical physics. I. Functional analysis*, Academic Press, New York, 1972.

[Rud91] Walter Rudin, *Functional analysis*, second ed., International Series in Pure and Applied Mathematics, McGraw-Hill Inc., New York, 1991.

[RVJ+06] Maaria Rantala, Simopekka Vänskä, Seppo Järvenpää, et al., *Wavelet-based reconstruction for limited angle x-ray tomography*, IEEE Transactions on Medical Imaging **25** (2006), no. 2, 210–217.

[RY08] Bryan P. Rynne and Martin A. Youngson, *Linear functional analysis*, second ed., Springer Undergraduate Mathematics Series, Springer-Verlag London Ltd., London, 2008.

[Sch07] Thomas Schuster, *The Method of Approximate Inverse: Theory and Applications*, Lecture Notes in Mathematics, vol. 1906, Springer, Berlin Heidelberg, 2007.

[SFS06] William C Scarfe, Allan G Farman, and Predag Sukovic, *Clinical Applications of Cone-Beam Computed Tomography in Dental Practice*, February 2006.

[SGG+09] Otmar Scherzer, Markus Grasmair, Harald Grossauer, Markus Haltmeier, and Frank Lenzen, *Variational methods in imaging*, Applied Mathematical Sciences, vol. 167, Springer, New York, 2009. MR 2455620 (2009j:49001)

[SKJ+03] Samuli Siltanen, Ville Kolehmainen, Seppo Järvenpää, et al., *Statistical inversion for medical x-ray tomography with view radiographs: I. General theory*, Physics in Medicine and Biology **48** (2003), 1437–1463.

[SMB03] Kristian Sandberg, David N. Mastronarde, and Gregory Beylkin, *A fast reconstruction algorithm for electron microscope tomography*, Journal of Computational and Applied Mathematics **144** (2003), no. 1-2, 61–72.

[Ste70] Elias M. Stein, *Singular integrals and differentiability properties of functions*, Princeton Mathematical Series, No. 30, Princeton University Press, Princeton, N.J., 1970.

[SW71] Elias M. Stein and Guido Weiss, *Introduction to Fourier analysis on Euclidean spaces*, Princeton University Press, Princeton, N.J., 1971, Princeton Mathematical Series, No. 32.

[Tuy81] Heang Tuy, *Reconstruction of a three-dimensional object from a limited range of views*, Journal of mathematical analysis and applications **80** (1981), no. 2, 598–616.

[YDC05] Lexing Ying, Laurent Demanet, and Emmanuel J. Candès, *3D discrete curvelet transform*, Proceedings of SPIE, Wavelets XI, vol. 5914, September 2005, pp. 351–361.

[YF02] Daniel F. Yu and Jeffrey A. Fessler, *Edge-preserving tomographic reconstruction with nonlocal regularization*, IEEE Transactions on medical imaging **21** (2002), no. 2, 159–173.

[ZCS+06] Yiheng Zhang, Heang-Ping Chan, Berkman Sahiner, Jun Wei, Mitchell M. Goodsitt, Lubomir M. Hadjiiski, Jun Ge, and Chuan Zhou, *A comparative study of limited-angle cone-beam reconstruction methods for breast tomosynthesis*, Medical Physics **33** (2006), no. 10, 3781–3795.